Molecular design for moving from fluorescent to TADF emitters toward high-performance OLEDs and organic lasers

湯, 洵

2022

Doctoral thesis

高性能 OLED 及び有機レーザーを目指した蛍光から TADF までの分子設計

Molecular design for moving from fluorescent to TADF emitters toward high-performance OLEDs and organic lasers

Xun Tang

Department of Chemistry and Biochemistry

Graduate School of Engineering

Kyushu University

Table of contents

Chapter 1. General introduction

1.1 The nature of light

Light, which is known as a kind of electromagnetic radiation, brightens our darkness and plays a vital role in our daily life.[1] At the most fundamental level, light exhibits two extremely significant features: (i) light is energy in motion, and it moves with an extremely fast speed (c=2.99×10^8 m s^{-1} in a vacuum);[2, 3] (ii) light can convey information. Scientists discovered later that light is intrinsically a very complicated phenomenon. A Dutch physicist and mathematician Christiaan Huygens asserted that light is composed of *waves*.[4] Followed by Isaac Newton, who is an English physicist and mathematician, noticed that light is composed of *particles*. It was not until the 20th century that modern scientists perceived light as a *dual*-nature; that is, light behaves as a wave in some circumstances, while there are other circumstances in which it exhibits a particle. This dual wave-like and particle-like nature of light is known as the wave-particle duality.[4, 5]

1.2 Radiation mechanism and process

1.2.1 Spontaneous and stimulated emission

Absorption, spontaneous emission, and stimulated emission are three relevant processes to generate photons with different types of light.[6, 7] As shown in **Figure 1-1 (a)**, absorption is a process in which the energy of an incident photon is converted to the internal energy of electrons from the ground state (E_1) to the excited state (E_2). The light-emitting process will take place after the absorption. Spontaneous emission is a radiative energy conversion process, where an excited electron at E_2 decays to E_1 to generate a photon. Spontaneous emission depends on the electrons at E_2; the rate of spontaneous emission can be modeled as the equation 1.1:

$$\left(\frac{dN_2}{dt}\right)_{sp} = -A_{21}N_2, \text{ (Eq. 1.1)}$$

where N_2 is the number of atoms per unit volume at E_2, and the constant of proportionality A_{21} is called Einstein A coefficient.[8] Meanwhile it ought to be noted

that the radiative emission is just one of the two possible ways within this decay process, the energy might go through the nonradiative decay by converting to heat (mechanical vibrations). Also, another feature of the photons from the spontaneous emission is random direction, phase, and electromagnetic polarization.

Stimulated emission is a process, where an incident photon with equal energy to (E_2−E_1) can interact with an excited electron, thereby inducing the light amplification. As equation 1.2 shows:

$$\left(\frac{dN_2}{dt}\right)_{st} = -B_{21}\mu N_2, \text{ (Eq. 1.2)}$$

where the constant of proportionality B_{21} is known as another Einstein B coefficient[9] and μ is the spectral energy density per unit bandwidth. It is worth noting that the stimulated photons will have the same frequency, direction, phase, and electromagnetic polarization as the incident one.

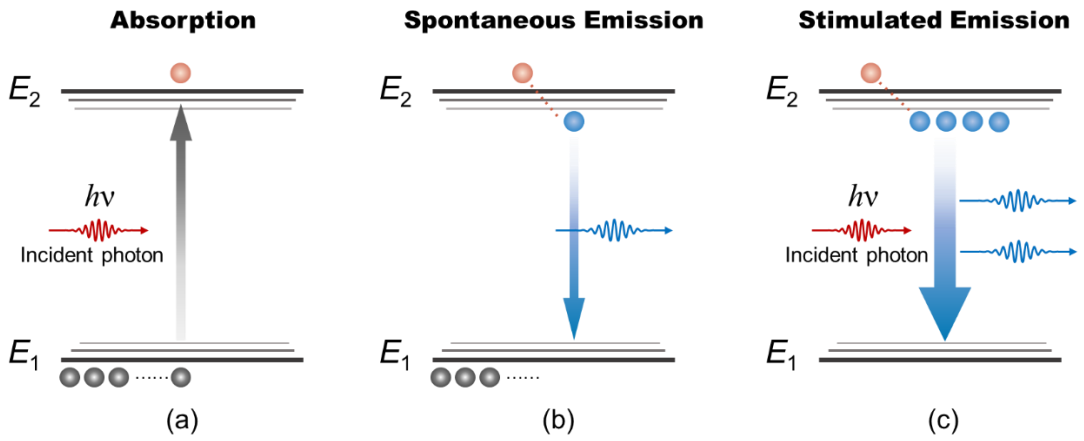

Figure 1-1. Schematic illustration of the three processes: (a) absorption; (b) spontaneous emission, and (c) stimulated emission.

1.2.2 Fluorescence, phosphorescence, and delayed fluorescence

As shown in the Jablonski diagram of **Figure 1-2**, the radiative transition (emission of photons) from the singlet excited state (S_1) to the ground state (S_0) is known as fluorescence, as a consequence of the photon absorption, rapid vibrational relaxation, as well as possible internal conversion (IC). Fluorescence usually takes place between

the two electronic states of the same spin multiplicity.[10] In common, the radiative rate of a fluorescence emitter is as fast as 10^7–10^{10} s^{-1}, which makes it a very promising candidate for organic light-emitting devices (OLEDs) and lasers.[11, 12] In contrast, phosphorescence is a radiative transition from the triplet excited state (T_1) to S_0, which contains two electronic states of the different spin multiplicity.[13] Similar to the intersystem crossing (ISC) process, phosphorescence is in principle a forbidden transition owing to the different spin multiplicity. However, this transition is able to be weakly allowed through the spin-orbit coupling (SOC) effect.[14] Because of the involvement of the spin-flip process, the phosphorescence transition lifetime is very large (timescale ranges from 10^{-6} to 10 s), which is not suitable for laser dyes; however, afterglow usually takes place owing to the "long-lived" triplet excitons.[15] The third type of radiative transition is known as the delayed fluorescence (DF), including the P-type of triplet-triplet annihilation (TTA) and E-type of thermally activated delayed fluorescence (TADF).[16, 17] Both of these two delayed fluorescence mechanisms come from the reverse intersystem crossing (RISC) from T_1 to S_1. Because the spin-flip process is also required for this forbidden transition between S_1 and T_1, the prompt and delayed emission components have the same spectral shapes but the latter has a longer radiative lifetime.

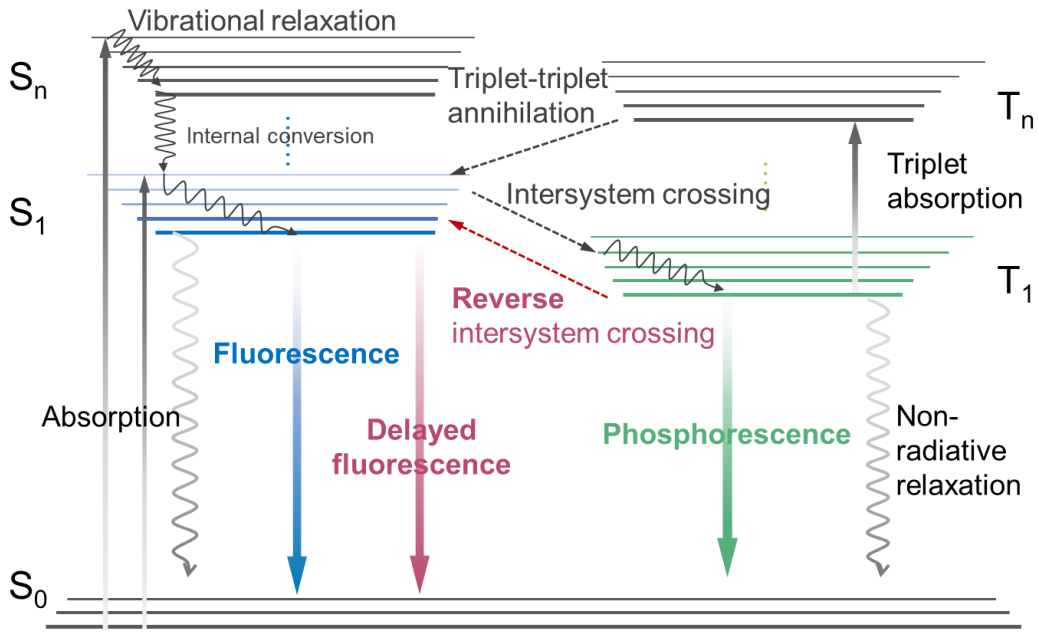

Figure 1-2. Perrin-Jablonski diagram showing the possible radiative and nonradiative transitions. S_0, S_1, and S_n represent the ground state, the 1st singlet excited state, and the higher-lying (n≥2) singlet excited state, respectively. T_1 and T_n denote the 1st triplet excited state and the higher-lying (n≥2) triplet excited state, respectively.

1.3 Exciton utilization in OLEDs

1.3.1 Design and principle of OLEDs

Since the first report on electroluminescence (EL) from an anthracene crystal by Pope et al., with an extremely high driving voltage exceeding 400 V, the development of OLEDs is exactly the improvement of exciton utilization efficiency by engineering materials and devices.[18] As illustrated in **Figure 1-3**, a conventional OLED structure has several functional organic layers sandwiched between the anode and cathode electrodes. The organic region is composed of a hole-injection layer (HIL), a hole-transporting layer (HTL), an electron-blocking layer (EBL), an emissive layer (EML), a hole-blocking layer (HBL), an electron-transporting layer (ETL), and an electron-injection layer (EIL), respectively.

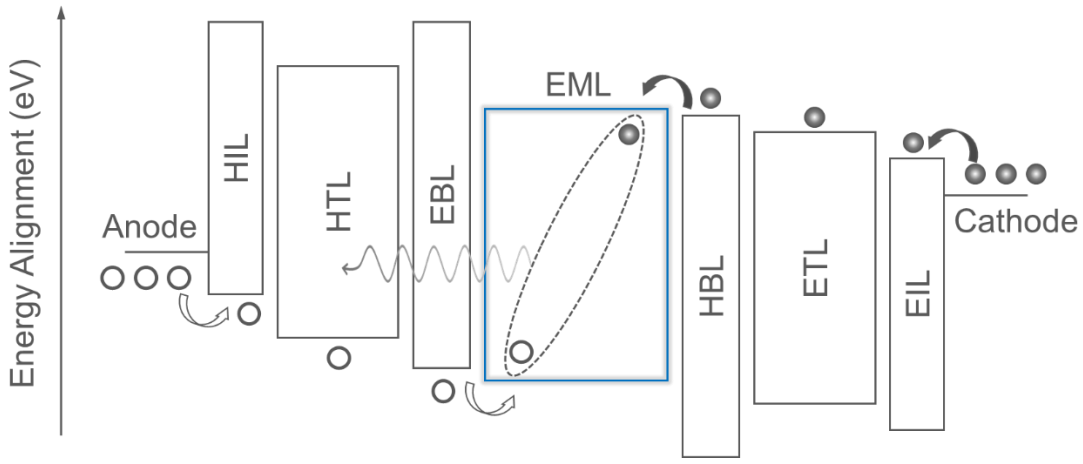

Figure 1-3. Conventional OLED structure includes functional multilayers of the anode, HIL, HTL, EBL, EML, HBL, ETL, EIL, and cathode.

Herein as shown in **Figure 1-4**, the injected holes and electrons are transported through the highest occupied molecular orbital (HOMO) and lowest unoccupied molecular orbital (LUMO) level of the injection and transporting layers, and followed by the recombination in the EML. The formed high-energy hole-electron pair is called "exciton". According to the spin-statistic rule, the singlet and triplet excitons are generated at a ratio of 1:3 under the electrical excitation. External quantum efficiency (EQE) of OLEDs is given by the following equation:

$$\eta_{ext} = \eta_r \cdot \chi \cdot \phi_{PL} \cdot \eta_{out}, \text{ (Eq. 1.3)}$$

where η_{ext} is the EQE, η_r is the charge-carrier (hole/electron) balance factor, χ is the spin statistic factor, ϕ_{PL} is the photoluminescence quantum yield (PLQY), and η_{out} is the light outcoupling efficiency of devices. Ideally, η_r and ϕ_{PL} are unity if the excellent charge balance and efficient radiative transition are obtained. η_{out} is commonly considered as 20%, because of the photon loss from waveguide mode, surface plasma polariton (SPP), and so on, Therefore, maximizing the χ value, in other words, fully harvesting singlet and triplet excitons for radiation process is the intrinsic target to improve the EQE.

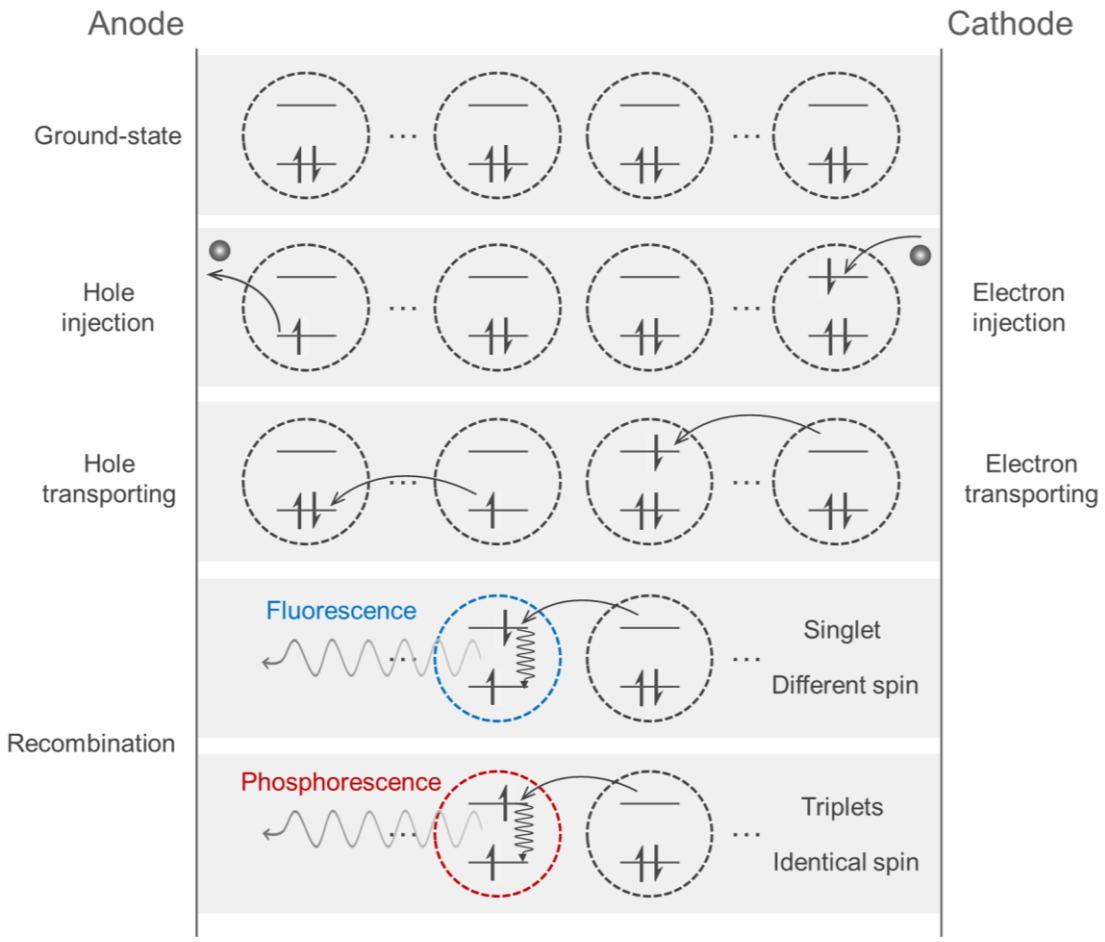

Figure 1-4. Carrier injection, transporting, recombination, and formation of fluorescence/phosphorescence processes in OLEDs.[19]

1.3.2 Exciton utilization in fluorescence OLEDs

The 1st generation OLED technology, in which a fluorescence emitter tris(8-hydroxyquinoline) aluminum (Alq_3) was used for light-emitting, was proposed by Tang and VanSlyke in 1987.[11] In the fluorescence OLEDs, only 25% singlets generated under the electrical excitation could be employed for radiative emission, because of the very weak SOC effects in organic molecules like Alq_3. Thus, the maximum χ value or internal quantum efficiency (IQE) is limited at 25%, indicating the theoretically maximum EQE is calculated to be 5% in such fluorescence OLEDs. Therefore, full utilization of singlets and triplets toward 100% IQE is anticipated if the strong SOC effect can provide the probability of spin multiplets mixing.

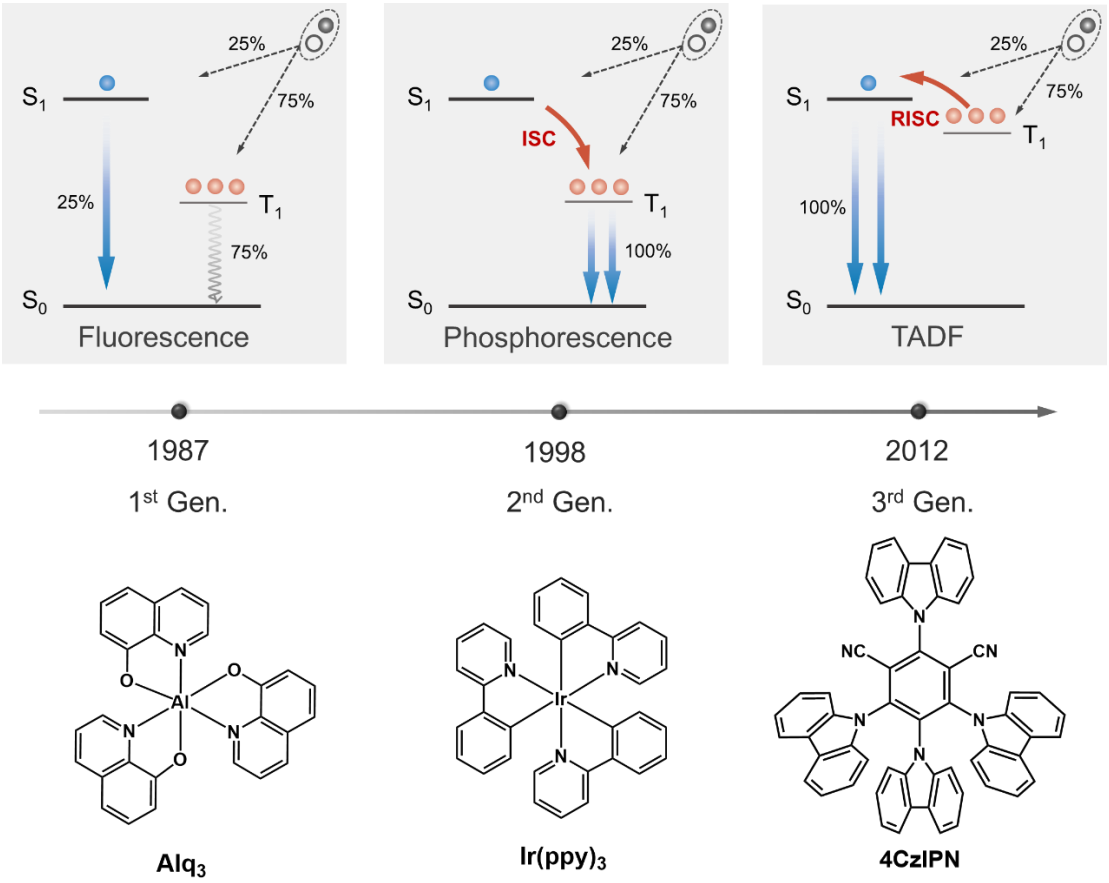

Figure 1-5. Exciton utilization efficiency progress of OLEDs from the 1st generation fluorescence-based OLEDs (1987) to the 2nd generation phosphorescence-based OLEDs (1998), and the 3rd generation TADF-based OLEDs (2012). The chemical structures of the representative light-emitting molecules Alq_3 (fluorescence), tris(2-phenylpyridine)iridium(III) [$Ir(ppy)_3$, phosphorescence], and 1,2,3,5-tetrakis(carbazol-9-yl)-4,6-dicyanobenzene (4CzIPN, TADF) as shown.

1.3.3 Exciton utilization in phosphorescence OLEDs

To harvest the spin-forbidden triplets, a strong SOC from the heavy-atom effect was utilized by Forrest et al. for the fabrication of the 2nd generation phosphorescence OLEDs in 1998.[14] According to the spin-orbit perturbation (SOP) theory, it is evident that the triplet wavefunctions are usually not pure zero-order, but a mixture of singlet nature functionalized by perturbation (such as SOC) to some degree at the excited state. In this case, a simple generalization of the SOC operator to determine the molecules can be presented as:

$$H_{SO} = \frac{e^2\hbar^2}{2m^2c^2}\frac{Z}{r^3}\vec{l}_i\vec{s}_i = \lambda\,\vec{L}\vec{S}, \text{(Eq. 1.4)}$$

where $\lambda = \pm\frac{\xi}{2S}$ is the SOC constant, $\vec{L}$ is the angular momentum of an electron, $\vec{S}$ is the spin of an electron, Z is the nuclear charge, $\hbar$ is the Planck's constant, e is the elementary charge, c is the velocity of light, m is the mass of an electron, r is the radius of the atom. To promote the singlet-triplet spin mixture, using the heavy-metal atom would be an efficient way to enlarge the SOC value, due to their very large Z values. Benefitting from this theory, the singlets could transfer to the triplet state by a fast ISC process, followed by the decay to the ground state as phosphorescence even at room temperature. Therefore, nearly 100% of IQE can be achieved, indicating that the maximum EQE is boosted to ~20%, which is about four times the EQE (~5%) of fluorescent OLEDs. However, the radiative transition of triplet excitons from T_1 excited state to S_0 will exhibit a much longer lifetime from microseconds to a few seconds, which definitely limits its applications for ASE or lasing.

1.3.4 Exciton utilization in TADF OLEDs

Although the emitters based on phosphorescent heavy-atom complexes have achieved almost unity IQEs, the use of rare and expensive heavy metals limits their further applications. To relieve the cost and environmental issues of expensive rare metals used in phosphors, a cutting-edge strategy named TADF was put forward by Adachi et al. in 2012, in which triplets could be up-converted to the S_1, through which the delayed fluorescence emission takes place.[20] This up-conversion process is called RISC. Herein, in the pure organic compounds, the conversion between the singlet and triplet manifolds mainly depends on two parameters, besides the SOC strength (H_{SO}), singlet-triplet splitting (ΔE_{ST}) plays a crucial role in the probability of the RISC process. In the framework of the perturbation theory, the singlet/triplet mixing coefficient $c_{S_1T_1}$ can be presented as:

$$c_{S_1T_1} \propto \frac{H_{SO}}{\Delta E_{ST}}, \text{(Eq. 1.5)}$$

From the aforementioned relationship, decreasing the ΔE_{ST} with increasing the H_{SO} is required to increase the probability of the ISC and RISC processes. In a simple two-electron two-state model, the energy of S_1 (E_{S1}), T_1 (E_{T1}), and ΔE_{ST} can be expressed as follows:

$$E_{S1} = h_H + h_L + J_{HL} + K_{HL}, \text{(Eq. 1.6)}$$

$$E_{T1} = h_H + h_L + J_{HL} - K_{HL}, \text{(Eq. 1.7)}$$

$$\Delta E_{S1T1} = 2K_{HL}, \text{(Eq. 1.8)}$$

where h_H and h_L represent the HOMO and LUMO wavefunction orbits, respectively, J_{HL} denotes the Coulomb repulsion energy between two electrons, and K_{HL} is the electron exchange energy. Furthermore, K_{HL} and ΔE_{S1T1} can be expanded as:

$$K_{HL} = \frac{e^2}{4\pi\varepsilon_0} \iint \varphi_H(\overrightarrow{r_1})\varphi_L(\overrightarrow{r_2}) \frac{1}{|\overrightarrow{r_1}-\overrightarrow{r_2}|} \varphi_H(\overrightarrow{r_2})\, \varphi_H(\overrightarrow{r_1}) d^3\overrightarrow{r_1} d^3\overrightarrow{r_2}, \text{(Eq. 1.9)}$$

$$\Delta E_{S1T1} = \frac{e^2}{2\pi\varepsilon_0} \iint \varphi_H(\overrightarrow{r_1})\varphi_L(\overrightarrow{r_2}) \frac{1}{|\overrightarrow{r_1}-\overrightarrow{r_2}|} \varphi_H(\overrightarrow{r_2})\, \varphi_L(\overrightarrow{r_1}) d^3\overrightarrow{r_1} d^3\overrightarrow{r_2}, \text{(Eq. 1.10)}$$

where φ_H and φ_L are the HOMO and LUMO wavefunctions, respectively. From equations 1.9 and 1.10, it can be concluded that ΔE_{ST} mainly depends on the spatial overlap between φ_H and φ_L. To obtain a small ΔE_{ST} and thereby accomplish triplet up-conversion at room temperature, the overlap between φ_H and φ_L ought to be largely eliminated. In that case, as shown in **Figure 1-6**, the conventional TADF molecules are commonly composed of distinct electron-donating (donor) and electron-accepting (acceptor) fragments, which are linked with a large dihedral angle or spatial arrangement for a sufficient wavefunction separation. In such D-A type designs, the wavefunctions of HOMO essentially localize at a donor fragment, while the ones of LUMO concentrate on an acceptor moiety. Benefitting from this cutting-edge strategy, 100% IQE can also be realized by the prompt and delayed radiative transition from pure organic compounds, which thereby results in EQEs exceeding 20% for TADF OLEDs as well. As another alternative strategy that can harvest triplets and singlets for radiation,

many efforts have been devoted to TADF molecules toward laser activities. However, it is evident that a small ΔE_{ST} alone is not sufficient for enabling an efficient TADF radiation process or a fast radiative transition rate, other than the laser actions. Actually, TADF molecules commonly possess a retarded radiative transition rate of k_r~10^6 to 10^8 s^{-1}. Thus, very rare TADF molecules exhibit ASE performance up to now, which will be further discussed in section 1.4.

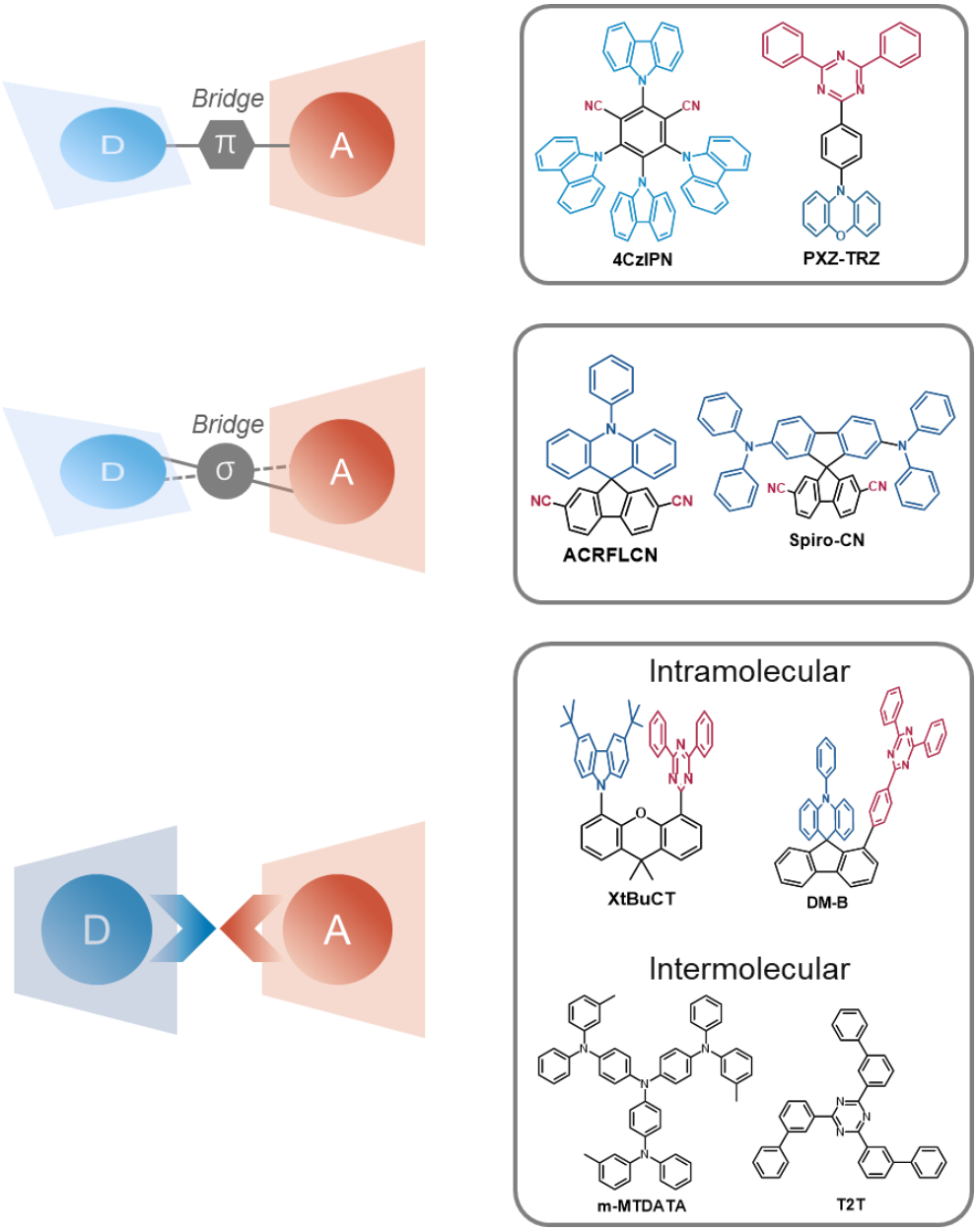

Figure 1-6. Fundamental D/A type molecular designs with different interplays (conjugated link, unconjugated link, and through-space arrangement or exciplex) toward TADF emission.

1.4 Exciton utilization in organic lasers

As another type of radiative transition process (stimulated emission), lasers from organic dyes ought to have a similar developing track to the OLEDs that utilize spontaneous emission. There are commonly three fundamental elements illustrated in **Figure 1-7** to realize organic lasers: (i) an ideal amplifying gain medium, in which an incident photon will be amplified after passing through this gain bulk; (ii) an optical resonator, which is usually incorporated to enhance the amplification capability and manipulate the output spectra or geometry of laser beams; (iii) a pumping source, which denotes an external system to excite the gain medium for light amplification by supplying the required energy. Usually, the pumping source can be classified as optical- or electrical-pumping.

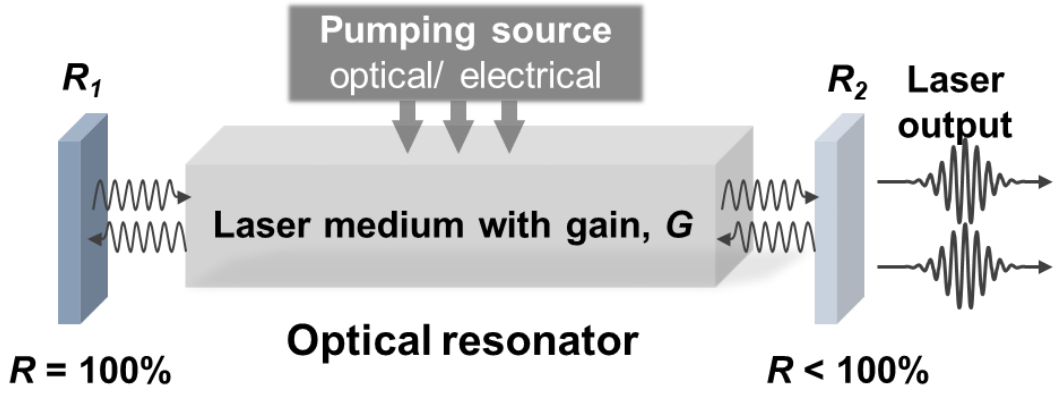

Figure 1-7. Architecture to realize organic lasers, including the organic gain medium, optical resonator, and pumping source.

1.4.1 Progress of organic lasers

As shown in **Figure 1-8**, the indication of the first laser from organic dye solution was announced by F. P. Schafer et al. in 1966, which was regarded as the milestone in the research field of organic lasers.[12, 21, 22] Then, a continuous-wave (CW) organic laser was latterly achieved by using a solution of Rhodamine 6G in water.[23] To "escape" from the solution, the first laser from an organic solid-state film was reported by F. Hide et al. in 1996,[24-26] which was followed by a number of molecular designs for the

extremely low thresholds,[27-33] such as the renowned 4,4'-bis[(*N*-carbazole)styryl]biphenyl (BSBCz).[34-36] Later, the quasi-CW solid-state lasers operating from 5 MHz to 80 MHz were subsequently demonstrated by reducing the exciton quenching and annihilation channels.[37-39] Then, incorporating with the OLED engineering that could tolerate the extremely high current density injection over 100 A cm^{-2} with the suppressed efficiency rolloff,[40-42] electrical-pumping laser diodes have been encouragingly indicated in 2019.[43] It ought to be noticed that most of the organic laser works and milestones are on the basis of fluorescence dyes, indicating that only singlets were utilized for radiative transition. Therefore, the progress of exciton utilization efficiency in organic lasers lags far behind the phosphorescence and TADF OLEDs.

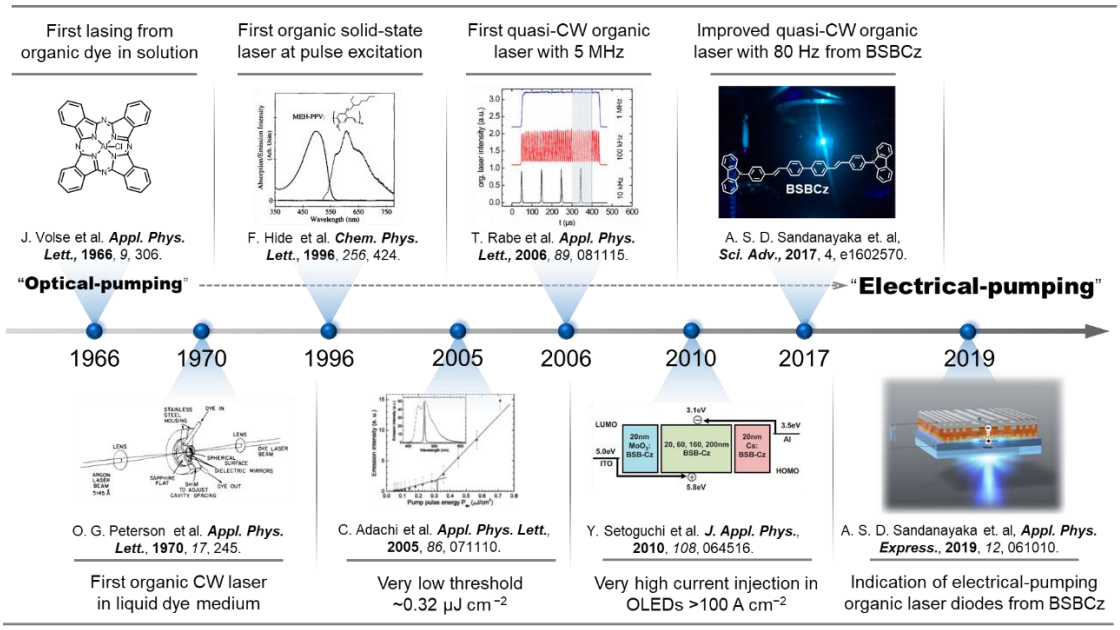

Figure 1-8. Progress of organic lasers from a liquid dye to the indication of solid-state electrical-pumping OSLDs based on fluorescence dyes.

1.4.2 Organic lasers from fluorescence dyes

As discussed above, the history of organic lasers started from the dye molecules dissolved in liquid solvents. Then, a number of organic gain dyes were designed toward the solid-state semiconductor lasers, where the incorporation of dyes into the solid films

arises much interest as its facile processability, wide-range color tunability, and feasible compatibility with the optical resonator structures. As an excellent laser dye, there are several requirements to meet: (i) the stimulated emission cross-section (σ_{em}) should be high; (ii) the PLQY is high, implying the weak quenching, internal conversion (IC), and ISC process must be suppressed; (iii) optical losses, including the ground-state absorption, scattering losses, ISC rate, singlet-singlet annihilation (SSA), triplet absorption (TA), and singlet-triplet annihilation (STA) at the laser wavelength ought to be minimized; (iv) the Stokes shift should be rationally controlled to prevent too large shift for reducing the nonradiative transition such as Joule heat, or too small shift for reducing the reabsorption; (v) the dyes should have good photostability against the intense excitation power, oxygen, and moisture from the environment.

Figure 1-9 lists the representative cores building up the laser molecules, and their derivatives can realize the wide-range color tuning of laser emission from ultraviolet (UV) to near infrared (NIR). For example, the coumarin-based family can cover the wavelength range from violet to green, while the poor photostability restricts its further application.[44] The Rhodamine family exhibits high photostability and efficiency in the region from green to red.[45] BODIPY-core based laser dyes, which own a rigid molecular skeleton, are composed of a pyrromethene unit linked to a borondifluoride group.[46-49] Laser dyes from the BODIPY-core usually have high PLQYs, moreover, benefiting from a variety of sites for functionalization, bathochromic (deep red to NIR) and hypsochromic (blue to green) shift can be realized by tuning diverse substituents at the skeleton.[50, 51] Phenylenevinylene-based small molecules are widely known organic laser catalogues with outstanding laser properties. Among them, a variety of derivatives with low laser thresholds can be obtained from the incorporation of *trans*-1,4-distyrylbenzene (DSB) and bis-styrylbenzene (BSB) fragments. In the case of a BSBCz derivative, which is end-capped with carbazole-groups, exhibits an extremely low ASE threshold of 0.32 μJ cm^{-2}.[34] Furthermore, owing to the negligible overlap with the excited state absorption, such as the TA and SSA, laser actions under the quasi-CW optical excitation and short-pulsed electrical pumping could be realized.[38, 43] Fluorene unit is also a crucial component in the laser molecular design, which can be

functionalized to increase the conjugation length and improve the solubility when substituted with alkyl chains at the 9,9'-position.[52-54] More complex fluorene-based structures such as the linear, star-shaped and dendritic oligomers or polymers have been widely investigated toward the extremely low ASE/laser thresholds.[29, 55] It is worth noting that their laser wavelengths are mostly localized in the blue region, because of no strong donor or acceptor units involved to shrink the wide energy gaps. Then, DCM, DPP, and BT units with a stronger electron-affinity capability were subsequently investigated toward the longer-wavelength emission.[56-61] Owing to the introduction of the strong donor and acceptor fragments, the intramolecular charge transfer (ICT) ought to be rationally manipulated to guarantee the laser actions. It is worth noting that the tuning of the CT states is crucial for realizing TADF lasers, which will be discussed in the following sections.

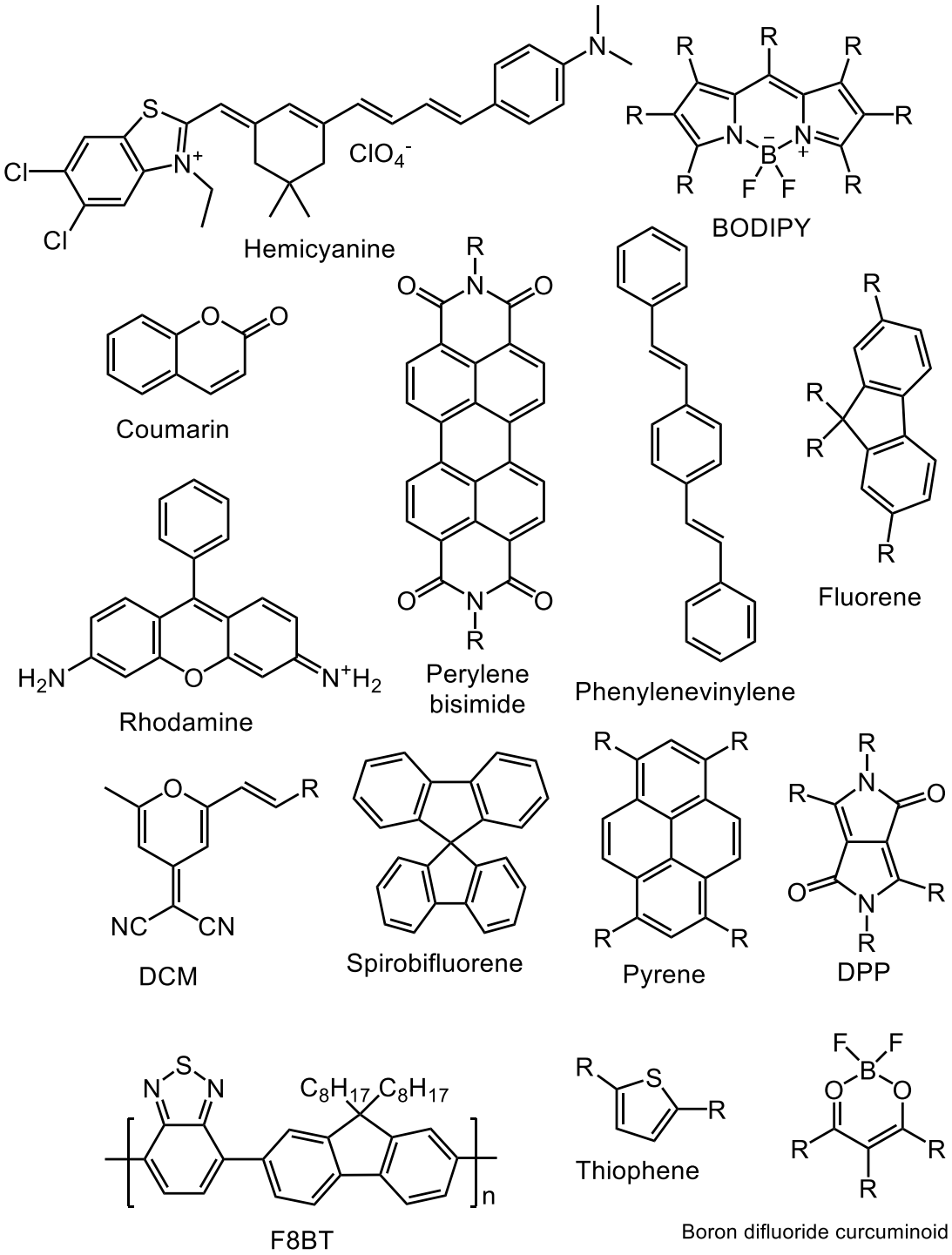

Figure 1-9. Representative laser cores for building up the fluorescent laser molecules.

1.4.3 Triplets behaviors in organic lasers

Similar to the limited exciton utilization in fluorescent OLEDs, in terms of the organic lasers based on fluorescence dyes, the detrimental effects from the accumulation of long-lived triplet excitons will be enlarged. As shown in **Figure 1-10**,

the dramatic triplet accumulation and singlet quenching take place at the same time after the external pumping turns on, because the lifetime of singlets is usually in the range of nanosecond, while triplet excitons exhibit a much longer lifetime (in a scale from microsecond to millisecond), which causes the triplet density to increase by several orders of magnitude in comparison with the singlet density.

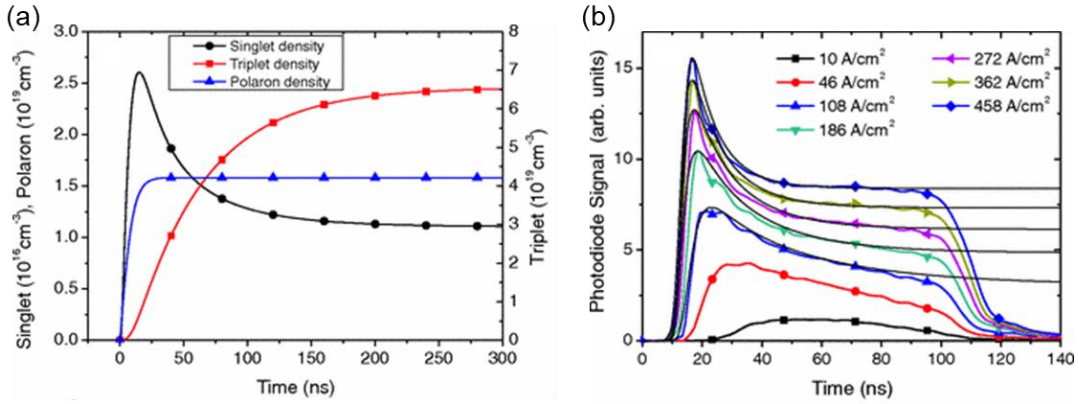

Figure 1-10. (a) Singlet and triplet population dynamics under the high current injection and (b) time-resolved EL signal under the different current injections.[62] The figures are reproduced from Ref. 62.

In that case, there are several interactions that triplets involved, including triplet nonradiative relaxation, TA, STA, and triplet-triplet annihilation (TTA), which are subsequently listed in **Figure 1-11**. As discussed above, triplets can be generated through the ISC process from singlets; thus, the corresponding process can be expressed by the rate coefficient k_{ISC}

$$S_1 \xrightarrow{k_{ISC}} T_1, \text{(Eq. 1.11)}$$

Commonly, the triplets will relax back to the ground state with a non-radiative transition. Nevertheless, under the high-power excitation or current density injection, the triplets would undergo an IC process to the high-lying triplet excited state (T_n, $n \geq 2$). This triplet behavior is called TA.

TTA and STA take place in the bimolecular interaction system. In the TTA process, the interaction between two triplets leads to a Dexter energy transfer (DET) from the first to the second molecule, which is thereby excited to the high-lying state that subsequently relaxes to the singlet energy level. In that case, TTA can some degree contribute to the radiation process in the particular condition. However, the high concentration inducing molecular collision is a prerequisite to satisfy the short-range Dexter exchange interaction. The corresponding TTA process can be expressed as

$$T_1 + T_1 \xrightarrow{k_{TT}} S_1 + S_0, \text{ (Eq. 1.12)}$$

where k_{TTA} is the TTA rate coefficient.

In terms of STA, implying the quenching of singlets by triplets is known as one of the main hindrances toward long-pulsed and terminal electrical-pumping lasers. Herein, when the singlet exciton energy in one molecule is approximately equal to the triplet internal conversion (T_1 to T_n, $n \geq 2$) of the second molecule, the long-distance Förster resonance energy transfer (FRET) can take place in the bimolecular system. Especially under electrical excitation, STA becomes severe because 75% of the generated excitons are triplets. The corresponding quenching process can be described as

$$S_1 + T_1 \xrightarrow{k_{STA}} T_1 + S_0, \text{ (Eq. 1.13)}$$

Where k_{STA} is the STA rate coefficient.

Therefore, under the condition of the optical excitation, the population of singlets can be described as the following equation 1.14:

$$\frac{dN_S}{dt} = p - k_r^s N_S - k_{SSA} N_S^2 - k_{STA} N_S N_T - k_{ISC} N_S + k_{TTA} N_T^2, \text{ (Eq. 1.14)}$$

where N_S and N_T denote singlet and triplet densities, respectively, p is the generation rate of singlet excitons, k_r^s is the rate constant of radiative decay from S_1 to S_0. Here, k_{SSA} implies the rate constant of singlet-singlet annihilation (SSA). It should be mentioned that the circumstance under electrical excitation will be much more complex,

due to the consideration of carrier injection, balance, singlet-polaron annihilation (SPA), and triplet-polaron annihilation (TPA).

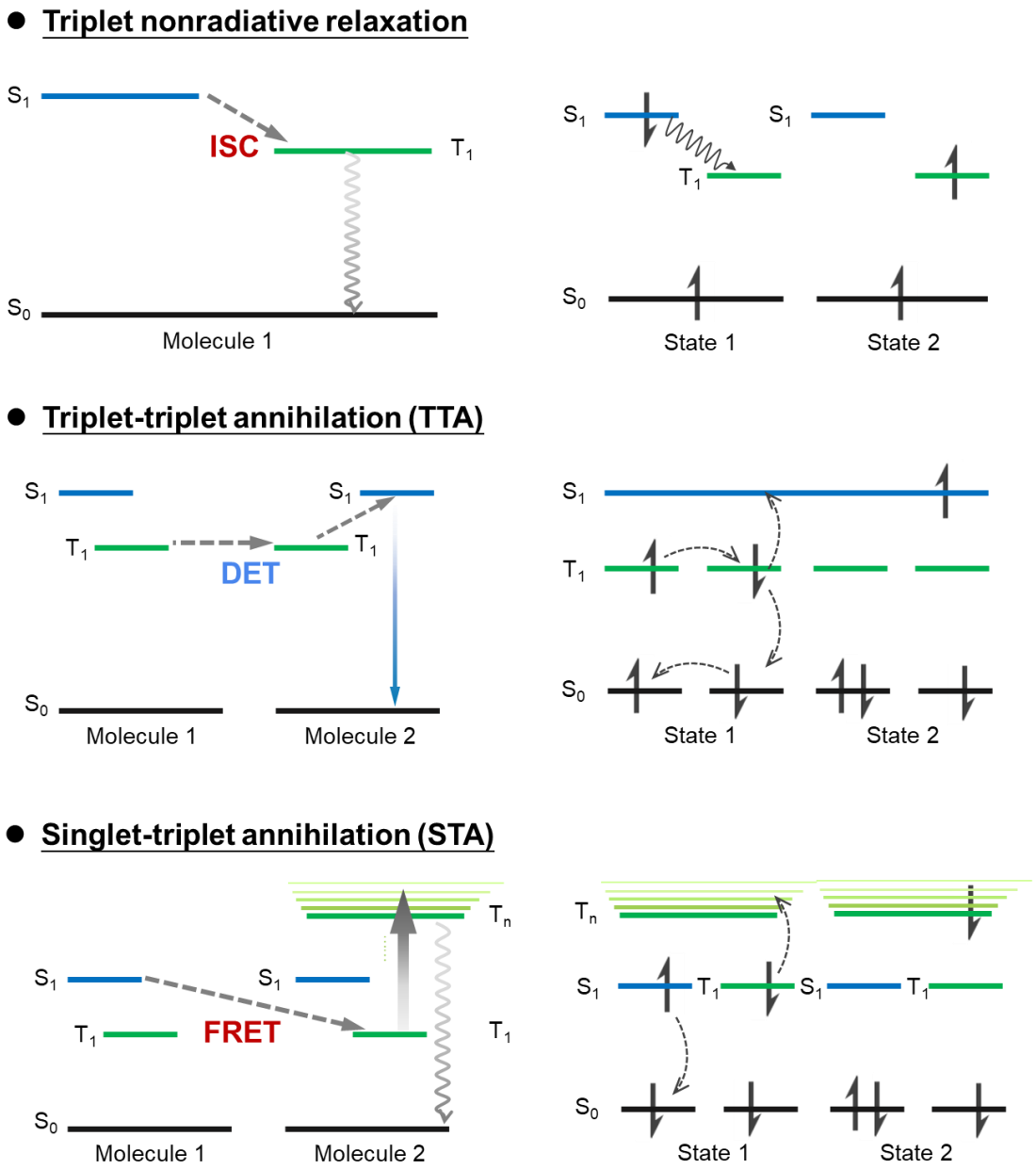

Figure 1-11. (a) Triplet nonradiative relaxation process in one molecule; (b) TTA process through DET in the bimolecular system; (c) STA process through a long-distance FRET.

Up to now, to suppress the aforementioned annihilation processes in the fluorescent laser system, the effective strategy is to remove or scavenge the triplets. As a consequence, several methods focusing on scavenging triplets are commonly adopted before unveiling the TADF concept, such as the employment of chemical additives or oxygen to quench triplets;[39, 63] the introduction of triplet assistant molecules for scavenging triplets generated from lasing dyes;[64, 65] the use of lasing dyes with very fast triplets relaxation.[66] Actually, the most ideal condition is to fully utilize the frozen triplets for laser actions, which is beneficial for reducing the laser thresholds and reinforcing the laser stability, in particular of the electrical-pumping devices. However, it ought to be noticed that most of the organic laser works are on the basis of fluorescent emitters, and the progress of exciton utilization efficiency far lags.

1.4.4 TADF molecules in organic lasers

As the stimulated emission, the performance of organic lasers is tightly relevant to the Einstein B coefficient, which is proportional to the radiative decay rate k_r :

$$B \propto \frac{c^3}{8\pi h v^3} k_r, \text{ (Eq. 1.15)}$$

where c is the velocity of light, h is Planck's constant, v is the frequency of light. Moreover, the ASE or laser threshold (E_{th}) is inversely proportional to B:

$$E_{th} \propto \frac{1}{B}, \text{ (Eq. 1.16)}$$

Therefore, because of the slow radiative rate nature (k_r <10^7 s^{-1}), the 2nd generation phosphorescence is not suitable to be used as laser gain mediums. Much attention has been paid to TADF, which preserves a part of features of fluorescent emission with a moderate k_r. Unfortunately, up to now, very limited TADF candidates can show ASE in solid-state films,[67-71] which mainly results from a contradiction between obtaining a small ΔE_{ST} and a large k_r. As discussed above, a small ΔE_{ST} can be achieved by suppressing the HOMO/LUMO wavefunction overlap (**Figure 1-12**), which is subsequently connected with a decrease of the k_r from the following equations:

$$k_r(S_1 - S_0) = 2Cv^3n^3|\overrightarrow{\mu_{HL}}|^2, \text{(Eq. 1.17)}$$

where $v = \Delta E(S_1 - S_0)/h$ is the transition frequency, n is the refractive index, $C = 16\pi^3/(3\varepsilon_0 hc^3)$ denotes a numerical constant, ε_0 is the vacuum permittivity, h is Planck's constant, and c is the velocity of light. $\overrightarrow{\mu_{HL}}$ is the transition dipole moment from $S_1 - S_0$, which can be expressed as:

$$\overrightarrow{\mu_{HL}} = e \int \varphi_H(\vec{r})\varphi_L(\vec{r})d^3r, \text{(Eq. 1.18)}$$

where φ_H and φ_L represent the HOMO and LUMO wavefunctions, respectively, $\vec{r}$ is the dipole vector and e is the electron charge. So, the relationship between $k_r(S_1 - S_0)$ and HOMO/LUMO wavefunction can be summarized as:

$$k_r(S_1 - S_0) = 2e^2Cv^3n^3|\varphi_H(\vec{r})\varphi_L(\vec{r})d^3r|^2, \text{(Eq. 1.19)}$$

Compared to Eq.1.10, it seems a competition between obtaining a small ΔE_{ST} and a large k_r, implying that the conventional charge-transfer (CT) type TADF molecules are commonly not sufficient to realize laser actions with low thresholds.

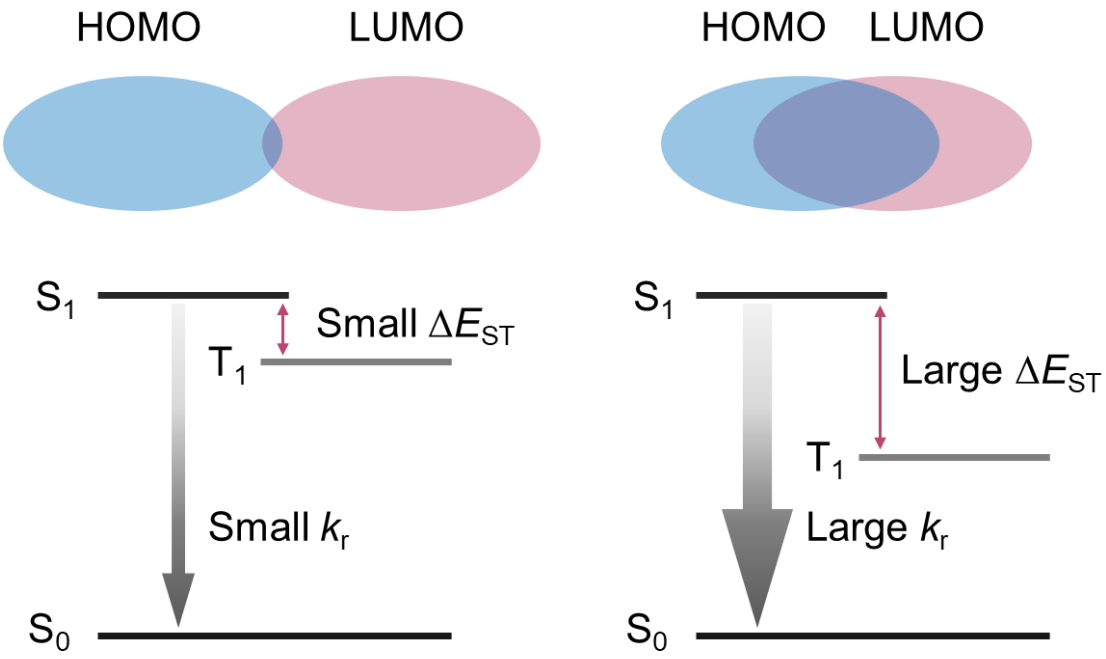

Figure 1-12. Effect of HOMO/LUMO wavefunctions overlaps on the singlet-triplet splitting (ΔE_{ST}) and radiative decay rate (k_r).

As an example in **Figure 1-13**, an unconjugated spirobifluorene was considered as an efficient bridge to build up the D-A separated molecule. Here, Cz-SBF was employed as the core, where different substituents were modified. Initially, when electron-accepting moieties, cyano-groups were functionalized in the one side of the spirobifluorene, the frontier molecular orbitals are thereby separated on the two perpendicular fluorene sites. Resultantly, the negligible wavefunction overlaps induce a small ΔE_{ST} with TADF for DPA-SBF, while quenching the ASE or laser properties by sacrificing the radiative transition rate. By comparison, when a phenyl-group was inserted between diphenylamine and spirobifluorene, the extension of conjugated length led to a change of electronic wavefunction density and distribution with a considerable orbital overlap. Therefore, the modified molecule CzP-SBF exhibited a remarkably low ASE threshold of 0.4 μJ cm^{-2}, unfortunately without the TADF property. Therefore, the conjugated and rigid molecular structure without a distinct D-A separation will be preferred for laser molecular design.

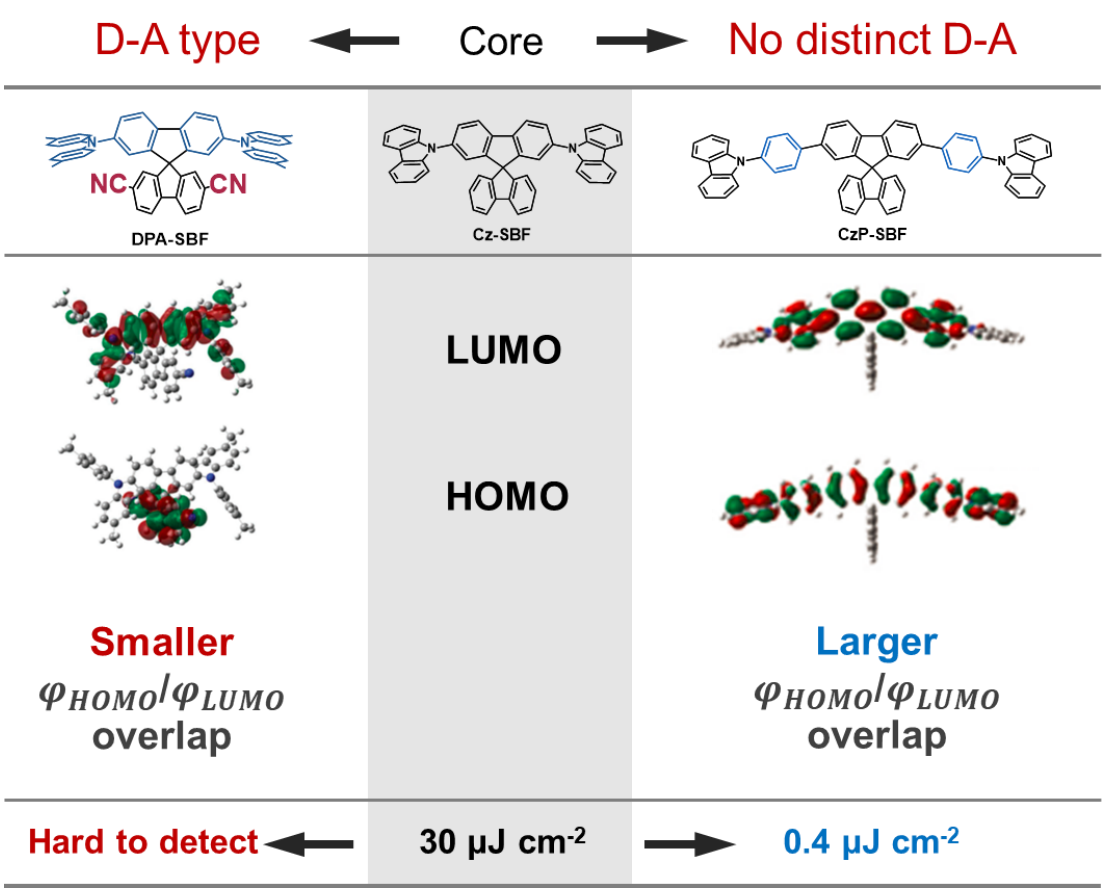

Figure 1-13. Molecular structures, molecular frontier orbitals and ASE/laser performance of Cz-SBF, DPA-SBF, and CzP-SBF, respectively.[72] The calculated wavefunctions are reproduced from Ref. 72.

1.5 Purpose and outline

As discussed above, the development of high-performing OLEDs and OSLDs is intrinsically to manipulate the spin-forbidden triplet behaviors. Besides the scavenging of triplets to enhance the laser action in the fluorescence laser system, improving the generated exciton utilization efficiency, especially for possible strategies to activate the frozen triplets has been emphasized. Within the past three decades, 100% IQE has been achieved in the 2nd generation phosphorescent OLEDs and the cutting-edge 3rd generation TADF OLEDs. Nevertheless, the progress of exciton utilization efficiency for organic lasers is still far lagged. Up to now, most efforts have been dedicated to fluorescent laser dyes, implying that scavenging or "killing" the detrimental triplets is indispensable to achieve laser actions.[73] Though the indication of electrical-pumping OSLDs has been recently realized,[43] the extremely high laser threshold induces very poor operational stability. Thus, harvesting and contributing triplets to the laser action is what we are striving for. Unfortunately, owing to the slow radiative rate nature, phosphorescent emitters cannot be employed as laser dyes. Therefore, attention has been paid to the 3rd generation TADF emitters, which reserves part of the fluorescence features. Nevertheless, the principle of TADF molecule design is based on the D/ A twisted configuration for the separated wavefunctions, which helps the formation of a CT state with a weak oscillator strength (*f*) and low radiative rate. Up to now, there are very rare TADF candidates, which show ASE, and no distributed feedback (DFB) lasers based on TADF molecules have ever been reported so far. Also, the design principle of D-A type molecules toward ASE/laser actions is still vague; the underlying intramolecular interactions that influence the electronic properties have not been systematically investigated.

Furthermore, as EL from TADF molecules has achieved 20% EQEs over the visible light regime, the color purity has been emphasized for a wider color gamut as well. In common, TADF molecules possess a very wide full-width at half-maximum (FWHM, >70 nm), which results from the structural and vibronic relaxations in the

flexible D-A structures. Therefore, how to improve the color purity with smaller FWHM is also a long-term challenge.

Therefore, this thesis focuses on the investigation of intramolecular interactions in D-A type molecules, which torches the promising molecular design from fluorescence to TADF molecules.

In **Chapter 2**, functional substituents with an increasing electron-donating capability were incorporated into a DCNP-core. The suppressed wavefunction delocalization maintained the priority of a locally-excited (LE) state, while a weak CT state induced by D/A interplays guaranteed a moderate ΔE_{ST} to feasibly build up the triplet scavenging system. As a consequence, an excellent laser performance from 2nd-order and mixed-order DFBs could be achieved. Also, there was negligible efficiency rolloff that took place in the corresponding OLED under a high current density injection.

In **Chapter 3**, laser dyes based on a strong D-A type were designed by inserting a functional fluorene spacer. Here, the fluorene spacer with long alkyl chains could effectively increase the conjugation length and adjust the wavefunction distribution, thereby resulting in a hybrid locally charge transfer (HLCT) state. Benefitting from this skeleton, organic lasers with emission ranging from yellow (555 nm) to NIR (845 nm) were realized by tuning the relative D/A interplay strength.

In **Chapter 4**, a quasi-planar D-A type molecular structure was proposed, where an intramolecular lock was inserted to reduce and fix the torsion angle of the D-A planes. Resultantly, the suppression of structural and vibronic relaxation led to a narrowband emission (~40 nm). Furthermore, because of the rational manipulation of HOMO/LUMO distance, the designed molecules exhibit not only TADF properties with high EQEs over 10%, but also a promising laser performance with a low threshold around 1 μJ cm^{-2}.

In **Chapter 5**, an entirely planar molecular skeleton CzBN based on multiple resonance (MR) effects was put forward. Different from the conventional TADF molecules composed of D/A moieties, electron-accepting and donating capabilities were localized at the opposite B/N atoms, respectively, which triggered the TADF activity. Moreover, benefitting from the TADF property and the rigid structure, EL

performance with 10% EQE and a narrow FWHM of 30 nm was thereby obtained. Encouragingly, because of the large *f*, a good DFB laser with a remarkably low threshold of around 1 μJ cm^{-2} could be achieved in this TADF molecule.

By systematically clarifying the substituent effects, functional spacers between D-A motifs, intramolecular locked quasi-planar D-A configuration, as well as the planar MR effects, I realized TADF-based DFB lasers with low thresholds. A detailed discussion on the aforementioned works will be presented in four chapters as follows:

References

[1] D. F. Walls, *Nature* **1979**, *280*, 451.

[2] C. P. Flynn, A. M. Stoneham, *Phys. Rev. B* **1970**, *1*, 3966.

[3] J. H. Poynting, *Proceedings of the Royal Society of London. Series A, Containing Papers of a Mathematical and Physical Character* **1909**, *82*, 560.

[4] F. Selleri, *Wave-Particle Duality* **1992**, Springer Science+Business Media.

[5] T. L. Dimitrova, A. Weis, *Am. J. Phys.* **2008**, *76*, 137.

[6] S. W. Hell, J. Wichmann, *Opt. Lett.* **1994**, *19*, 780.

[7] P. W. Milonni, *Am. J. Phys.* **1984**, *52*, 340.

[8] R. C. Hilborn, *Am. J. Phys.* **1982**, *50*, 982.

[9] L. G. Piper, K. W. Holtzclaw, B. D. Green, W. A. M. Blumberg, *J. Chem. Phys.* **1989**, *90*, 5337.

[10] J. R. Lakowicz, *Principles of Fluorescence Spectroscopy* **1999**, 1.

[11] C. W. Tang, S. A. VanSlyke, *Appl. Phys. Lett.* **1987**, *51*, 913.

[12] P. P. Sorokin, J. R. Lankard, *IBM J. Res. Dev.* **1966**, *10*, 162.

[13] G. N. Lewis, M. Kasha, *J. Am. Chem. Soc.* **1944**, *66*, 2100.

[14] M. A. Baldo, D. F. O'Brien, Y. You, A. Shoustikov, S. Sibley, M. E. Thompson, S. R. Forrest, *Nature* **1998**, *395*, 151.

[15] M. L. Saviotti, W. C. Galley, *Proc. Natl. Acad. Sci.* **1974**, *71*, 4154.

[16] H. Sternlicht, G. C. Nieman, G. W. Robinson, *J. Chem. Phys.* **1963**, *38*, 1326.

[17] M. N. Berberan-Santos, J. M. M. Garcia, *J. Am. Chem. Soc.* **1996**, *118*, 9391.

[18] M. Pope, H. P. Kallmann, P. Magnante, *J. Chem. Phys.* **1963**, *38*, 2042.

[19] B. Minaev, G. Baryshnikov, H. Agren, *Phys. Chem. Chem. Phys.* **2014**, *16*, 1719.

[20] H. Uoyama, K. Goushi, K. Shizu, H. Nomura, C. Adachi, *Nature* **2012**, *492*, 234.

[21] F. P. Schäfer, W. Schmidt, J. Volze, *Appl. Phys. Lett.* **1966**, *9*, 306.

[22] B. H. Soffer, B. B. McFarland, *Appl. Phys. Lett.* **1967**, *10*, 266.

[23] O. G. Peterson, S. A. Tuccio, B. B. Snavely, *Appl. Phys. Lett.* **1970**, *17*, 245.

[24] F. Hide, B. J. Schwartz, M. A. Díaz-García, A. J. Heeger, *Chem. Phys. Lett.* **1996**,

256, 424.

[25] N. Tessler, G. J. Denton, R. H. Friend, *Nature* **1996**, *382*, 695.

[26] V. G. Kozlov, V. Bulović, P. E. Burrows, S. R. Forrest, *Nature* **1997**, *389*, 362.

[27] R. Xia, G. Heliotis, Y. Hou, D. D. C. Bradley, *Org. Electron.* **2003**, *4*, 165.

[28] I. D. W. Samuel, G. A. Turnbull, *Chem. Rev.* **2007**, *107*, 1272.

[29] W.-Y. Lai, R. Xia, Q.-Y. He, P. A. Levermore, W. Huang, D. D. C. Bradley, *Adv. Mater.* **2009**, *21*, 355.

[30] R. Xia, W.-Y. Lai, P. A. Levermore, W. Huang, D. D. C. Bradley, *Adv. Funct. Mater.* **2009**, *19*, 2844.

[31] Y. Qian, Q. Wei, G. Del Pozo, M. M. Mroz, L. Luer, S. Casado, J. Cabanillas-Gonzalez, Q. Zhang, L. Xie, R. Xia, W. Huang, *Adv. Mater.* **2014**, *26*, 2937.

[32] S. Yuyama, T. Nakajima, K. Yamashita, K. Oe, *Appl. Phys. Lett.* **2008**, *93*, 023306.

[33] D. Schneider, T. Rabe, T. Riedl, T. Dobbertin, O. Werner, M. Kröger, E. Becker, H. H. Johannes, W. Kowalsky, T. Weimann, J. Wang, P. Hinze, A. Gerhard, P. Stössel, H. Vestweber, *Appl. Phys. Lett.* **2004**, *84*, 4693.

[34] T. Aimono, Y. Kawamura, K. Goushi, H. Yamamoto, H. Sasabe, C. Adachi, *Appl. Phys. Lett.* **2005**, *86*, 071110.

[35] T. Matsushima, S. Yoshida, K. Inada, Y. Esaki, T. Fukunaga, H. Mieno, N. Nakamura, F. Bencheikh, M. R. Leyden, R. Komatsu, C. Qin, A. S. D. Sandanayaka, C. Adachi, *Adv. Funct. Mater.* **2019**, *29*, 1807148.

[36] B. S. B. Karunathilaka, U. Balijapalli, C. A. M. Senevirathne, S. Yoshida, Y. Esaki, K. Goushi, T. Matsushima, A. S. D. Sandanayaka, C. Adachi, *Nat. Commun.* **2020**, *11*, 4926.

[37] T. Rabe, K. Gerlach, T. Riedl, H. H. Johannes, W. Kowalsky, J. Niederhofer, W. Gries, J. Wang, T. Weimann, P. Hinze, F. Galbrecht, U. Scherf, *Appl. Phys. Lett.* **2006**, *89*, 081115.

[38] A. S. D. Sandanayaka, T. Matsushima, F. Bencheikh, K. Yoshida, M. Inoue, T. Fujihara, K. Goushi, J. C. Ribierre, C. Adachi, *Sci. Adv.* **2017**, *3*, e1602570.

[39] A. S. D. Sandanayaka, L. Zhao, D. Pitrat, J.-C. Mulatier, T. Matsushima, C.

Andraud, J.-H. Kim, J.-C. Ribierre, C. Adachi, *Appl. Phys. Lett.* **2016**, *108*, 223301.

[40] T. Matsushima, C. Adachi, *Jpn. J. Appl. Phys.* **2007**, *46*, L1179.

[41] T. Matsushima, C. Adachi, *Jpn. J. Appl. Phys.* **2007**, *46*, L861.

[42] Y. Setoguchi, C. Adachi, *J. Appl. Phys.* **2010**, *108*, 064516.

[43] A. S. D. Sandanayaka, T. Matsushima, F. Bencheikh, S. Terakawa, W. J. Potscavage, C. Qin, T. Fujihara, K. Goushi, J.-C. Ribierre, C. Adachi, *Appl. Phys. Express* **2019**, *12*, 061010.

[44] G. Somasundaram, A. Ramalingam, *Chem. Phys. Lett.* **2000**, *324*, 25.

[45] T. G. Pavlopoulos, *Prog. Quantum Electron.* **2002**, *26*, 193.

[46] F. López Arbeloa, J. Bañuelos, V. Martínez, T. Arbeloa, I. López Arbeloa, *Int. Rev. Phys. Chem.* **2005**, *24*, 339.

[47] F. Liang, H. Zeng, Z. Sun, Y. Yuan, Z. Yao, Z. Xu, *J. Opt. Soc. Am. B* **2001**, *18*, 1841.

[48] A. Costela, I. García-Moreno, M. Pintado-Sierra, F. Amat-Guerri, R. Sastre, M. Liras, F. L. Arbeloa, J. B. Prieto, I. L. Arbeloa, *J. Phys. Chem. A* **2009**, *113*, 8118.

[49] C. F. A. Gómez-Durán, I. García-Moreno, A. Costela, V. Martin, R. Sastre, J. Bañuelos, F. López Arbeloa, I. López Arbeloa, E. Peña-Cabrera, *Chem. Commun.* **2010**, *46*, 5103.

[50] J. C. Forgie, P. J. Skabara, I. Stibor, F. Vilela, Z. Vobecka, *Chem. Mater.* **2009**, *21*, 1784.

[51] I. Esnal, I. Valois-Escamilla, C. F. A. Gómez-Durán, A. Urías-Benavides, M. L. Betancourt-Mendiola, I. López-Arbeloa, J. Bañuelos, I. García-Moreno, A. Costela, E. Peña-Cabrera, *Chem. Phys. Chem.* **2013**, *14*, 4134.

[52] G. Tsiminis, Y. Wang, P. E. Shaw, A. L. Kanibolotsky, I. F. Perepichka, M. D. Dawson, P. J. Skabara, G. A. Turnbull, I. D. W. Samuel, *Appl. Phys. Lett.* **2009**, *94*, 243304.

[53] J. C. Ribierre, G. Tsiminis, S. Richardson, G. A. Turnbull, I. D. W. Samuel, H. S. Barcena, P. L. Burn, *Appl. Phys. Lett.* **2007**, *91*, 081108.

[54] S. M. Morris, M. M. Qasim, D. J. Gardiner, P. J. W. Hands, F. Castles, G. Tu, W.

T. S. Huck, R. H. Friend, H. J. Coles, *Opt. Mater.* **2013**, *35*, 837.

[55] W.-Y. Lai, R. Xia, D. D. C. Bradley, W. Huang, *Chem. Eur. J.* **2010**, *16*, 8471.

[56] S. Varghese, S. K. Park, S. Casado, R. Resel, R. Wannemacher, L. Lüer, S. Y. Park, J. Gierschner, *Adv. Funct. Mater.* **2016**, *26*, 2349.

[57] A. L. Kanibolotsky, F. Vilela, J. C. Forgie, S. E. T. Elmasly, P. J. Skabara, K. Zhang, B. Tieke, J. McGurk, C. R. Belton, P. N. Stavrinou, D. D. C. Bradley, *Adv. Mater.* **2011**, *23*, 2093.

[58] R. Xia, G. Heliotis, P. N. Stavrinou, D. D. C. Bradley, *Appl. Phys. Lett.* **2005**, *87*, 031104.

[59] M. Anni, S. Lattante, *J. Phys. Chem. C* **2015**, *119*, 21620.

[60] Y. Xu, G. Hai, H. Xu, H. Zhang, Z. Zuo, Q. Zhang, R. Xia, C. Sun, J. Castro-Smirnov, A. Sousaraei, S. Casado, M. R. Osorio, D. Granados, I. Rodriguez, J. Cabanillas-Gonzalez, *Adv. Opt. Mater.* **2018**, *6*, 1800263.

[61] M. Lehnhardt, T. Riedl, T. Weimann, W. Kowalsky, *Phys. Rev. B* **2010**, *81*, 165206.

[62] D. Kasemann, R. Brückner, H. Fröb, K. Leo, *Phys. Rev. B* **2011**, *84*, 115208.

[63] J. B. Marling, D. W. Gregg, L. Wood, *Appl. Phys. Lett.* **1970**, *17*, 527.

[64] Y. Zhang, S. R. Forrest, *Phys. Rev. B* **2011**, *84*, 241301.

[65] B. S. B. Karunathilaka, U. Balijapalli, C. A. M. Senevirathne, Y. Esaki, K. Goushi, T. Matsushima, A. S. D. Sandanayaka, C. Adachi, *Adv. Funct. Mater.* **2020**, *30*, 2001078.

[66] A. S. D. Sandanayaka, T. Matsushima, F. Bencheikh, K. Yoshida, M. Inoue, T. Fujihara, K. Goushi, J.-C. Ribierre, C. Adachi, *Sci. Adv.* **2017**, *3*, e1602570.

[67] H. Nakanotani, T. Furukawa, T. Hosokai, T. Hatakeyama, C. Adachi, *Adv. Opt. Mater.* **2017**, *5*, 1700051.

[68] D.-H. Kim, A. D'Aléo, X.-K. Chen, A. D. S. Sandanayaka, D. Yao, L. Zhao, T. Komino, E. Zaborova, G. Canard, Y. Tsuchiya, E. Choi, J. W. Wu, F. Fages, J.-L. Brédas, J.-C. Ribierre, C. Adachi, *Nat. Photon.* **2018**, *12*, 98.

[69] H. Ye, D. H. Kim, X. Chen, A. S. D. Sandanayaka, J. U. Kim, E. Zaborova, G. Canard, Y. Tsuchiya, E. Y. Choi, J. W. Wu, F. Fages, J.-L. Bredas, A. D'Aléo,

J.-C. Ribierre, C. Adachi, *Chem. Mater.* **2018**, *30*, 6702.

[70] Z. Zhou, C. Qiao, K. Wang, L. Wang, J. Liang, Q. Peng, Z. Wei, H. Dong, C. Zhang, Z. Shuai, Y. Yan, Y. S. Zhao, *Angew. Chem. Int. Ed.* **2020**, *59*, 21677.

[71] Y. Li, K. Wang, Q. Liao, L. Fu, C. Gu, Z. Yu, H. Fu, *Nano Lett.* **2021**, *21*, 3287.

[72] A. J. Kuehne, M. C. Gather, *Chem. Rev.* **2016**, *116*, 12823.

[73] B. S. B. Karunathilaka, U. Balijapalli, C. A. M. Senevirathne, Y. Esaki, K. Goushi, T. Matsushima, A. S. D. Sandanayaka, C. Adachi, *Adv. Funct. Mater.* **2020**, *30*, 2001078.

Chapter 2. Suppressed delocalization of wavefunction distribution in the donor-acceptor structure for organic lasers and EL under high current injection

2.1 Introduction

The reasonable incorporation of the functional moieties into an emissive core plays a crucial role in determining the light-emitting properties, especially for laser dyes, because the infused electron-donating or -accepting substituents would significantly reorganize the electronic wavefunction distributions.[1-7] If the distinct D and A interplay leads to the separation of the HOMO and LUMO along the molecular skeleton, the reinforced intramolecular charge-transfer (ICT) state would sacrifice the LE state, *f*, thereby inhibiting the laser activity.[8-13]

Recently, a laser dye, 2,6-dicyano-1,1-diphenyl-$\lambda^5\sigma^4$-phosphinine (DCNP), with a relatively moderate ΔE_{ST} was found to be a good candidate for constructing an efficient host-guest lasing system, which enabled the selection of host materials easier to scavenge the triplets for better laser performance.[9, 14-17] However, in terms of the fabrication process, the minimal molecular weight of DCNP will bring a detrimental effect on a vacuum deposition system.[18] Moreover, the low molecular weight caused a lower decomposition temperature, which would accelerate the instability during the thermal-evaporation process or under the intense photo- or electrical excitation.[19] On the other hand, the severe spontaneous aggregation-caused quenching (ACQ) effect of DCNP resulted in a decrease in PLQY, which accordingly declined the laser and OLED performance.[20-23] So, the rational substituent in this core ought to be emphasized.

In terms of the fluorescent laser dye, the generated triplets cannot be utilized because of the spin-forbidden rule.[24-26] Therefore, the rational manipulation of long-lived triplets with the aim of suppressing triplet-caused annihilation, plays a crucial role in realizing stable laser actions.[27-29] Within the past decades, numerous efforts have been devoted to a promising organic molecule BSBCz,[30-34] which owns the remarkable photophysical properties, such as the high PLQY~100% and the high k_r~10^9 s^{-1} in doped films.[35] More importantly, the nonradiative relaxation lifetime of triplets of BSBCz is comparatively short (~224 ns), which effectively prevents the detrimental triplet-accumulation-inducing quenching such as STA.[36]

In this work, a cyanophenyl-moiety with the electron-withdrawing capability was conjugated with the DCNP core at a *para*-position. Owing to the bicyano-group in the DCNP-core, the cyanophenyl-moiety exhibited relatively weaker electron-donating characteristics, so the relatively weak D/A interplay in this new molecule DCNP-pCN partially induced only slight delocalization of HOMO wavefunction from the DCNP-core toward the cyanophenyl-moiety. Thus, the large HOMO/LUMO wavefunction overlap still concentrated on the DCNP-core, which guaranteed the comparatively high f of 0.1028 compared with the pristine DCNP (0.1180), thereby ensuring a high radiative decay rate (k_r~10^8 s^{-1}) for laser activity. Interestingly, the detrimental weak CT state to some degree maintained the relatively moderate ΔE_{ST} of 0.45 eV. For comparison, two DCNP-based derivatives conjugated with strong donor fragments, such as phenyl-carbazol (PhCz) and triphenylamine (TPA) groups, exhibited much smaller f and k_r, which thus induced poorer lasing activities. Herein, because of the well-matched energy levels and the excellent triplet scavenging capability, BSBCz was employed as the host matrix, as well as the triplet scavenger for DCNP-pCN. In particular, the emission from DCNP-pCN was slightly redshifted (λ_{PL}~516.0 nm) compared with the emission from pure DCNP (λ_{PL}~508.0 nm). Thus, the limited spectral shifting of DCNP-pCN was mediated by increasing the conjugated length and the weak D/A interplay. Therefore, with the effective triplet scavenging and optimized molecular size, the novel lasing dye DCNP-pCN exhibited remarkably high ASE performance, with its excellent stability, demonstrating no emission intensity degradation under the intense pulse-photoexcitation over four hours. Furthermore, when DCNP-pCN was incorporated into a 2^{nd}-order or mixed-order DFB resonator, the high-quality green laser could be obtained, with a low laser threshold of ~2.0 μJ cm^{-2}, which could be evidently confirmed by the polarization, near-field and far-field characterization. Owing to the high PLQY value (exceeding 90%) of a DCNP-pCN:BSBCz blend film, the corresponding OLEDs based on an extraordinarily thick homogeneous structure could exhibit EQEs ~2.0%, without marked efficiency rolloff under high current density injection (>17,000 mA cm^{-2}). It was worth noting that there was no STA in PL or EL mode under the extremely high pulsed photoexcitation or

current injection over 17,000 mA cm^{-2}. The aforementioned properties would torch a potential avenue to the electrical-pumping OSLDs with even higher performance in the future.

2.2 Results and discussion

2.2.1 Molecular structure and characterization

As displayed in **Figure 2-1**, a green-emitting dye DCNP-pCN was composed of the reported DCNP core and an electron-accepting nitrile-group at the *para*-position of the linker benzene ring. An orange emitter 1,1-diphenyl-4-(9-phenyl-9H-carbazol-3-yl)-1λ^5-phosphinine-2,6-dicarbonitrile (DCNP-PhCz) contained direct connection of DCNP at 3-position of the 9-phenyl-9H-carbazole donor unit. A red-emitting dye 4-(4-(diphenylamino)phenyl)-1,1-diphenyl-15-phosphinine-2,6-dicarbonitrile (DCNP-TPA) was composed of DCNP and an electron-donating diphenylamine-unit at the *para*-position of the linker benzene ring. These dyes were synthesized by $PdCl_2(PPh_3)_2$ catalyzed Suzuki-cross coupling reaction of intermediate BrDCNP and respective boronic acids or esters.

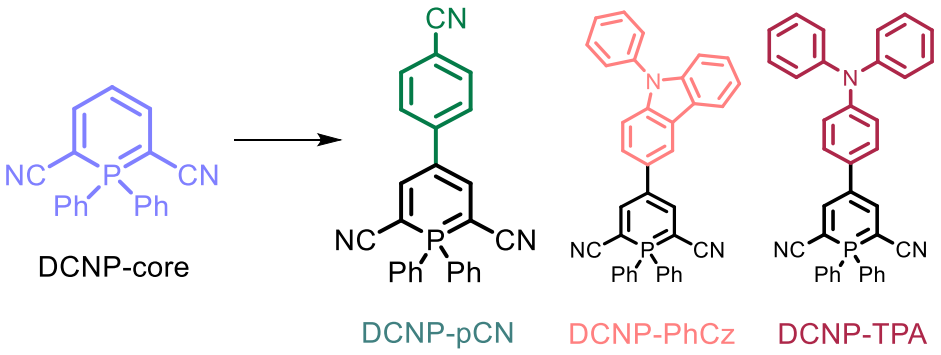

Figure 2-1. (a) Molecular design of organic lasing dyes DCNP-pCN, DCNP-PhCz, and DCNP-TPA.

2.2.2 Theoretical calculation

To initially predict the potential electronic properties of DCNP-pCN, density functional theory (DFT) simulation was carried out to calculate the HOMO and LUMO

wavefunction distribution of the S_1 and T_1 geometries in **Figure 2-2**. Because of the strong electron-affiliation capability of the two cyano-groups, it was noticeable that the LUMO wavefunction was mainly concentrated on the DCNP-core and slightly distributed at the two 1,1-diphenyl-rings connected to the phosphinine. In parallel, owing to the increased conjugated length and the electron-donating capability of the adding substituents, the HOMO wavefunction was evidently extended along the phenyl-ring to the end-cap. Benefitting from the introduction of another cyano-group at the *para*-position of phenyl-bridge, the intrinsic electron-withdrawing property will effectively prevent the HOMO/LUMO separation, then suppressing the formation of a CT state to some degree. By comparison, DCNP-PhCz and DCNP-TPA with stronger electron-donating moieties tend to have a larger HOMO/LUMO wavefunction separation, which could be confirmed from their shallower HOMO energy level. Thus, it can be observed in Figure 2-2 that a large HOMO/LUMO overlap still existed in DCNP-pCN, which guaranteed the large f ~0.1028 for realizing a fast k_r. In addition, because of the much stronger electron-donating capability of the PhCz and TPA moieties, the HOMO wavefunction was more concentrated on the donor fragments. Thus, the separation of HOMO/LUMO wavefunctions induced the strong CT state, which reduced the corresponding f of 0.0566 and 0.0255 for DCNP-PhCz and DCNP-TPA, respectively.

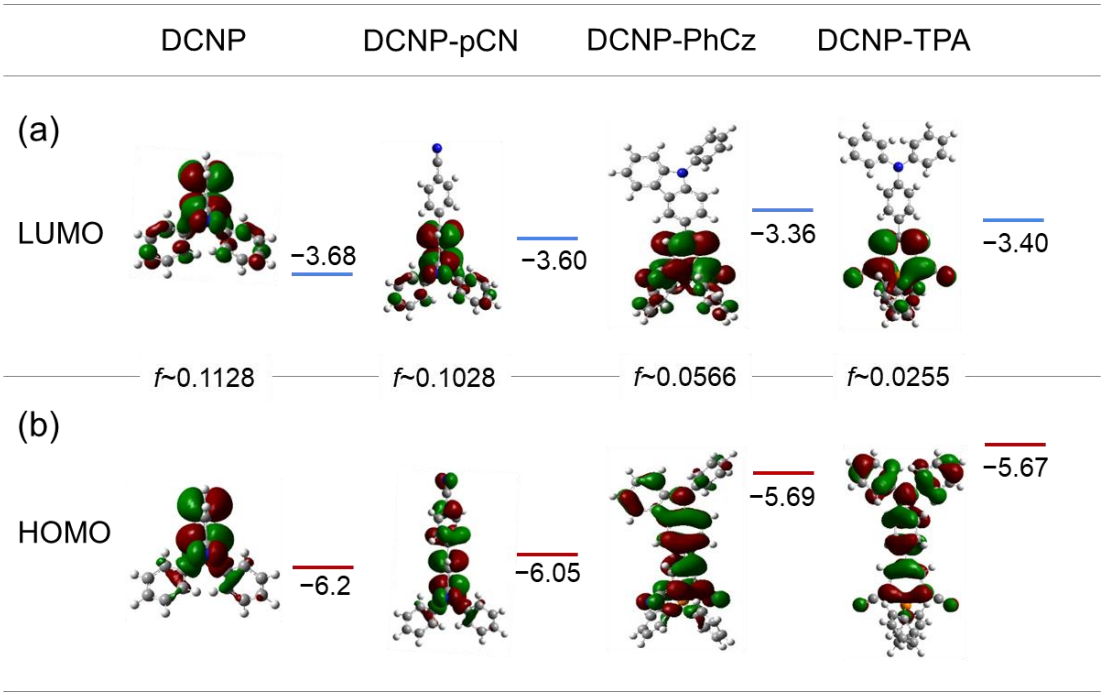

Figure 2-2. Theoretically calculated (a) LUMO and (b) HOMO wavefunction distribution of DCNP-pCN, DCNP-PhCz, and DCNP-TPA. The corresponding geometries were optimized at B3LYP/6-31G(d) level.

2.2.3 Photophysical properties

Photophysical properties were extensively investigated. **Figure 2-3(a)** subsequently displayed absorption and PL spectra of DCNP-pCN in dilute solution. As can be seen, the π-π* absorbance band tended to be weaker and broader from DCNP-pCN to DCNP-TPA, which was consistent with the features of a stronger CT state. Meanwhile, the corresponding transient PL was measured. The radiative lifetimes of DCNP-PhCz and DCNP-TPA were longer than that of DCNP-pCN [Figure 2-3(b)]. The PLQYs of DCNP-pCN, DCNP-PhCz, and DCNP-TPA were subsequently estimated as 98.9, 84.3, and 56.7%, respectively.

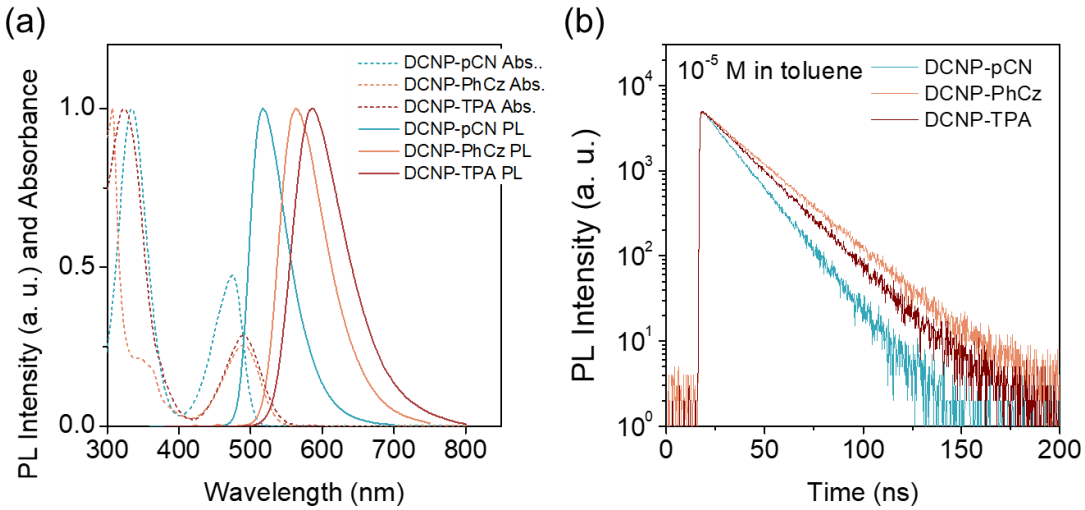

Figure 2-3. (a) UV-vis absorption, PL spectra and (b) transient PL decay spectra of DCNP-pCN, DCNP-PhCz, and DCNP-TPA measured at room temperature in toluene.

Comparing with the PL spectra in toluene, there was a very weak PL peak around 460 nm in a 1.0 wt% DCNP-pCN-doped BSBCz film, which originates from the emission from BSBCz. However, high PLQYs exceeding 90.0% could be estimated either in films of DCNP-pCN doped into a poly(methylmethacrylate) (PMMA) or BSBCz (90.5%) host at a low concentration of 1.0 wt% as shown in **Figure 2-4**. As expected, DCNP-PhCz and DCNP-TPA based blend films owned lower PLQYs of 73.1 and 54.3%, respectively.

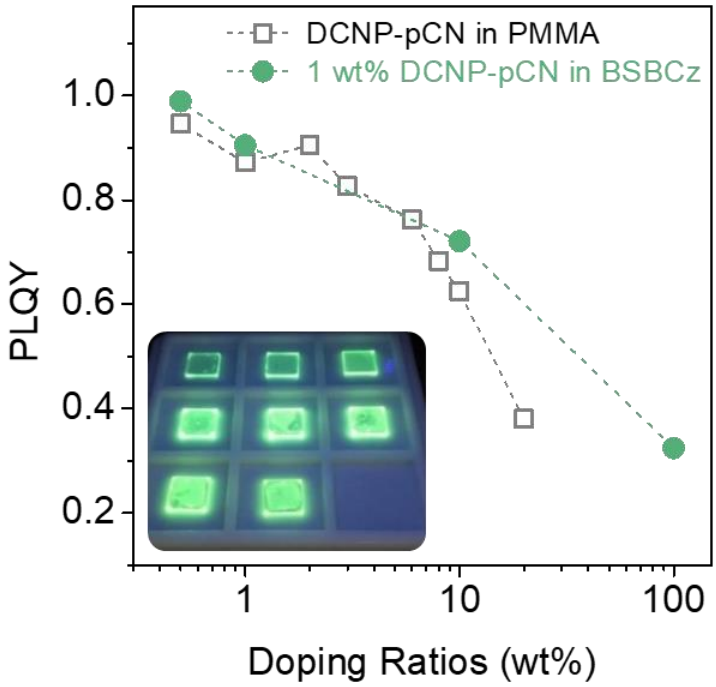

Figure 2-4. Plot of PLQYs as a function of diverse DCNP-pCN-doped concentrations in PMMA, and BSBCz blend films, respectively.

The phosphorescence emission at the low temperature (77 K) was accordingly measured. At the monomolecular state (10^{-5} M in toluene), the triplet energy levels of DCNP-pCN, DCNP-PhCz, and DCNP-TPA were estimated at 2.16, 2.00, and 1.94 eV, respectively, from the spectral onset of the shorter-wavelength side. These corresponding triplet energy levels were higher than that of BSBCz (T_1=1.48 eV). Benefitting from the large singlet-triplet energy gap and the very fast nonradiative relaxation of the triplets, BSBCz was employed as the host and triplet scavenger at the same time. Thus, as expected, there was no phosphorescence emission signal in the 1.0 wt% DCNP-pCN:BSBCz system (**Figure 2-5**). The data of photophysical properties were summarized in **Table 2-1**.

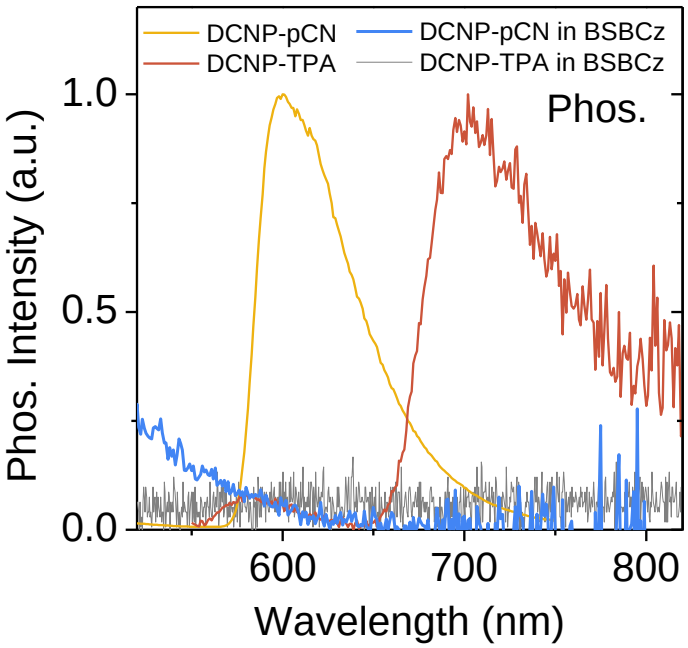

Figure 2-5. Phosphorescence of DCNP-pCN and DCNP-TPA in toluene and, 1 wt% DCNP-pCN: BSBCz and 1 wt% DCNP-TPA: BSBCz blend films at low temperature (77 K).

Table 2-1. Photophysical properties of DCNP-pCN, DCNP-PhCz and DCNP-TPA in solution and blend films

Material	λ_{PL}[a] (nm)	λ_{Abs}[a] (nm)	PLQY[a] (%)	PLQY[b] (%)	τ[b] (ns)	k_r[b] (10^8 s^{-1})	HOMO[c] (eV)	LUMO[d] (eV)
DCNP -pCN	516	505	98.9	90.5	9.9	0.92	−6.05	−3.60
DCNP -PhCz	563	533	84.3	73.1	14.9	0.49	−5.69	−3.36
DCNP -TPA	587	539	56.7	54.3	14.9	0.36	−5.67	−3.40

[a] measured in toluene solution; [b] measured in BSBCz blend film; [c] measured by photoelectron yield spectroscopy; [d] measured by subtracting the absorption onset energy from the HOMO energy.

2.2.4 ASE properties

On the basis of the aforementioned photophysical properties estimated, ASE studies of the blend films were performed to evaluate the potential of DCNP derivatives for lasers. From **Figure 2-6 (a)**, a sudden change of the emission intensity was detected, along with FWHM values of the spectra declining from 60.0 to 3.5 nm when the excitation powers were increased from 1.1 to 46.7 μJ cm^{-2}. The specific ASE spectral shape change was presented in Figure 2-6 (b). The ASE wavelength was around 523.7 nm. Based on the aforementioned evidence, the ASE threshold of the 1.0 wt% DCNP-pCN blend film was 9.2 μJ cm^{-2}. By comparison, the BSBCz blend films doped with DCNP-PhCz or DCNP-TPA at 1.0 wt% exhibited higher ASE thresholds of >36.3 μJ cm^{-2}, indicating that the localization of wavefunctions was beneficial for the laser activity. To assess the optical gain of the laser dyes, the corresponding stimulated emission cross-section (σ_{em}) has been estimated in the blend films, according to the equation 2.1:[37]

$$\sigma_{em}(\lambda) = \frac{\lambda^4 E_f(\lambda)}{8\pi n^2(\lambda) c\tau} \quad \text{. (Eq. 2.1)}$$

Here, λ is the wavelength of the emission, $E_f(\lambda)$ corresponds to the distribution of the PL efficiency and can be obtained by $\phi_f = \int E_f(\lambda) d(\lambda)$, $n(\lambda)$ is the refractive index, τ is the radiative lifetime, c is the velocity of light. For DCNP-pCN: BSBCz blend film, ϕ_f is 0.91, $n(\lambda)$ is 1.72, τ is 9.9 ns, c is 3×10^8 m s^{-1}, so, the σ_{em} at the ASE peak is around 4.7×10^{-17} cm^2. By comparison, DCNP-PhCz- or DCNP-TPA-based BSBCz blend films exhibited a smaller σ_{em} of 2.9×10^{-17} and 2.0×10^{-17} cm^2. Moreover, because of the effective triplet scavenging by BSBCz, as well as the high thermal stability, this DCNP-pCN-doped film exhibited remarkably high operational stability for ASE with continuous pulse-excitation at an excitation power of 46.0 μJ cm^{-2} [Figure 2-6 (c)]. It can be seen that there was almost no decline of the ASE intensities over four hours of continuous excitation, and the ASE spectral shapes at the initial period, 3000, 6000, 9000, and 12000 s, were respectively detected, without an obvious change or degradation as displayed in the inset of Figures 2-6 (c).

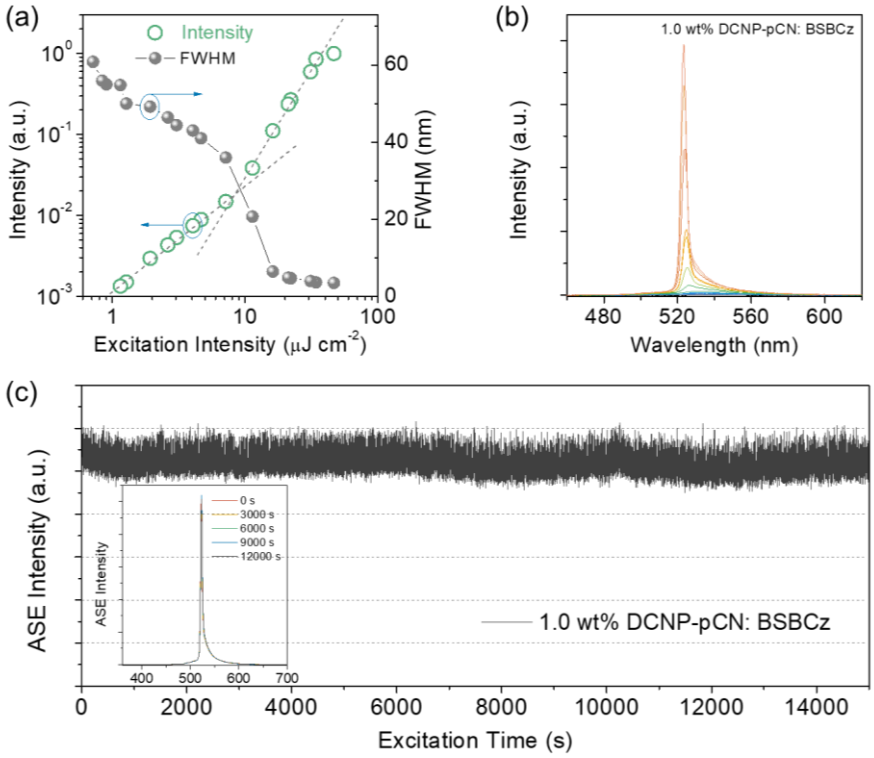

Figure 2-6. A low ASE threshold and high ASE stability were achieved in 1 wt% DCNP-pCN: BSBCz blend films. (a) Plots of emission intensity and FWHM values as a function of excitation intensity. (b) PL spectra measured from low to high excitation intensities. (c) ASE stability measured under the continuous excitation at ~50 μJ cm^{-2}. The inset of (c) was the ASE spectra measured during the stability test.

2.2.5 Second-order and mixed-order laser performance

To realize the organic lasers, 2nd-order and mixed-order DFB resonators were designed to satisfy the following Bragg equation: $m\lambda_{Bragg} = 2n_{eff}\Lambda_m$, where m denoted the order of diffraction, λ_{Bragg} was the Bragg wavelength from ASE, n_{eff} was the effective refractive index of the gain medium (1.0 wt% DCNP-pCN:BSBCz), and Λ_m indicated the corresponding period of the grating. Herein, the mixed-order DFB was composed of the alternative 1st-order (m=1) and 2nd-order (m=2) scattering regions. The 1st-order DFB structure was aimed at providing the enhanced optical feedback, while the 2nd-order DFB structure was incorporated to realize a vertically lasing outcoupling from the organic film surface. In this case, n_{eff} was 1.72, λ_{ASE} of 523.7 nm was approximately considered as λ_{Bragg}. Thus, the 1st-order DFB Λ_1 was calculated as 152.2

nm, while the Λ_2 for the 2nd-order one was accordingly calculated as 304.5 nm. Thus, a 1.0 wt% DCNP-pCN: BSBCz blend film with a thickness of 200 nm was vacuum-deposited onto the prepared DFB structure, followed by the encapsulation with an optically transparent fluoropolymer CYTOP layer and a sapphire lid in a glove box filled with nitrogen atmosphere. Afterward, the prepared DFB devices were optically pumped by a pulsed photoexcitation from a nitrogen laser source (337 nm) to evaluate the lasing performance.

As shown in **Figure 2-7**, with an increase of excitation power, the corresponding FWHM has abruptly reduced to ~0.4 nm. Meanwhile, a noticeable slope change of emission intensity occurred at the same time in both the 2nd-order DFB and mixed-order DFB devices in Figure 2-7 (a) and (c). In parallel, for mixed-order DFB devices, an extremely narrow FWHM value below 0.5 nm in the spectra was observed in Figure 2-7 (d). It is worth noting that a green lasing beam could be clearly observed from the 2nd-order DFB devices in the luminescent card [the inset diagram of Figure 2-7 (e)]. Additionally, four interference patterns from the mixed-order DFB laser also occurred in the inset diagram of Figure 2-7 (d). As a result, the laser thresholds for 2nd-order and mixed-order DFB devices were 2.6 and 2.4 μJ cm^{-2}, respectively, which were lower than the ASE threshold.

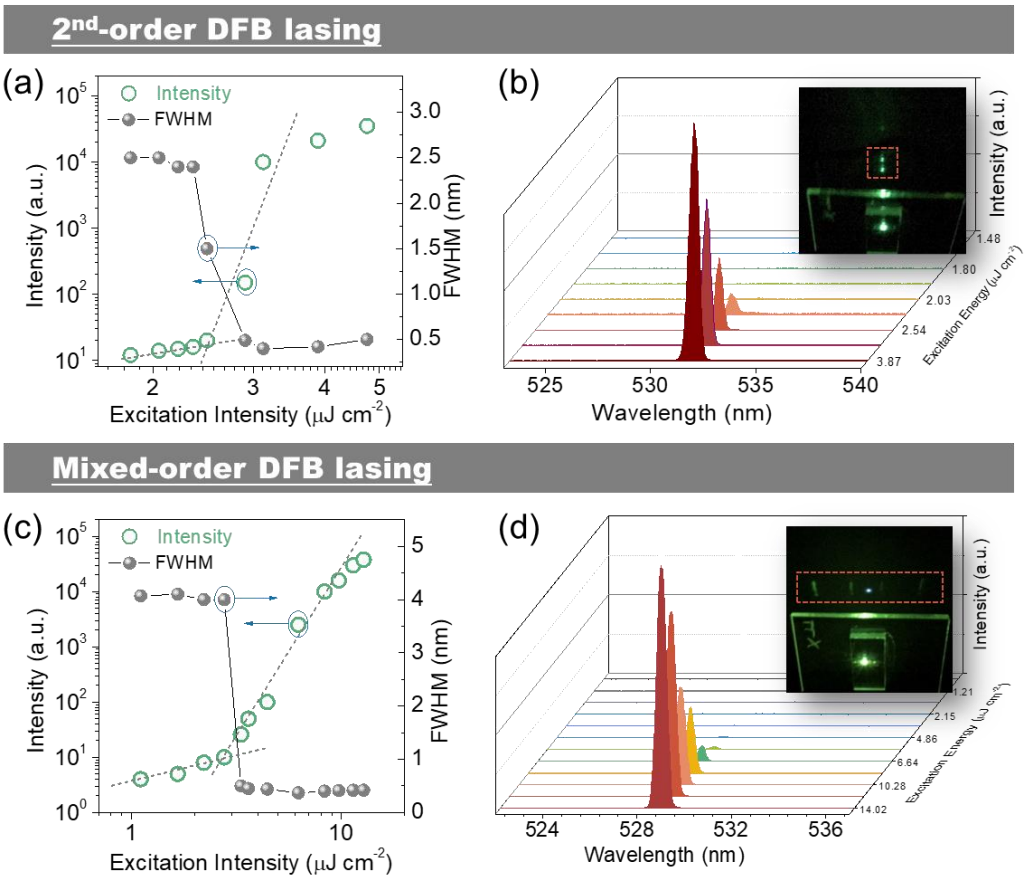

Figure 2-7. DFB lasing performance was obtained from 1 wt% DCNP-pCN: BSBCz blend films. Plots of emission intensity and FWHM values as a function of excitation intensity for (a) 2nd-order and (c) mixed-order DFB laser devices. PL spectra were measured under various excitation intensities in (b) 2nd-order and (d) mixed-order DFB laser devices. The insets in (b) and (d) were the photographs of devices showing laser beams.

To further reveal the intrinsic properties of the laser performance, time-dependent transient PL/laser properties were subsequently estimated by a streak camera in **Figure 2-8**. With an increase of excitation intensity, there was a quicker decay process as well as an abrupt decrease of a radiative lifetime to <20 ps, which was well consistent with the transition from spontaneous emission (below the laser threshold) to stimulated emission (above laser threshold). In detail, the broad spontaneous emission was obtained below the threshold. By increasing the excitation intensity, we could clearly

confirm the narrow emission within a very condensed wavelength zone, which corresponded to the stimulated lasing emission. Eventually, very narrow and intensive lasing was successfully detected by the streak camera in both 2nd-order and mixed-order DFB structures. When increasing the excitation power to trigger lasing activity, the component of spontaneous emission was largely declined, while above the threshold, the emission from both DFB devices exhibited a very steep decay process with almost one decay component, implying the stimulated emission.

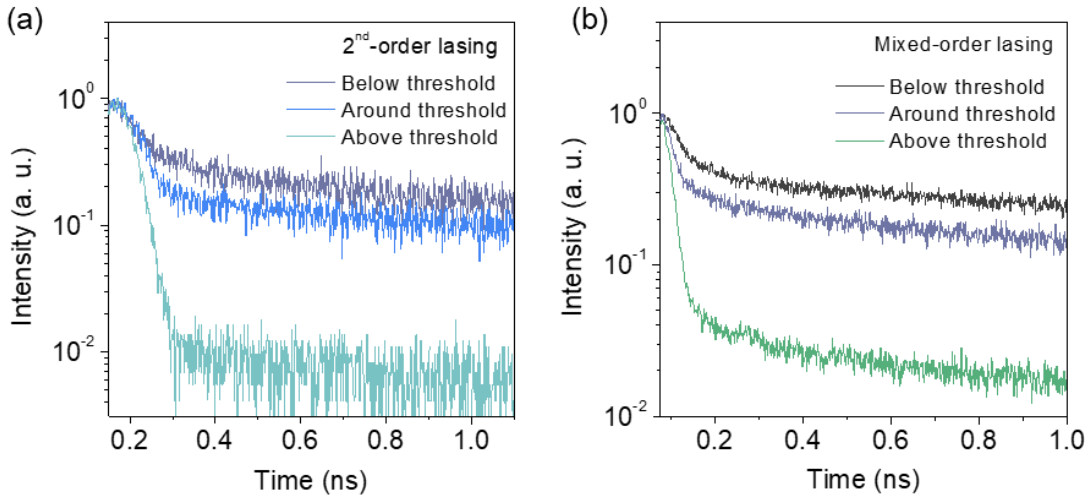

Figure 2-8. Transient PL from (a) 2nd-order and (b) mixed-order DFB lasers based on a 1 wt% DCNP-pCN: BSBCz blend film.

To further confirm the lasing activity, the investigation of polarization, far-field, and near-field interference patterns of the beam divergence from one laser device was systematically carried out. As shown in **Figure 2-9 (a)**, either 2nd-order or mixed-order DFB lasing exhibited a strong, linear transverse electric polarization, with a degree of polarization of 99.5% for 2nd-order devices and 99.8% for mixed-order devices, respectively, which was accordingly calculated from the equation: $(I_{max} - I_{min})/(I_{max} + I_{min})$, where I_{max} and I_{min} denoted the maximum intensity at 0° and the minimum intensity at 90°, respectively. As a result, the approaching unity degree value (100%) indicated the remarkable polarization characteristics of the DCNP-pCN:BSBCz

system. Moreover, further clarification of lasing activity was also confirmed by far-field interference patterns. As displayed in Figure 2-9 (b), while gradually increasing the excitation power to exceed the lasing threshold, a distinct beam signal appeared at the center of the detected camera images, indicating the intense lasing beam arising from the 2^{nd}-order DFB structures. From the mixed-order DFB structure, clear interference patterns were noticeably detected with the streak camera. In addition, the lasing beams or interference patterns could be feasibly observed by a luminescent card in front of the samples in Figure 2-9. Also, it was evident to observe the grating interference patterns from DFB lasing devices above the lasing thresholds in the near-field measurement [Figure 2-9 (c)]. Thus, the aforementioned evidence effectively verified the lasing taking place in a DCNP-pCN:BSBCz system.

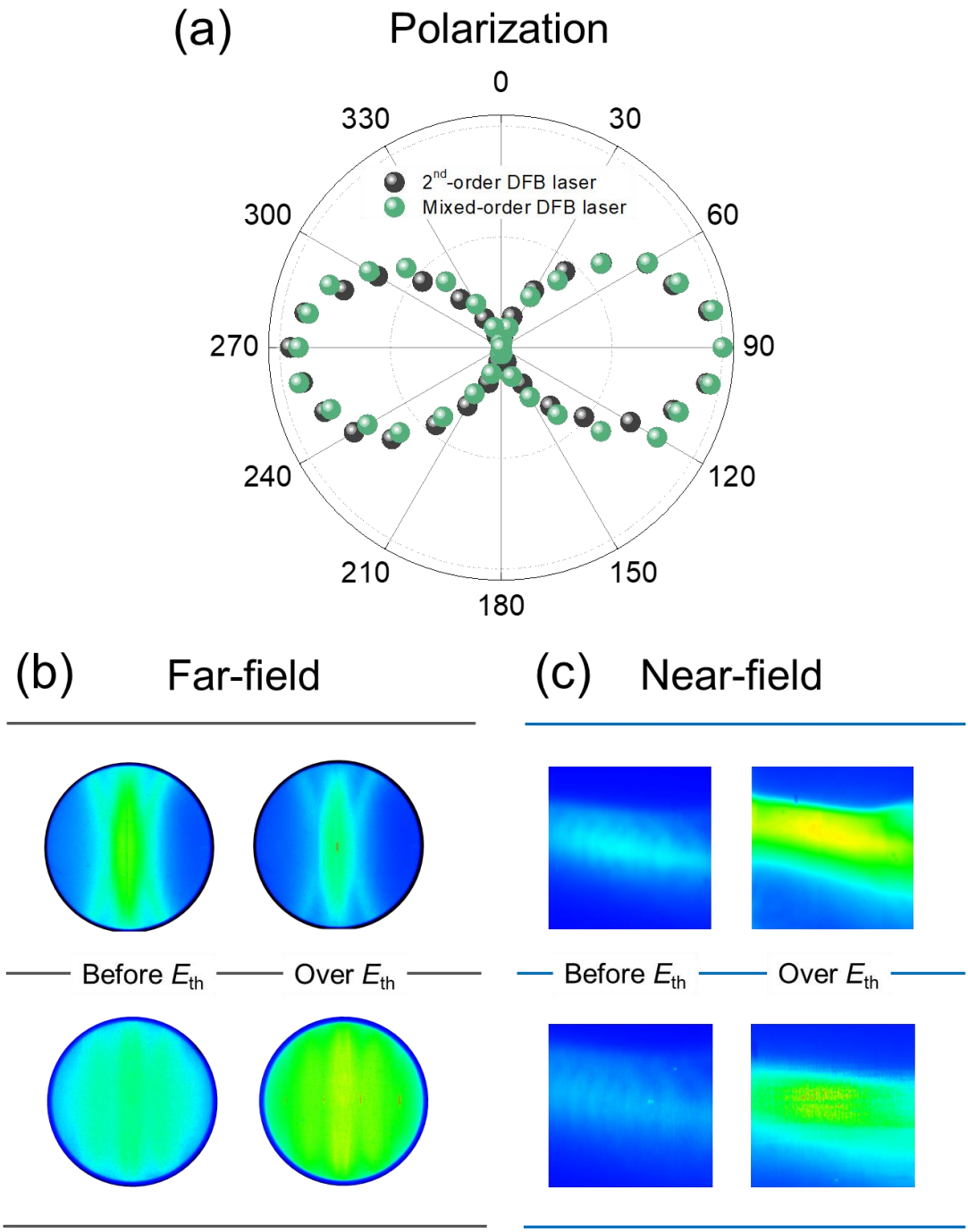

Figure 2-9. (a) Polarization plots of laser from the 2nd-order and mixed-order DFB devices. (b) Far-field and (c) near-field patterns of the 2nd-order and mixed-order DFB lasers below and above the laser thresholds.

2.2.6 EL performance of DCNP-pCN

To pursue the ultimate goal of improving OSLD performance, evaluating the EL properties of the DCNP-pCN:BSBCz system was inevitable. To improve the EQEs and suppress the efficiency rolloff under the extremely high current injection, carrier (holes and electrons) injection and transport should be well balanced to prevent the potential carrier accumulation and annihilation. Initially, I designed and fabricated hole-only devices (HODs) and electron-only devices (EODs) with a patterned indium tin oxide (ITO)-coated glass substrate. The HOD architecture was glass substrate/ITO (30 nm)/MoO_3 (10 nm)/1.0 wt% DCNP-pCN: BSBCz (180 nm)/MoO_3 (10 nm)/Al (100 nm); and the EOD architecture was glass substrate/ ITO (30 nm)/ 20.0 wt% Cs: BSBCz (30 nm)/ 1.0 wt% DCNP-pCN: BSBCz (180 nm)/Cs (30 nm)/Al (100 nm). Herein, MoO_3 was used as the HIL as well as the EBL, and Cs was doped into the BSBCz layer for reinforcing the electron-injection and transport capability. The current density−voltage (*J*−*V*) curves of HODs and EODs measured with direct-current (DC, solid symbols) or pulse (hollow symbols) mode were displayed in **Figure 2-10 (a)**. It could be concluded that hole- and electron-transporting can be well balanced in such device architectures even when the extremely high driving voltages were applied to them.

Therefore, the OLED architecture was accordingly designed as follows: glass substrate/ITO (30 nm)/20 wt% Cs: BSBCz (30 nm)/1 wt% DCNP-pCN: BSBCz (180 nm)/MoO_3 (10 nm)/Al (100 nm) [the OLED architecture was shown in Figure 2-10 (b)]. From Figure 2-10 (c), OLEDs possessed a low current leakage before turning them on. Meanwhile, a turn-on voltage of 2.7 V was obtained. In regards to the EL spectrum, it was noticeable that there was almost no emission leakage from BSBCz, indicating that the BSBCz-to-DCNP-pCN energy transfer or direct carrier trapping on DCNP-pCN molecules was happening. Remarkably, EQEs exceeding 2% could be achieved with neither efficiency rolloff nor degradation when the current density was increased to 300 mA cm^{-2} under DC electrical excitation [Figure 2-10 (d)].

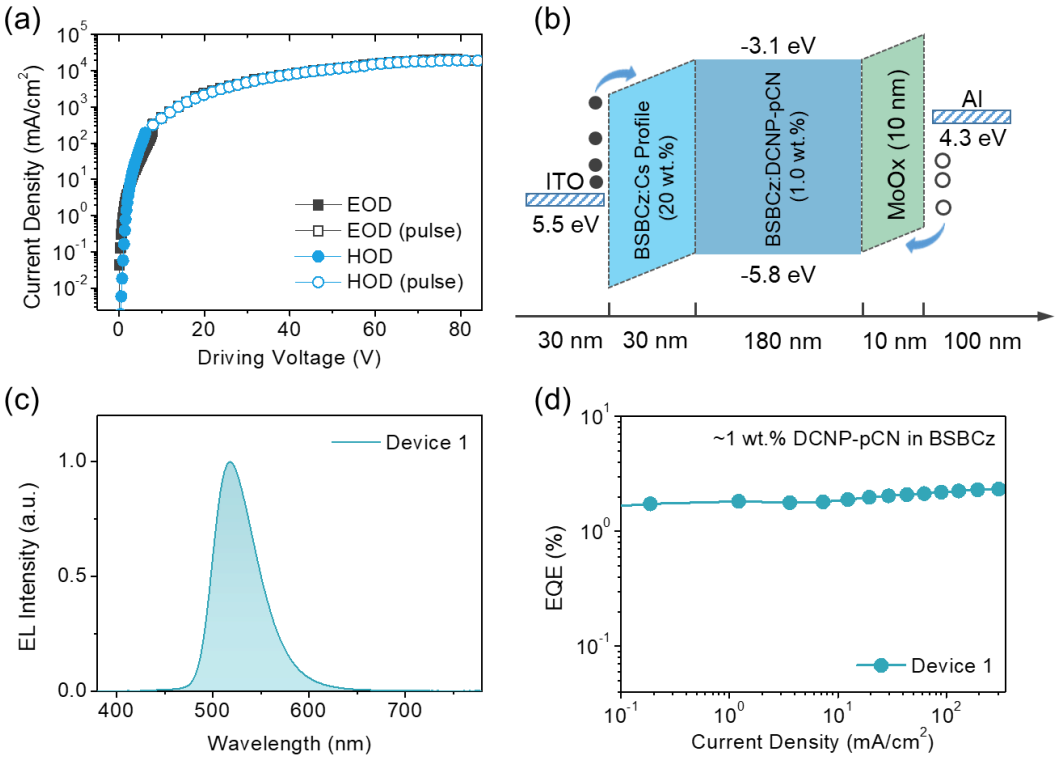

Figure 2-10. (a) *J*−*V* curves measured with DC and pulse operation (400 ns) for EOD and HOD devices. (b) Device architecture and energy-level diagram, (c) EL spectrum, and (d) EQE−*J* curve of OLEDs based on 1 wt% DCNP-pCN: BSBCz blend film.

Further, the EQE values under 400 ns pulsed excitation were then evaluated (**Figure 2-11**), which exhibited almost no efficiency rolloff even under the high current density exceeding 17000 mA cm^{-2}. For the comparison, OLEDs based on a DCNP-pCN neat film were also designed and fabricated by replacing the EML from a 1.0 wt% DCNP-pCN: BSBCz film to a DCNP-pCN neat film. Resultantly, the maximum EQE was only 0.8% with severe efficiency rolloff in **Figure 2-12** and **Table 2-2**. No efficiency rolloff even at high current densities plays an important role in realizing electrical-pumping OSLDs. To unveil why no efficiency rolloff happened in our OLEDs, we conducted the transient EL response properties under the long optical and electrical pulse excitation (1 ms). When the current density injection was subsequently increased from 15 to exceeding 17000 mA cm^{-2}, there was no transient EL intensity decline or degradation in 1wt% DCNP-pCN: BSBCz based OLEDs under 1 ms square pulse operation (the inset of Figure 2-11). The stable PL/EL intensity within the

variation of excitation power or current density in several orders of magnitude implied the complete suppression of STA, which mainly originate from the singlet quenching process undertaken by the accumulated long-lived triplets. In this case, the detrimental long-lived triplets generated at DCNP-pCN were quickly trapped by the lower T_1 level of BSBCz, followed by the rapid nonradiative relaxation to the ground state to prevent the triplet accumulation.

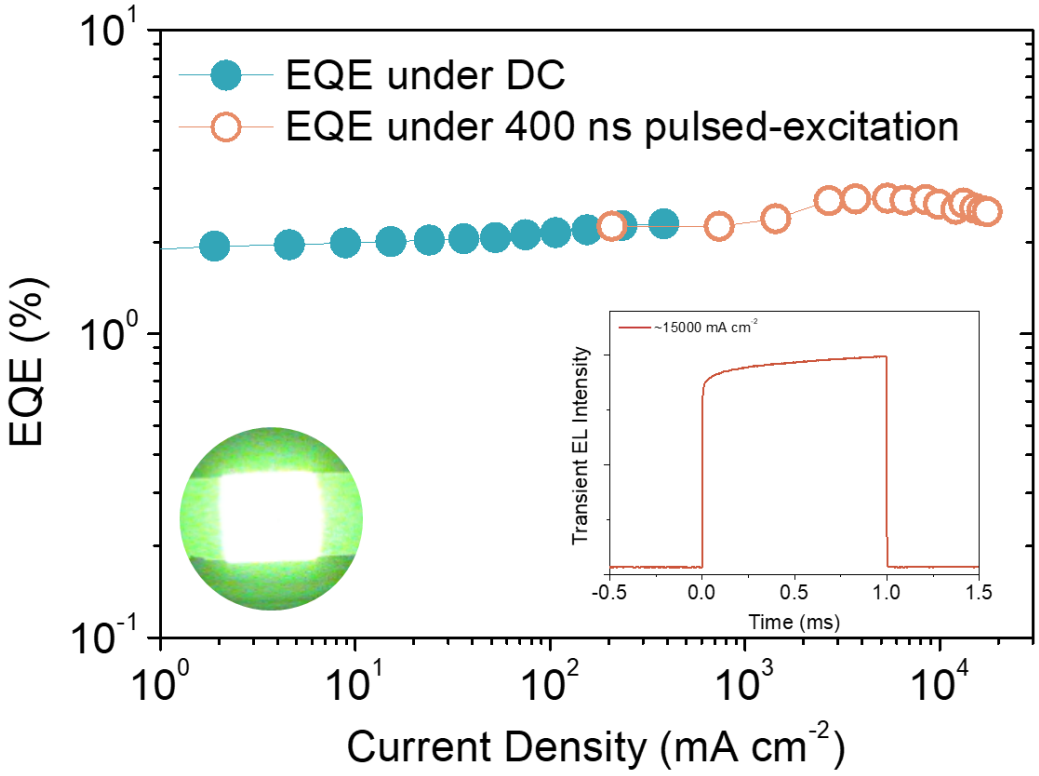

Figure 2-11. EQE of OLED based on 1 wt% DCNP-pCN: BSBCz blend film under pulsed (400 ns) excitation. The inset is the transient EL curve of the corresponding OLED under 1 ms pulsed excitation.

As expected in Figure 2-12, OLEDs based on a DCNP-pCN neat film without any triplet scavenger exhibited a serious EL intensity decease under the 1 ms pulse operation, implying STA happened in the device, which was consistent with the observation of its efficiency rolloff. Therefore, this triplet manipulation strategy as well as the lasing dye molecular design are beneficial to realizing the electrical-pumping OSLDs.

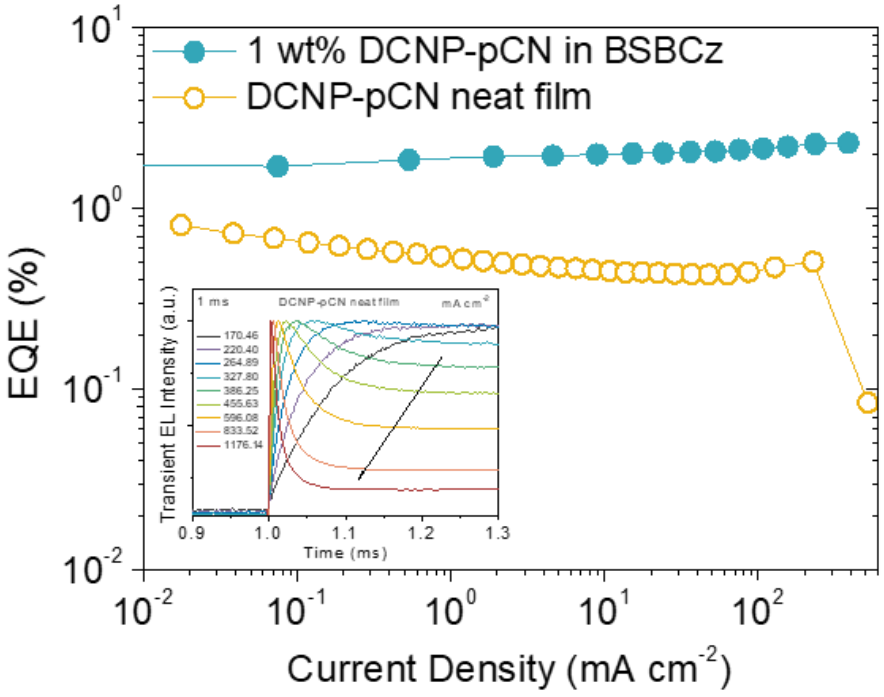

Figure 2-12. EQEs of OLEDs based on a DCNP-pCN neat film. The inset is the transient EL curve of the corresponding OLED under 1 ms-pulsed excitation.

Table 2-2. Performance of OLEDs based on DCNP-pCN.

Material	$V_{turn\text{-}on}$[a] (V)	EQE (%) at mA cm^{-2}			Luminance[b] (cd m^2)	λ_{EL} (nm)
		@ 1	@ 10	@ 300		
DCNP-pCN in BSBCz	2.7	1.83	1.89	2.33	35911	517.8
DCNP-pCN	3.5	0.53	0.45	0.1	4062	524.0

[a] turn-on voltage at 1 cd m^{-2}; [b] maximum luminance (cd m^{-2})

2.3 Conclusion

In summary, organic lasers and EL performance could be achieved by precisely tuning the substitutes and interplays of organic lasing gain molecules. In detail, while a cyanophenyl-moiety possessing a relatively weak electron-withdrawing capability was conjugated to a DCNP-core, the introduction of weak D/A interplays inducing a CT state effectively maintained the small ΔE_{ST} (0.45 eV) of DCNP-pCN but did not affect the priority of the LE state, thereby retaining a large *f*. Therefore, the remarkable laser performance from 2nd-order and mixed-order DFB devices could be obtained with high stability and a low lasing threshold around 2.0 μJ cm^{-2}. Moreover, an EQE value exceeding 2.0%, with no efficiency rolloff, was available in a thick homogeneous-structure OLED, and there was no exciton quenching happening under the high pulsed current injection (>17000 mA cm^{-2}), which arises from a promising laser dye design strategy and is useful for further improving OSLDs performance.

2.4 Experimental section

Materials

All reagents were used as purchased from commercial sources and were used without further purification. Column chromatographic separations were carried out using silica gel (200–300 nm). Nuclear magnetic resonance (NMR) spectra were obtained in $CDCl_3$ with a Bruker Biospin Avance-III 500 NMR spectrometer at ambient temperature. Chemical shifts (δ) were given in parts per million (ppm) relative to tetramethylsilane (TMS) as an internal reference. Elemental analyses (C, H, and N) were carried out with a Yanaco MT-5 elemental analyzer. Mass spectra were measured in positive-ion atmospheric-pressure chemical ionization (APCI) mode on a Waters 3100 mass detector. MALDI-TOF-MS spectra were measured using Shimadzu Biotech AXIMA (HP Z220 CMT workstation). Thermal gravimetry-differential thermal analysis (TG-DTA) was performed by Bruker TG-DTA 2400SA with a heating rate of 10 ^{o}C min^{-1} under nitrogen atmosphere. Differential scanning calorimetry (DSC)

analysis was performed by Netzsch DSC204 Phoenix calorimeter at a scanning rate of 5 ℃ min^{-1} under N_2 atmosphere.

Synthesis route

Synthesis of 4-bromo-2,6-dicyano-1,1-diphenyl-$\lambda^5\sigma^4$-phosphinine (BrDCNP)

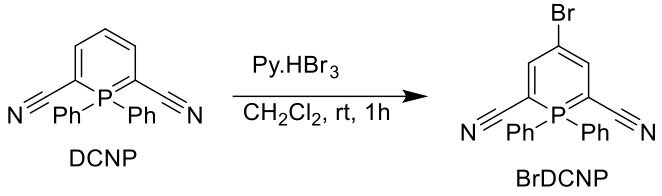

Figure 1-13. Synthesis route of BrDCNP.

Phosphinine DCNP (1.47 g, 4.9 mmol, synthesis routine was referred by Ref.38)[38] was dissolved in CH_2Cl_2 (17.5 mL), then, pyridinium bromideperbromide (1.57 g, 4.9 mmol, 1.0 equiv) was added to the prepared solution at room temperature. After stirring at RT for 1 h, water was added. Afterwards, the mixture was extracted for three times with chloroform ($CHCl_3$). The combined organic layer was washed with 1 M HCl aq. and brine. The organic layer was dried by Na_2SO_4, and concentrated under vacuum. The crude product was roughly purified by passing through a short column of silica gel (eluent: $CHCl_3$) and then recrystallized from $CHCl_3$/Et_2O to give BrDCNP as a red-orange solid (1.60 g, 85%).

Synthesis of 4-(4-cyanophenyl)-1,1-diphenyl-1λ^5-phosphinine-2,6-dicarbonitrile (DCNP-pCN)

Phosphinine BrDCNP (0.377 g, 1 mmol, 1.0 equiv), (4-cyanophenyl)boronic acid (0.220 g, 1.5 mmol, 1.5 equiv), $PdCl_2(PPh_3)_2$ (28.0 mg, 0.04 mmol, 4 mol%) and Na_2CO_3(1.05 g, 10 mmol, 10 equiv.) were dissolved in a toluene: EtOH: water (10: 2.5: 10 ml) mixture, and the mixture was refluxed (85 ℃) for 24 h. After the mixture was cooled to room temperature, water was added and the mixture was extracted for four times with $CHCl_3$. The combined organic layer was washed by brine and dried over Na_2SO_4, and the solvent was removed in vacuum. The residue was purified by a column chromatography on silica gel (eluent: AcOEt/*n*-Hexane = 1/3) to give yellow solid (0.24 g, 60 %). ^{1}H NMR (500 MHz, DMSO-D6) δ 7.69−7.76 (m, 8 H), 7.80−7.89 (m, 6 H),

8.22 (s, 1H), 8.28 (s, 1H); ^{13}C NMR (125 MHz, DMSO-D6) δ 59.91, 60.77, 107.98, 113.77, 113.85, 118.57, 118.67, 119.66, 124.19, 124.92, 125.41, 130.63, 130.74, 132.80, 132.89, 132.97, 134.90, 144.00, 146.85; ^{31}P NMR (202 MHz, DMSO-D6) δ 8.82; MS(ASAP): *m/z* calcd. for $C_{26}H_{16}N_3P$: 401.1082 ([M]+1); found. 402.20. MS(FAB+): *m/z* calcd. for $C_{26}H_{16}N_3P$: 401.1082; found. 401.1080.

1,1-Diphenyl-4-(9-phenyl-9H-carbazol-3-yl)-1λ^5-phosphinine-2,6-dicarbonitrile (DCNP-PhCz)

A procedure similar to that used for DCNP-pCN was followed using (9-phenyl-9H-carbazol-3-yl)boronic acid (0.430 g, 1.5 mmol, 1.5 equiv.).

Red solid (0.40 g, 74 %). ^{1}H NMR (500 MHz, DMSO-D6) δ 7.27−7.30 (t, J=7.5 Hz, 1 H), 7.32−7.34 (d, J=10.0 Hz, 1 H), 7.37−7.39 (d, J=10.0 Hz, 1 H), 7.41−7.44 (t, J=7.5 Hz, 1 H), 7.52−7.57 (m, 2H), 7.62−7.63 (t, J=5.0 Hz, 2 H), 7.71−7.72 (d, J=5.0 Hz, 2 H), 7.73−7.88 (m, 10 H), 8.14 (s, 1H), 8.19 (s, 1H), 8.27−8.29 (d, J=10.0 Hz, 1 H), 8.40 (s, 1 H); ^{13}C NMR (125 MHz, DMSO-D6) δ 58.05, 58.91, 110.11, 116.91, 116.99, 117.24, 119.20, 119.30, 120.49, 121.22, 123.43, 123.74, 124.17, 125.01, 125.75, 126.79, 127.02, 128.06, 130.57, 130.68, 132.20, 132.67, 132.76, 134.66, 137.40, 139.13, 140.97, 146.17; ^{31}P NMR (202 MHz, DMSO-D6) δ 9.51; MS(ASAP): m/z calcd. for C37H24N3P: 541.1708 ([M]+1); found. 542.24. MS(FAB+): m/z calcd. for C37H24N3P: 541.1708; found. 541.1725.

4-(4-(Diphenylamino)phenyl)-1,1-diphenyl-1λ^5-phosphinine-2,6-dicarbonitrile (DCNP-TPA)

A procedure similar to that used for DCNP-pCN was followed using (4-(diphenylamino)phenyl)boronic acid (0.433 g, 1.5 mmol, 1.5 equiv.).

Red solid (0.37 g, 68%). ^{1}H NMR (500 MHz, DMSO-D6) δ 6.94−6.95 (d, J=5.0 Hz, 2 H), 6.98−6.70 (d, J=10.0 Hz, 4 H), 7.01−7.04 (t, J=7.5 Hz, 2 H), 7.27−7.30 (t, J=7.5 Hz, 4 H), 7.40−7.42 (d, J=5.0 Hz, 2 H), 7.67−7.87 (m, 10 H), 7.99 (s, 1H), 8.05 (s, 1H); ^{13}C NMR (125 MHz, DMSO-D6) δ 58.29, 59.15, 115.61, 115.69, 118.99, 119.08, 123.26, 124.02, 124.55, 124.77, 125.50, 126.20, 129.97, 130.55, 130.66, 132.67, 132.76,

134.29, 134.69, 145.51, 145.76, 147.70; ^{31}P NMR (202 MHz, DMSO-D6) δ 9.43; MS(ASAP): *m/z* calcd. for $C_{37}H_{26}N_3P$: 543.1864 ([M]+1); found. 544.40. MS(FAB+): *m/z* calcd. for $C_{37}H_{26}N_3P$: 543.1864; found. 543.1867.

Film sample preparation

Quartz substrates were subsequently ultrasonically washed by alkali detergent, pure water, acetone and isopropyl alcohol (IPA) each for 15 minutes. Then, the cleaned substrates were transferred into a deposition chamber. A 1.0 wt% DCNP-pCN and BSBCz were co-deposited onto the prepared quartz substrates with a thickness of 200 nm under high vacuum pressure (2.0×10^{-5} Torr) with a total deposition rate of 2.5 Å s^{-1}.

Photophysical properties

The steady-state ultraviolet-visible absorption spectra were measured by a double-beam absorption spectrometer (Lambda 950, Perkin Elmer). The steady-state PL and phosphorescence spectra were collected by a spectro-fluorimeter (JASCO FP 8600) at room temperature and 77 K (liquid nitrogen temperature), respectively. The PLQY values were measured by a Quantaurus-QY plus spectrometer (Hamamatsu Photonics). Transient PL decay curves were detected by a time-resolved spectroscopy setup, which is composed of a third harmonic wave generation, a Nd:YAG/YVO lasing source (EKSPLA PL-2250) (with an excitation wavelength of 355 nm and a pulse duration of 30 ps), and a streak camera (C10910-01, Hamamatsu Photonics).

Organic solid-state film fabrication and ASE measurement

DCNP-derivatives and BSBCz were thermally co-deposited onto the substrates in the vacuum chamber, followed by storing in the glove box filled with nitrogen gas. For ASE measurement, the prepared solid-state film was optically-excited at the edge region by a randomly polarized nitrogen gas laser source (KEN2020, USHO Optical Systems Co., Ltd.) with a pulse width of 800 ps at an excitation wavelength of 337 nm. The output lasing beam was concentrated to a stripe shape for waveguide emission. The ASE emission was detected from the edge of the quartz substrate by a spectrometer (Hamamatsu Photonics PMA-12). ASE measurements are conducted under the nitrogen atmosphere to prevent the detrimental effects caused by oxygen and moisture.

DFB structure fabrication

A silicon dioxide layer with a thickness of 1000 nm was sputtered onto glass substrates to avoid the exciton quenching by the glass. Then, the substrates were subsequently washed as the aforementioned steps. After the UV-ozone treatment, hexamethyldisilazane was spin-coated on the silicon dioxide surface at 4000 rpm for 15 s and then annealed at 120 ℃ for 120 s. Afterward, to form a resist layer, ZEP520A-7 solution (ZEON Co.) was dropped onto the surface, followed by spin-coating at 4000 rpm for 30 s and annealing at 180 ℃ for 4 min. Next, the electron-beam lithography (JEOL, JBX-5500SC) was used to obtain the grating patterns on the resist layer. For the development of the resist layers, the grating patterns were developed in ZED-N50 (ZEON Co.) solution at room temperature. During the process of etching, the resist layer was employed as the protecting layer while the substrates have undertaken the plasma-etching with CHF_3 using an EIS-200ERT etching system (Elionix). For completely removing the resist layer from the substrates, they were plasma-etched with O_2 using an FA-1EA etching system (SAMCO).

Fabrication and characterization of optical-pumping organic lasing

After finishing the 2^{nd}-order and mixed-order DFB fabrication, the corresponding DFB substrates were transferred into the vacuum chamber (vacuum pressure was 2.0×10^{-5} Torr) and the thermal co-deposition of DCNP-pCN and BSBCz at 1.0 wt% was conducted, with its total thickness being controlled at 200 nm. After the thermal deposition, the substrates were transferred to the glove box filled with nitrogen gas to avoid the potential degradation caused by oxygen and moisture in air. Three droplets of CYTOP (purchased from Asahi Glass Co. Ltd.) were spin-coated on the surface of the organic films. Eventually, the samples were encapsulated by a sapphire lid, which were then dried under vacuum overnight. The fabricated samples were optically excited by a nitrogen-gas lasing source (NL100, Stanford Research System, excitation lasing wavelength is 337 nm with 3 ns pulse), whose output beam was concentrated to a small-size light spot through a lens and a slit. The lasing intensity and spectral shape were detected by a multichannel spectrometer (PMA-50, Hamamatsu Photonics) with an optical fiber. The excitation power was manipulated by adjusting the neutral density

filters with different optical densities. Near-field and far-field patterns of 2nd-order and mixed-order DFB lasing were measured by a lasing beam profiler (C9164-01, Hamamatsu Photonics) and (C9664-01G02, Hamamatsu Photonics), respectively.

OLED device fabrication and characterization

Organic and metallic layers are subsequently thermally evaporated onto the pre-patterned ITO substrates with shadow masks of different patterns. The completed OLEDs were transferred to the glove box filled with nitrogen, and then I conducted encapsulation using a glass cap and UV curing epoxy resin. The *J*−*V*, luminance (*L*) and EQEs were measured under the DC mode by a calibrated luminance meter (CS-2000, Konica Minolta, Japan), and integrated with a constant source meter (Keithley 2400, Keithley Instruments Inc.).

DFT calculations

The computational studies were conducted using the computer facilities at the Research Institute for Information Technology, Kyushu University. The ground-state (S_0) geometry of emitters was optimized at the B3LYP/6-311+G(d) level using Gaussian 09, and the time-dependent DFT (TD-DFT) calculations were conducted at the B3LYP/6-311+G(d) level for the excited state calculation using the S_0 geometry.

Pulsed EL measurement

I set up the pulsed transient EL emission system to assist the measurement of EQE under pulsed excitation. The instrument was integrated by a digital storage oscilloscope (DSO5045A, Agilent Technologies), a high-speed bipolar amplifier (HAS 4101, NF Corporation), a pulse generator (30 MHz multifunction generator WF1974, NF Corporation), a photomultiplier tube (PMT, C9525-02, Hamamatsu Photonics) detector, and one resistance. The pulse generator supplied the pulse signal to the bipolar amplifier, and the bipolar amplifier supplied very high voltage. One resistance (1.1 Ω) and the target OLED was connected in series. The PMT was used to collect the photons from OLEDs and then transfer the photon signal to the electrical signal. The oscilloscope could provide three channels to deal with three electrical signals from the amplifier, resistance and PMT. The detected applied voltage at the resistance (1.1 Ω), thus, according to the Ohm's rule

$$I = \frac{V}{R}; J = \frac{I}{S};\ (2\text{-}1)$$

where I is the current of the electric circuit, R is the resistance, V is the applied voltage, S is the light emission area of OLED (0.04 cm^{-2}), J is the current density of OLED. So, the current density (J) of OLED can be calculated.

The next step was to evaluate the EQEs of the OLED under 400 ns pulse excitation. EQE was related to the spectral shape and current efficiency (CE). To ensure the EL spectra shape under the pulse excitation, I used a photonic multichannel analyzer (PMA-50) to measure the emission spectra at different current densities. When increasing the current density, the EL intensity was also increased, which was consistent with the conclusion obtained from PMT. I compared the EL spectral shape between pulsed excited and DC excited devices at 53 mA cm^{-2}, it was evident to see the same spectral shapes under the two different conditions. The next part was to determine EQEs, the unit of luminance (L) is cd m^{-2}, of current density I is A m^{-2} (or mA cm^{-2}), of current efficiency (CE) is cd A^{-1}. According to following equations:

$$\text{EQE} \propto \text{CE};\ \text{CE}(\text{cd}\ A^{-1}) = \frac{L(cd\ m^{-2})}{I(A\ m^{-2})},\ (2\text{-}2)$$

$$\text{Thus, EQE} \propto \frac{L(cd\ m^{-2})}{I(A\ m^{-2})};\ \text{and}\ \frac{EQE_m}{EQE_n} = \frac{L_m}{I_m} \times \frac{I_n}{L_n},\ (2\text{-}3)$$

Here, at the current of 208 mA cm^{-2}, EQE_{208} was measured of 2.26%, according to Equation (2-3), I could also calculate the other EQE values under different current densities. Up to 17000 mA cm^{-2}, all the EQEs could exceed 2%, and there was almost no efficiency rolloff. So, it confirmed that there was no STA for this system under the very high current density (>17000 mA cm^{-2}) with the pulsed electrical excitation.

References

[1] H. Nakanotani, S. Akiyama, D. Ohnishi, M. Moriwake, M. Yahiro, T. Yoshihara, S. Tobita, C. Adachi, *Adv. Funct. Mater.* **2007**, *17*, 2328.

[2] T. Nakagawa, S.-Y. Ku, K.-T. Wong, C. Adachi, *Chem. Commun.* **2012**, *48*, 9580.

[3] P. R. Hammond, *Opt. Commun.* **1979**, *29*, 331.

[4] S. L. Bondarev, V. N. Knyukshto, V. I. Stepuro, A. P. Stupak, A. A. Turban, *J. Appl. Spectrosc.* **2004**, *71*, 194.

[5] M. Meyer, J. C. Mialocq, *Opt. Commun.* **1987**, *64*, 264.

[6] X. Liu, M. Sang, H. Lin, C. Liu, J. Zhang, J. Yi, K. Gao, W.-Y. Lai, W. Huang, *Chem. Eur. J.* **2020**, *26*, 3103.

[7] E. Collet, M.-H. Lemée-Cailleau, M. Buron-Le Cointe, H. Cailleau, M. Wulff, T. Luty, S.-Y. Koshihara, M. Meyer, L. Toupet, P. Rabiller, S. Techert, *Science* **2003**, *300*, 612.

[8] A. J. Kuehne, M. C. Gather, *Chem. Rev.* **2016**, *116*, 12823.

[9] D.-H. Kim, A. D'Aléo, X.-K. Chen, A. D. S. Sandanayaka, D. Yao, L. Zhao, T. Komino, E. Zaborova, G. Canard, Y. Tsuchiya, E. Choi, J. W. Wu, F. Fages, J.-L. Brédas, J.-C. Ribierre, C. Adachi, *Nat. Photon.* **2018**, *12*, 98.

[10] H. Ye, D. H. Kim, X. Chen, A. S. D. Sandanayaka, J. U. Kim, E. Zaborova, G. Canard, Y. Tsuchiya, E. Y. Choi, J. W. Wu, F. Fages, J.-L. Bredas, A. D'Aléo, J.-C. Ribierre, C. Adachi, *Chem. Mater.* **2018**, *30*, 6702.

[11] A. Abbotto, L. Beverina, R. Bozio, S. Bradamante, C. Ferrante, G. A. Pagani, R. Signorini, *Adv. Mater.* **2000**, *12*, 1963.

[12] F. Maowen, W. Jieyun, G. Deng, W. Zhang, C. Kaixin, Y. Gong, *17th International Conference on Optical Communications and Networks* **2019**, *11048*,

[13] A. K. Sheridan, A. R. Buckley, A. M. Fox, A. Bacher, D. D. C. Bradley, I. D. W. Samuel, *J. Appl. Phys.* **2002**, *92*, 6367.

[14] B. S. B. Karunathilaka, U. Balijapalli, C. A. M. Senevirathne, S. Yoshida, Y.

Esaki, K. Goushi, T. Matsushima, A. S. D. Sandanayaka, C. Adachi, *Nat. Commun.* **2020**, *11*, 4926.

[15] U. Balijapalli, X. Tang, D. Okada, Y.-T. Lee, B. S. B. Karunathilaka, M. Auffray, G. Tumen-Ulzii, Y. Tsuchiya, A. S. D. Sandanayaka, T. Matsushima, H. Nakanotani, C. Adachi, *Adv. Opt. Mater* **2021**, *n/a*, 2101122.

[16] O. Mhibik, S. Forget, D. Ott, G. Venus, I. Divliansky, L. Glebov, S. Chénais, *Light Sci. Appl.* **2016**, *5*, e16026.

[17] M. Zavelani-Rossi, G. Lanzani, M. Anni, G. Gigli, R. Cingolani, G. Barbarella, L. Favaretto, *Synth. Met.* **2003**, *139*, 901.

[18] N. F. Cover, S. Lai-Yuen, A. K. Parsons, A. Kumar, *Int J Nanomedicine* **2012**, *7*, 2411.

[19] H. Aziz, Z. D. Popovic, *Chem. Mater.* **2004**, *16*, 4522.

[20] W. Z. Yuan, P. Lu, S. Chen, J. W. Y. Lam, Z. Wang, Y. Liu, H. S. Kwok, Y. Ma, B. Z. Tang, *Adv. Mater.* **2010**, *22*, 2159.

[21] H. He, H. Li, Y. Cui, G. Qian, *Adv. Opt. Mater.* **2019**, *7*, 1900077.

[22] W. Liu, H. Yu, R. Hu, T. Xu, Y. Lun, J. Gan, S. Xu, Z. Yang, B. Z. Tang, *Small* **2020**, *16*, 1907074.

[23] B.-P. Jiang, Y.-X. Yu, X.-L. Guo, Z.-Y. Ding, B. Zhou, H. Liang, X.-C. Shen, *Carbon* **2018**, *128*, 12.

[24] K. B. Clark, J. A. Howard, A. R. Oyler, *JACS* **1997**, *119*, 9560.

[25] J. P. Webb, W. C. McColgin, O. G. Peterson, D. L. Stockman, J. H. Eberly, *J. Chem. Phys.* **1970**, *53*, 4227.

[26] M. Reufer, J. M. Lupton, U. Scherf, *Appl. Phys. Lett.* **2006**, *89*, 141111.

[27] V. T. N. Mai, V. Ahmad, M. Mamada, T. Fukunaga, A. Shukla, J. Sobus, G. Krishnan, E. G. Moore, G. G. Andersson, C. Adachi, E. B. Namdas, S.-C. Lo, *Nat. Commun.* **2020**, *11*, 5623.

[28] C. Gärtner, C. Karnutsch, U. Lemmer, C. Pflumm, *J. Appl. Phys.* **2007**, *101*, 023107.

[29] L. Zhao, M. Inoue, K. Yoshida, A. S. D. Sandanayaka, J. Kim, J. Ribierre, C. Adachi, *IEEE Journal of Selected Topics in Quantum Electronics* **2016**, *22*, 26.

[30] T. Aimono, Y. Kawamura, K. Goushi, H. Yamamoto, H. Sasabe, C. Adachi, *Appl. Phys. Lett.* **2005**, *86*, 071110.

[31] T. Matsushima, S. Yoshida, K. Inada, Y. Esaki, T. Fukunaga, H. Mieno, N. Nakamura, F. Bencheikh, M. R. Leyden, R. Komatsu, C. Qin, A. S. D. Sandanayaka, C. Adachi, *Adv. Funct. Mater.* **2019**, *29*, 1807148.

[32] Q. Ou, Q. Peng, Z. Shuai, *Nat. Commun.* **2020**, *11*, 4485.

[33] A. S. D. Sandanayaka, T. Matsushima, F. Bencheikh, S. Terakawa, W. J. Potscavage, C. Qin, T. Fujihara, K. Goushi, J.-C. Ribierre, C. Adachi, *Appl. Phys. Express* **2019**, *12*, 061010.

[34] S. D. Sandanayaka Atula, T. Matsushima, F. Bencheikh, K. Yoshida, M. Inoue, T. Fujihara, K. Goushi, J.-C. Ribierre, C. Adachi, *Sci. Adv. 3*, e1602570.

[35] A. S. D. Sandanayaka, K. Yoshida, M. Inoue, C. Qin, K. Goushi, J.-C. Ribierre, T. Matsushima, C. Adachi, *Adv. Opt. Mater.* **2016**, *4*, 834.

[36] B. S. B. Karunathilaka, U. Balijapalli, C. A. M. Senevirathne, Y. Esaki, K. Goushi, T. Matsushima, A. S. D. Sandanayaka, C. Adachi, *Adv. Funct. Mater.* **2020**, *30*, 2001078.

[37] H. Nakanotani, C. Adachi, S. Watanabe, R. Katoh, *Appl. Phys. Lett.* **2007**, *90*, 231109.

[38] N. Hashimoto, R. Umano, Y. Ochi, K. Shimahara, J. Nakamura, S. Mori, H. Ohta, Y. Watanabe, M. Hayashi, *J. Am. Chem. Soc.* **2018**, *140*, 2046.

Chapter 3. Functional spacers inserted in strong donor-acceptor molecules for color-tunable low-threshold lasers ranging from yellow to near-infrared (NIR) regions

3.1 Introduction

Organic dyes have been widely employed as light emitters for OLEDs and promising gain mediums for OSLs for the past few decades. This owed to their unique and outstanding merits, for instance, feasible chemical tunability for molecular designs, and thin-film light weight and flexibilities.[1-4] In particular, in regards to the emerging organic lasing sources, the potential applications in the fields of optical communication, high-sensitivity sensors, high-resolution spectroscopy, medical surgery and bio-integration, are benefited from its exclusive characteristics such as high emission intensity, mono-directionality and large coherence length.[5] Up to now, careful chemical engineering of the donor-acceptor interactions and energy gaps has allowed the preparation of small molecules, oligomers and polymers exhibiting stimulated emission from deep blue to NIR regions.[6-11] Nevertheless, the introduction of substituents with either distinct electron-donating or electron-accepting capabilities for reducing the energy gaps, would reorganize the wavefunction distributions, which commonly tended to be separated from each other. Therefore, most of the candidates had a high-lying energy level resulting in blue-emission with suppressed distinct D-A interactions. Those dyes showed very low ASE and therefore low lasing thresholds (below 1 μJ cm^{-2}),[12-15] similar to well-studied small molecule BSBCz.[7, 16-19] BSBCz has realized true CW optical lasing,[19-21] and the indication of electrical-pumping OSLDs was described.[22] By comparison, either for ASE or lasing thresholds, the progress of gain molecules spanning from yellow to NIR with smaller energy gaps largely still lagged behind.[23]

Recently, π-conjugated oligomers, incorporating a diverse D or A moiety were widely exploited to accelerate the development of yellow-to-NIR laser performance.[4, 24, 25] However, the promising ASE or lasing thresholds were rarely obtained because of the inducing ICT state, as well as the energy-gap law effect, which is an intrinsic limit inducing a decreased fluorescence radiative process because of faster non-radiative processes.[26-28] Moreover, as the large k_r is one of the important parameters to realize lower-threshold ASE and laser actions, the precise manipulation of D/A motifs

not only feasibly tuned the color emission,[29-31] but also determined the HOMO and LUMO energies and their overlap. Such the HOMO/LUMO overlap in contrast with CT states yielded HLCT transition, which induced therefore a relatively large *f*.[32-35]

Herein, I designed the linear D-A type molecules where the skeleton could be described as D-spacer-A-spacer-D for promising laser dyes. In more detail, the donor moiety was chosen to be triphenylamine (TPA), while the fluorene-based spacers connected the D units to the A core. Benzothiadiazole (BTD) and benzo[1,2-c:4,5c']bis[1,2,5]thiadiazole (BBTD) were selected as acceptors for yellow [(TPA-F)$_2$BTD] and NIR [(TPA-F)$_2$BBTD] laser dyes, respectively. It was to be highlighted that long alkyl chains were appended on the fluorene spacer in order to provide a high solubility to realize solution-processed devices, as well as to suppress intermolecular aggregation. The acceptor BBTD exhibited a stronger electron-accepting capability than BTD does, which was due to the extension of the heterocyclic core. Thus, the intensive D/A interplay further led to a much smaller energy gap, thereby resulting in the large red-shift from yellow to NIR emission. Benefitting from the reasonable HOMO/LUMO wavefunction distribution in the molecular skeleton, the noticeable wavefunction overlap guaranteed the LE feature with a large *f* of around 0.5. Such large absorption was accompanied by the fluorescence decay time around 4 ns and high PLQYs of 91% for (TPA-F)$_2$BTD and 33.8% for (TPA-F)$_2$BBTD. Thus, the optimal laser thresholds for yellow and NIR ones were around 1 μJ cm^{-2}, respectively, which were among the lowest ones in the corresponding spectral region to the best of our knowledge. Here, it could be highlighted that the substitution of the fluorene unit with long alkyl chains allowed solution processing and effectively prevented the ACQ, yielding the high PLQY of 90% in a neat film of (TPA-F)$_2$BTD, with a low laser threshold. Moreover, the solution-processed OLEDs of (TPA-F)$_2$BTD and (TPA-F)$_2$BBTD were fabricated and showed EQEs of 2.7% and 0.56% for yellow and NIR emission, respectively, with only slight efficiency rolloff under the injected current density of hundreds of mA cm^{-2}.

3.2 Results and discussion

3.2.1 Molecular design

The specific molecular structures were presented as $(TPA\text{-}F)_2BTD$ and $(TPA\text{-}F)_2BBTD$ in **Figure 3-1**. It is noted that $(TPA\text{-}F)_2BTD$ and $(TPA\text{-}F)_2BBTD$ were constructed on the same linear molecular structure as a donor-spacer-acceptor-spacer-donor skeleton, where the donor fragment was TPA and the spacer was fluorene unit with alkyl-chains. The difference was the strong acceptor moieties, BTD was used in $(TPA\text{-}F)_2BTD$, while BBTD containing an extending heterocyclic core was incorporated into $(TPA\text{-}F)_2BBTD$. Herein, the change from BTD to BBTD reinforced the electron-accepting strength in the molecule for a deeper LUMO energy level to reduce the energy gap with redshifting emission. Meanwhile, for a better comparison, two molecules based on the similar molecular skeleton without spacer units, $(TPA)_2BTD$ and $(TPA)_2BBTD$ were subsequently designed accordingly.

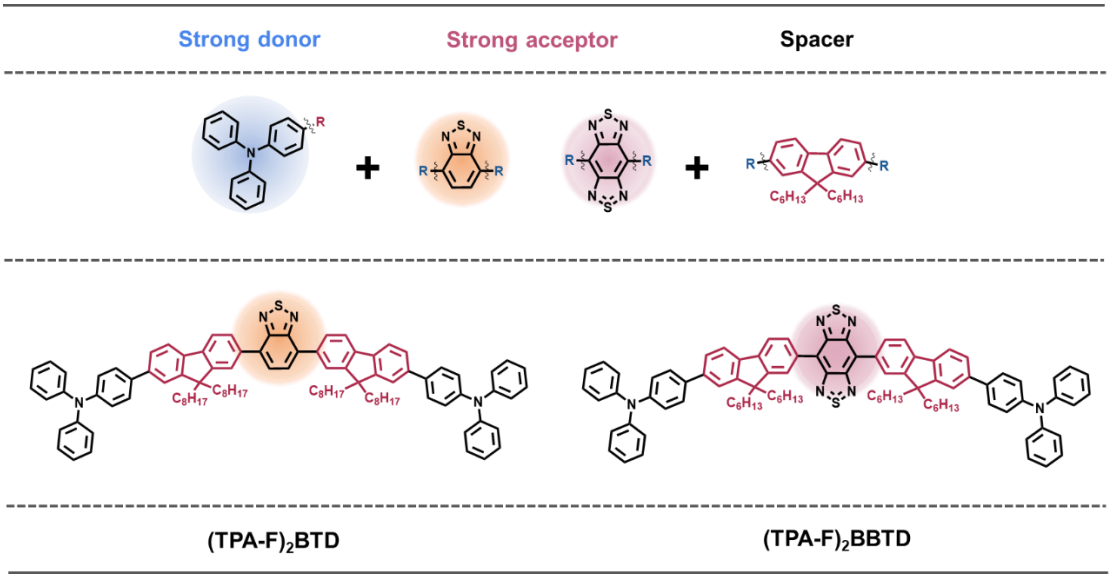

Figure 3-1. Molecular design of strong D-A type dyes $(TPA\text{-}F)_2BTD$ and $(TPA\text{-}F)_2BTD$.

3.2.2 Theoretical calculation

The DFT and time-dependent DFT (TD-DFT) methods were performed to better clarify the geometrical difference and HOMO/LUMO wavefunction distribution of the molecules. As expected [**Figure 3-2 (a)** and **(b)**], the LUMO wavefunctions were mainly concentrated on the BTD and BBTD acceptor moieties and partially extended to fluorene spacers, whereas HOMO wavefunctions were distributed from TPA moieties to fluorene spacers. Herein, the long alkyls chain did not participate in the orbital wavefunction distribution; thus, neither influence of HOMO/LUMO distribution nor derivation of calculated values took place within these two models. In this case, the substantial HOMO/LUMO wavefunction overlap mainly concentrated at the spacer-bridge, which guaranteed a large *f* in the strong D-A type molecules, promoting a high S_1-S_0 transition dipole moment and the large k_r. Thus, the calculated *f* for $(TPA\text{-}F)_2BTD$ and $(TPA\text{-}F)_2BBTD$ are 0.55 and 0.50, respectively, which was a prerequisite for triggering ASE or laser activities. By comparison, D-A type molecules $(TPA)_2BTD$ and $(TPA)_2BBTD$ without spacers exhibited more condensed HOMO/LUMO distribution, because of the shorter strong D/A center distance. Thus, besides the spacer unit, HOMO/LUMO overlap tended to shift to the acceptor-core, the corresponding *f* had a slight decrease for $(TPA)_2BTD$ (0.45) and $(TPA)_2BBTD$ (0.47), respectively. All the calculated data was summarized in **Figure 3-1**.

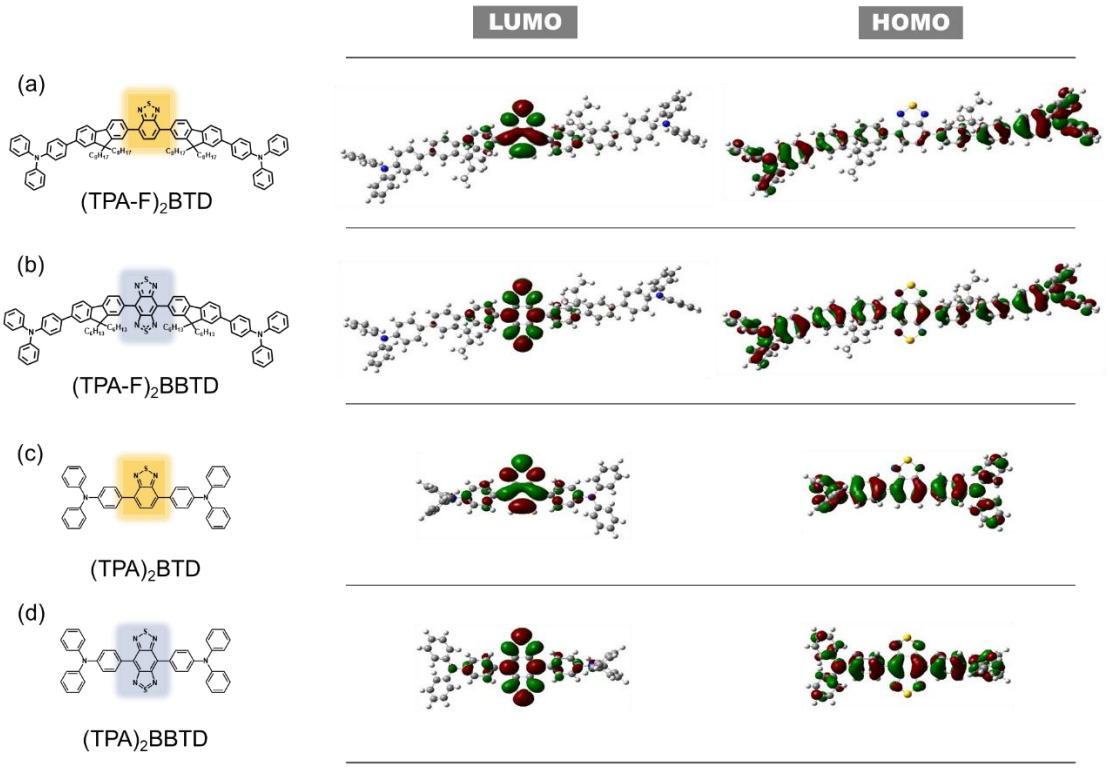

Figure 3-2. Calculated HOMO and LUMO wavefunction distribution of (a) (TPA-F)$_2$BTD and (b) (TPA-F)$_2$BBTD with the spacers and (c) (TPA)$_2$BTD and (d) (TPA)$_2$BBTD without the spacers. The corresponding geometries were optimized at B3LYP/6-31G(d) level.

Table 3-1. Theoretically calculated wavelength peak, HOMO, LUMO, energy gap, and *f* of (TPA-F)$_2$BTD, (TPA-F)$_2$BBTD, (TPA)$_2$BTD, and (TPA)$_2$BBTD.

Material	λ_{PL} (nm)	HOMO (eV)	LUMO (eV)	E_g (eV)	*f*
(TPA-F)$_2$BTD	557.5	−4.85	−2.35	2.22	0.5521
(TPA-F)$_2$BBTD	957.7	−4.82	−3.30	1.29	0.4986
(TPA)$_2$BTD	580.4	−4.80	−2.27	2.14	0.4496
(TPA)$_2$BBTD	987.8	−4.67	−3.17	1.26	0.4660

3.2.3 Solvent effect

Photophysical studies were performed in solution. To that end, solvatochromism was recorded in eight different solvents having different polarities allowing to have information on the excited state dipole moment (ground-state dipole moment was obtained from DFT calculation), while the absorption spectra did not move dramatically, a clear red-shift of the emission of $(TPA\text{-}F)_2BTD$ and $(TPA\text{-}F)_2BBTD$ was observed when increasing the polarity of the solvent in **Figure 3-3**. Such behavior was typical for the CT-state emission, revealing that the ground-state dipole moment is rather low compared to the excited state dipole moment. For $(TPA\text{-}F)_2BTD$ and $(TPA\text{-}F)_2BBTD$, the ground-state dipole moment was 1.69 and 0.86 Debye, respectively, in parallel, the corresponding excited state dipole moment was 13.7 and 8.1 Debye, respectively. These results were consistent with the features of the CT state, implying the HLCT property in this molecular design.

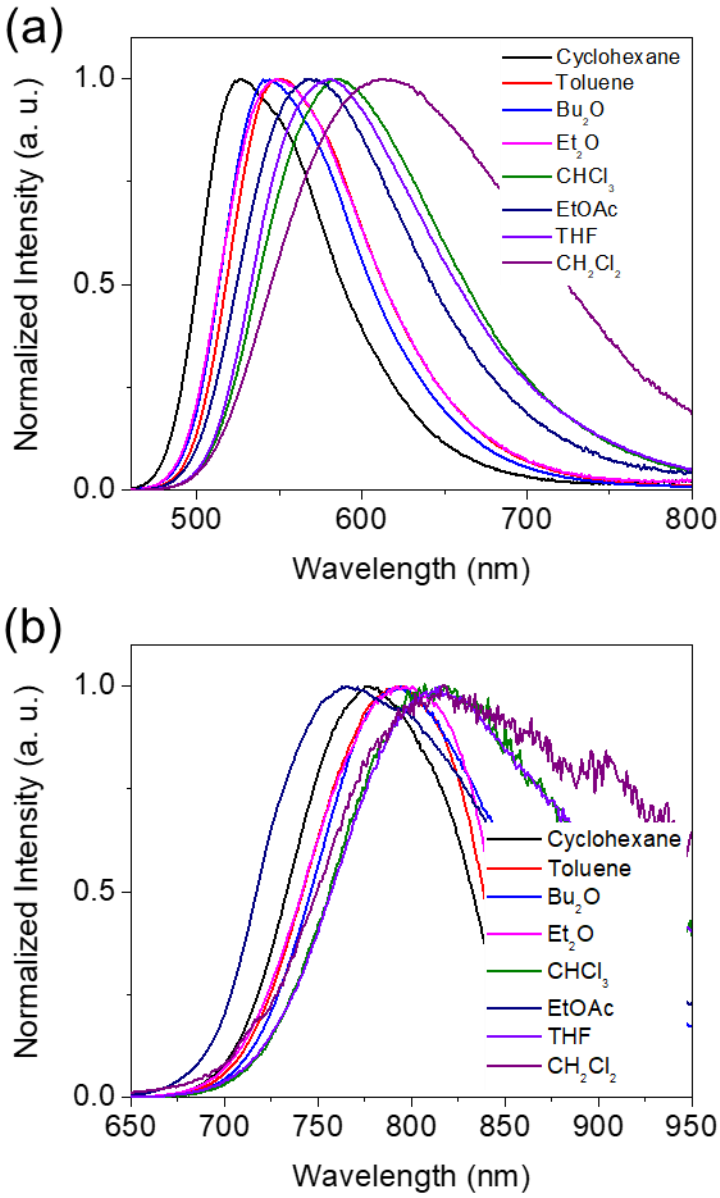

Figure 3-3. (a) $(TPA\text{-}F)_2BTD$ and (b) $(TPA\text{-}F)_2BBTD$ in different solvents with different polarities. The solvents were cyclohexane, toluene, dibutylether (Bu_2O), diethylether (Et_2O), chloroform ($CHCl_3$), ethylacetate (EtOAc), tetrahydrofuran (THF), and dichloromethane (CH_2Cl_2).

3.2.4 Energy level determination

To determine the energy levels of the four molecules, photoelectron spectra were measured by photoelectron yield spectroscopy (AC-3, Riken Keiki). As shown in **Figure 3-4**, in regards to $(TPA)_2BTD$ and $(TPA)_2BBTD$ without fluorene spacers, the

HOMO energy levels were −5.5 and −5.4 eV, respectively. By comparison, after inserting the fluorene spacers between strong D-A skeleton, the HOMO wavefunction distribution extended to the spacers, so the corresponding HOMO energy levels became deeper, which were around −5.8 eV. Thus, the emission of molecules with spacer units ought to exhibit blue-shifting. The corresponding data was summarized in **Table 3-2**.

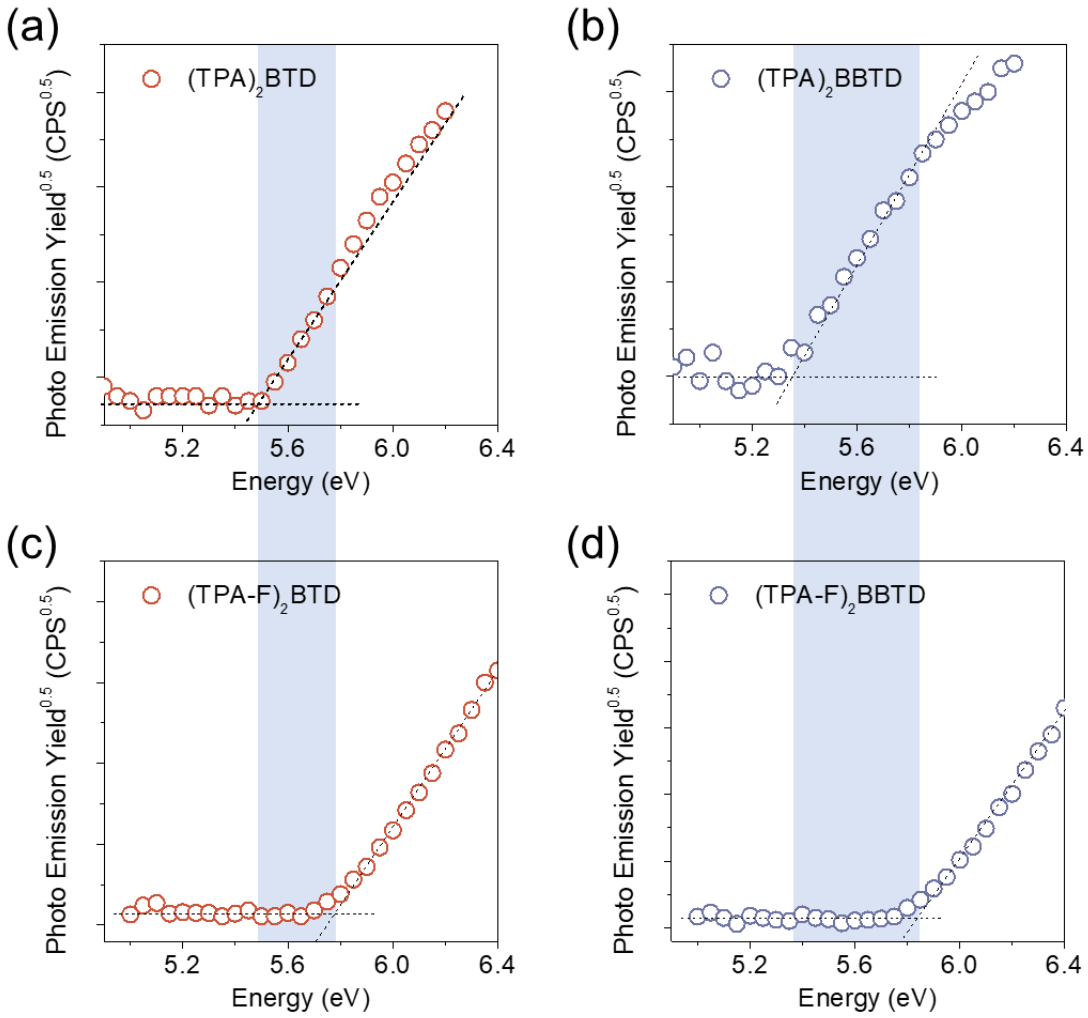

Figure 3-4. Photoelectron yield spectra of (a) $(TPA)_2BTD$, (b) $(TPA)_2BBTD$, (c) $(TPA\text{-}F)_2BTD$, and (d) $(TPA\text{-}F)_2BBTD$.

Table 3-2. Experimental HOMO and LUMO of $(TPA\text{-}F)_2BTD$, $(TPA\text{-}F)_2BBTD$, $(TPA)_2BTD$, and $(TPA)_2BBTD$.

Material	λ_{PL}[a] (nm)	HOMO[b] (eV)	LUMO[c] (eV)	HOMO[d] (eV)	LUMO[d] (eV)

$(TPA\text{-}F)_2BTD$	550	−5.79	−3.38	−5.71	−2.94
$(TPA\text{-}F)_2BBTD$	793	−5.82	−4.27	−5.72	−3.71
$(TPA)_2BTD$	608	−5.50	−3.25	/	/
$(TPA)_2BBTD$	886	−5.40	−3.96	/	/

[a] measured in toluene solution; [b] measured in neat film; [c] measured by subtracting the absorption onset energy from the HOMO energy; [d] measured by CV.

3.2.5 Photophysical properties

Then, the PL of the four molecules was further investigated. As shown in **Figure 3-5**, $(TPA\text{-}F)_2BTD$ and $(TPA)_2BTD$ showed yellow-to-red emission, while $(TPA\text{-}F)_2BBTD$ and $(TPA)_2BBTD$ exhibited NIR emission in toluene, because of the stronger electron-affinity capability with an extending heterocyclic core. As expected, owing to the inserted fluorene spacer with a weaker electron-donating capability, $(TPA\text{-}F)_2BTD$ and $(TPA\text{-}F)_2BBTD$ exhibited shallower HOMO energy levels and blueshifting. In terms of PLQY, $(TPA\text{-}F)_2BTD$ and $(TPA\text{-}F)_2BTD$ with spacers had higher PLQY values of 91.3% and 33.8%, which were higher than their analogs without spacer units (81.2% and 4.1%). Then, the PLQYs were subsequently estimated at various doping ratios in a 4,4'-bis(*N*-carbazolyl)-1,10-biphenyl (CBP) matrix. The solution-processed blend films were fabricated by spin-coating onto the fused silica substrates, and the corresponding film thickness was controlled to be around 150 nm. For the yellow lasing dye $(TPA\text{-}F)_2BTD$, the doping ratios were varied from 3 to 100 wt%. 100 wt% represented a host-free neat film. The consistent maximum absorption peak of the CT transition around 444 nm, as well as no obvious broadening or shifting of this transition within such a large doping region, implied that there might be little concentration-dependent quenching or intermolecular aggregation in those large molecules for $(TPA\text{-}F)_2BTD$. It was worth noting that all PLQY values could almost exceed 90%. In detail, the unity PLQY values (close to 100%) could be achieved at lower doping ratios. Even in the neat film, there was only a slight reduction of the PLQY to 90%, which further

confirmed fluorene-spacer with long alkyl chains in D-spacer-A-spacer-D molecule, not only reinforced the solubility, but also brought a large steric hindrance to effectively reduce the intermolecular interaction and aggregation. By comparison in Figure 3-5 (a), $(TPA)_2BTD$ without spacers in CBP blend films exhibited a smaller PLQY decrease and larger rolloff when increasing the doping concentrations. As shown in Figure 3-5 (b), the PLQYs of NIR molecules $(TPA\text{-}F)_2BBTD$ and $(TPA)_2BBTD$ were well consistent with the findings above.

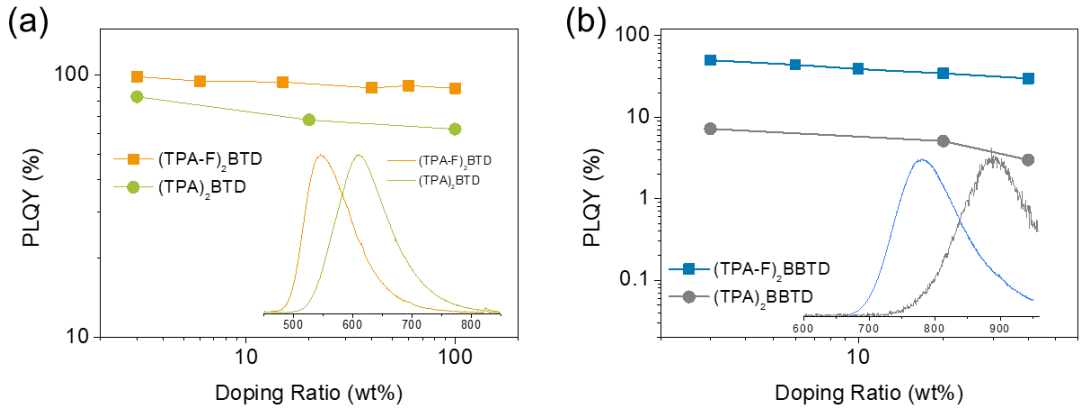

Figure 3-5. PLQYs of (a) $(TPA\text{-}F)_2BTD$ and $(TPA)_2BTD$ and (b) $(TPA\text{-}F)_2BBTD$ and $(TPA)_2BBTD$ doped into CBP at different doping ratios. The insets were PL spectra of $(TPA\text{-}F)_2BTD$, $(TPA)_2BTD$, $(TPA\text{-}F)_2BBTD$, and $(TPA)_2BBTD$ in toluene, respectively.

To gain further insights into those dyes, sub-nanosecond transient PL decay measurements were conducted for $(TPA\text{-}F)_2BTD$ and $(TPA\text{-}F)_2BBTD$-based blend films with 3 wt% doping ratios, and the corresponding fast fluorescence decay lifetimes (τ) were 3.7 and 4.1 ns in respect with doping ratios (**Figure 3-6**). According to the equation: $k_r = \emptyset/\tau$, where k_r denotes the fluorescence radiative rate constant, $\emptyset$ is the PLQY, the samples with 3 wt% doping ratios owned high k_r of 2.7×10^8 and 1.2×10^8 s^{-1}, respectively for blend films, indicating the potential to realize efficient ASE or laser performance. In contrast, $(TPA\text{-}F)_2BTD$ without the spacer units exhibited a slower decay lifetime (6.7 ns), lower PLQY (81%), as well as a smaller k_r, which might result

from the energy-gap law and the shorter D-A distance inducing nonradiative coupling. The corresponding photophysical data was summarized in **Table 3-3**.

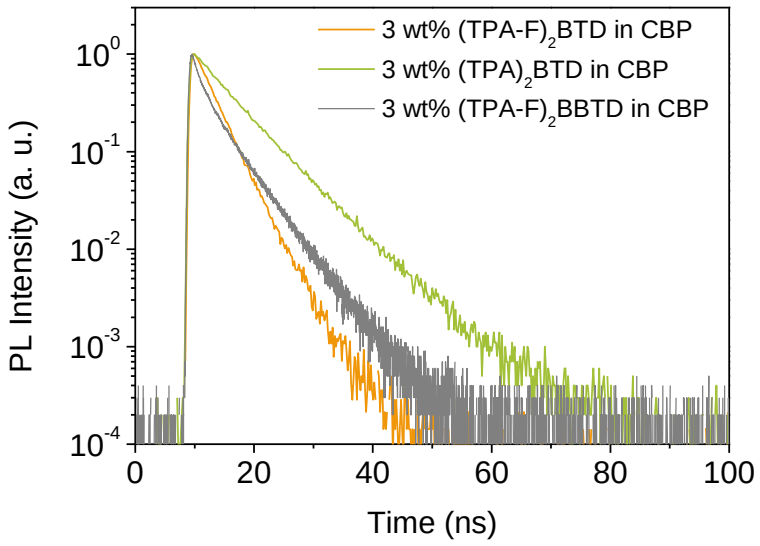

Figure 3-6. Time-dependent transient PL in nanosecond scale of $(TPA\text{-}F)_2BTD$, $(TPA)_2BTD$, and $(TPA\text{-}F)_2BBTD$ doped in CBP at 3 wt%.

Table 3-3. Photophysical properties of $(TPA\text{-}F)_2BTD$, $(TPA\text{-}F)_2BBTD$, $(TPA)_2BTD$, and $(TPA)_2BBTD$ in solution and blend films

Material	λ_{PL}[a] (nm)	PLQY[a] (%)	PLQY[b] (%)	τ[b] (ns)	k_r[b] (10^8 s^{-1})
$(TPA\text{-}F)_2BTD$	550	91.3	99.0	3.7	2.5
$(TPA\text{-}F)_2BBTD$	793	33.8	50.0	4.1	1.2
$(TPA)_2BTD$	608	81.0	82.8	6.7	1.2
$(TPA)_2BBTD$	886	4.1	7.2	/	/

[a] measured in toluene solution; [b] measured in blend film at 3 wt% doping concentration.

3.2.6 ASE properties and DFB lasers

According to the large *f*, as well as relatively large k_r of $(TPA\text{-}F)_2BTD$ and $(TPA\text{-}F)_2BBTD$, ASE of those dyes was investigated with the hope to obtain lower thresholds.

In the context of the yellow lasing dye $(TPA\text{-}F)_2BTD$, concentration-dependent ASE properties were systematically evaluated in CBP films doped with lasing dyes at 3 to 100 wt%. The thickness for all the prepared samples was >100 nm, which was thick enough to realize the edge-waveguide. **Figure 3-7 (a)** showed the output ASE intensity from the edge at different doping concentrations. It was evident that all the studied samples (at different doping ratios) showed ASE with a narrow spectral shape. ASE could be well evidenced from a change in intensity slope and a narrowing of the emission (i.e., a decrease of the FWHM) up to a value lower than 10 nm. Also, the ASE peaks varied from 549 to 573 nm (yellow) by changing the concentration ratios. As shown in Figure 3-7 (b), the ASE thresholds increased from 0.5 to 2.7 μJ cm^{-2} when going from 3 to 100 wt.% in CBP. To the best of our knowledge, the yellow ASE threshold around 0.5 μJ cm^{-2} was the lowest ever reported for yellow emission in the literature. The trend of the ASE threshold change was nearly in line with the k_r of 2.7×10^8 s^{-1} for 3 wt.%; 2.0×10^8 s^{-1} for 100 wt.%, because Einstein's B constant is proportional to k_r according to the following relationship:

$$B \propto \frac{c^3}{8\pi h\nu^3} k_{r;}\ E_{th} \propto \frac{1}{B}$$

where B is Einstein's B constant, c is the velocity of light, h represents Planck's constant, ν is the transition frequency, and E_{th} is the threshold. By comparison, owing to the smaller k_r, the $(TPA)_2BTD$ doped CBP blend film had a higher ASE threshold over 15 μJ cm^{-2}. Moreover, to assess the optical gain of the laser dyes, the σ_{em} has been estimated in the blend films. According to the Eq. 2-1, the corresponding σ_{em} at the ASE peak for $(TPA\text{-}F)_2BTD$ and $(TPA\text{-}F)_2BTD$ is exceeding 1.0×10^{-16} cm^2. By comparison, $(TPA)_2BTD$-based CBP blend films exhibited a smaller σ_{em} of 7.0×10^{-17} cm^2, which is consistent with the difference of their ASE thresholds. Also, I noticed that the host-free system also exhibited promising threshold values, which was benefitting from the effective limitation of intermolecular aggregation and reduced concentration quenching. The optimal threshold of only 1.9 μJ cm^{-2} was obtained.

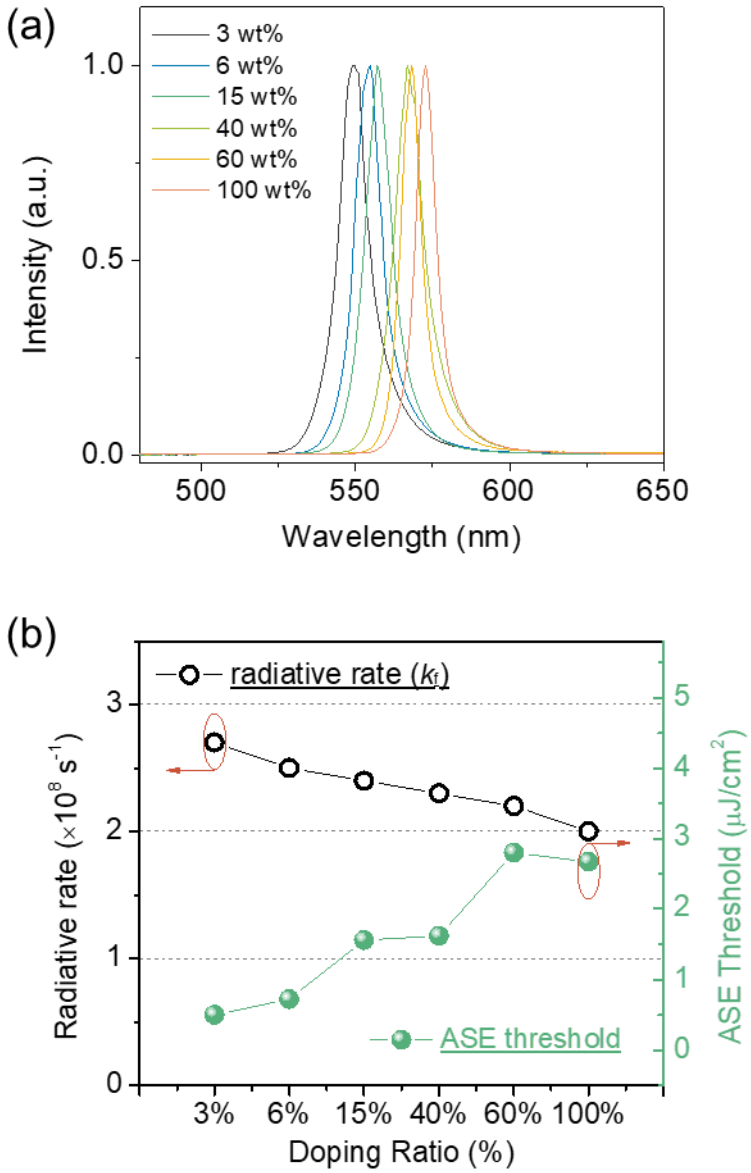

Figure 3-7. (a) ASE spectra of $(TPA\text{-}F)_2BTD$-based solid-state films with different doping ratios in a CBP host matrix. (b) Relationship of fluorescence radiative rate constants with the ASE thresholds as a function of doping ratio.

Moreover, owing to the elimination of host (CBP), crystallization and degradation would be easier to take place during the operation or preserving in the ambient condition. Therefore, as shown in **Figure 3-8**, the host-free system could tolerate moisture and oxygen under high nitrogen-laser (337 nm) excitation power above the threshold, and the ASE intensity could maintain nearly 90% of the original intensity

after one hour in the ambient condition, which was slightly more stable than the blend film.

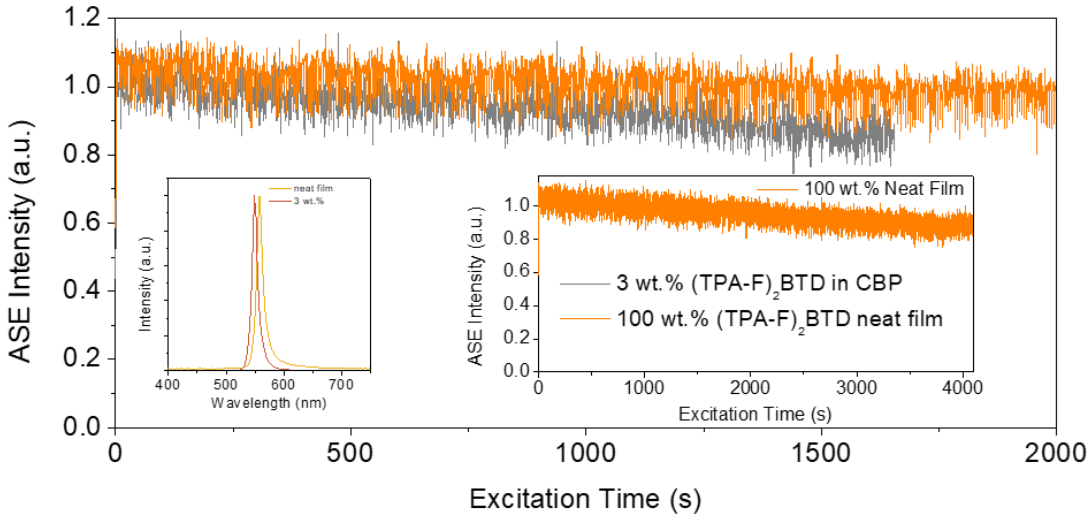

Figure 3-8. ASE stability of (TPA-F)$_2$BTD in CBP blend film and neat film.

For the NIR emitter (TPA-F)$_2$BBTD, though the k_r (~1.0×10^8 s^{-1}) was slightly lower than that of (TPA-F)$_2$BTD, which could be explained by the lower PLQYs, NIR ASE with low thresholds (going from 3.8 to 7.9 μJ cm^{-2}) still took place under wide-range doping concentrations from 1 to 40 wt.% with decreasing slope efficiency (the corresponding thickness of the samples was around 200 nm). The sharp decrease of FWHMs in the NIR-region spectra to <10 nm was plotted in **Figure 3-9 (a)**, with all the ASE wavelengths exceeding 780 nm (passing from 796 to 847 nm). It was highlighted that the lowest NIR ASE threshold (3.8 μJ cm^{-2}) was realized with the doping ratio 3 wt.% in CBP [Figure 3-9 (b)]. In contrast, ASE threshold based on (TPA)$_2$BBTD molecule without spacers was too high to detect, which could be caused by the serious energy-gap law and very strong donor-acceptor coupling effect in the short distance.

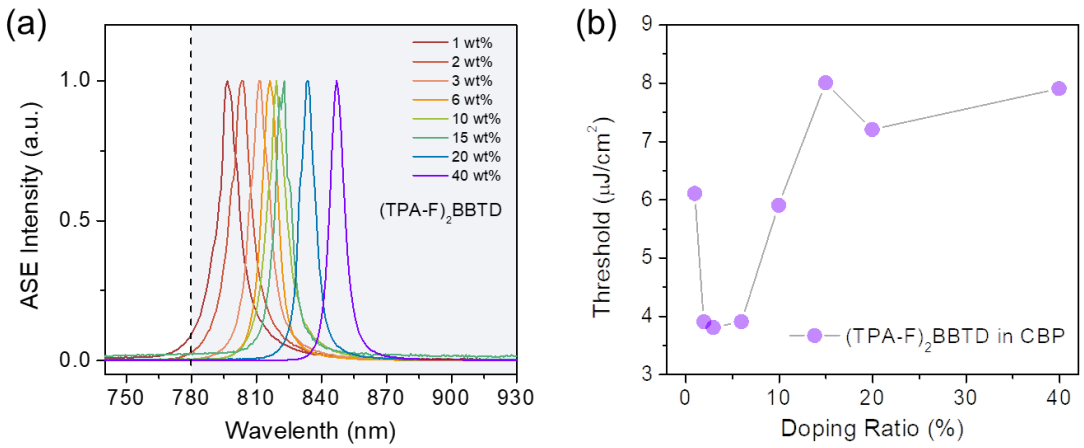

Figure 3-9. ASE performance of (TPA-F)$_2$BBTD-based solid-state films with different doping ratios in a CBP host matrix. (a) ASE spectra of all the films operating above the thresholds and (b) concentration dependence of the ASE thresholds.

Furthermore, I incorporated the 2nd-order DFB resonator structures to give a vertically output of the yellow and NIR lasers with low thresholds. Herein, diverse DFB grating periods (Λ_2) of 360, 370, and 380 nm were designed and used for a (TPA-F)$_2$BTD neat film. In parallel, Λ_2 of 505, 520, 535 and 550 nm were subsequently used to fabricate laser devices based on a 3 wt% (TPA-F)$_2$BBTD: CBP blend film, and the lowest threshold was around 1 μJ cm^{-2}. Consequently, wide-range tunable lasers with low laser thresholds from a (TPA-F)$_2$BTD neat film (from 558 to 586 nm) and 3 wt% (TPA-F)$_2$BBTD: CBP blend film (from 779 to 845 nm) were able to be obtained by rationally manipulating the vibronic bands spanning the entire emission spectrum (**Figure 3-10**). It should be noted that the relatively wide spectral shape of D-A type molecules enables the possibility of wider color-tunable lasers in a single molecule. Then, the polarization property of NIR laser based on the (TPA-F)$_2$BBTD: CBP blend film was further investigated. As shown in **Figure 3-11**, the 2nd-order DFB NIR laser exhibited a strong, linear transverse electric polarization, with a degree of polarization of 99.9% for the 2nd-order devices, which was accordingly calculated from the equation: $(I_{max} - I_{min})/(I_{max} + I_{min})$, where I_{max} and I_{min} denoted the maximum intensity at 90° and the minimum intensity at 0°, respectively. Consequently, the high degree value implied that the remarkable polarization characteristics of the NIR laser system.

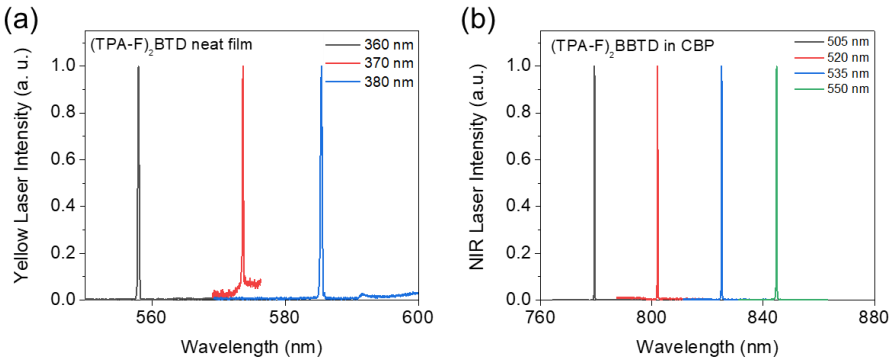

Figure 3-10. Yellow laser performance of (a) $(TPA\text{-}F)_2BTD$ neat films with different DFB grating periods of 360, 370, and 380 nm. NIR laser performance of (a) 3 wt% $(TPA\text{-}F)_2BBTD$: CBP blend films with different DFB grating periods of 505, 520, 535 and 550 nm. The insets were the grating patterns for 2nd-order DFB structures.

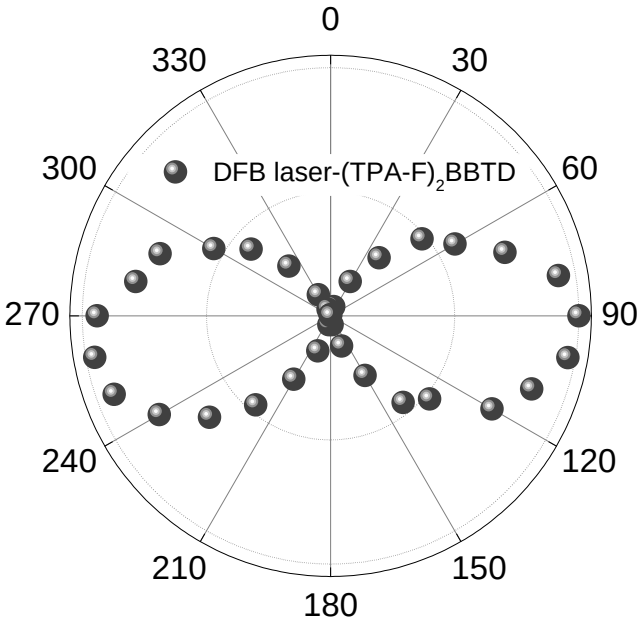

Figure 3-11. Polarization of NIR laser based on $(TPA\text{-}F)_2BBTD$ doped into a CBP film at 3 wt%.

Consequently, the yellow and NIR laser performance obtained in this work was compared with the representative lasers reported. As shown in **Figure 3-12**, organic lasers with low thresholds were mainly achieved in the blue regime, while the

performance far lagged behind for the yellow-NIR regime, in other words, the laser dyes with small energy gaps. In this work, the laser performances based on (TPA-F)$_2$BTD and (TPA-F)$_2$BBTD exhibited remarkably low laser thresholds, which paved an avenue to realize the excellent lasers from D-A type molecules with small energy gaps.

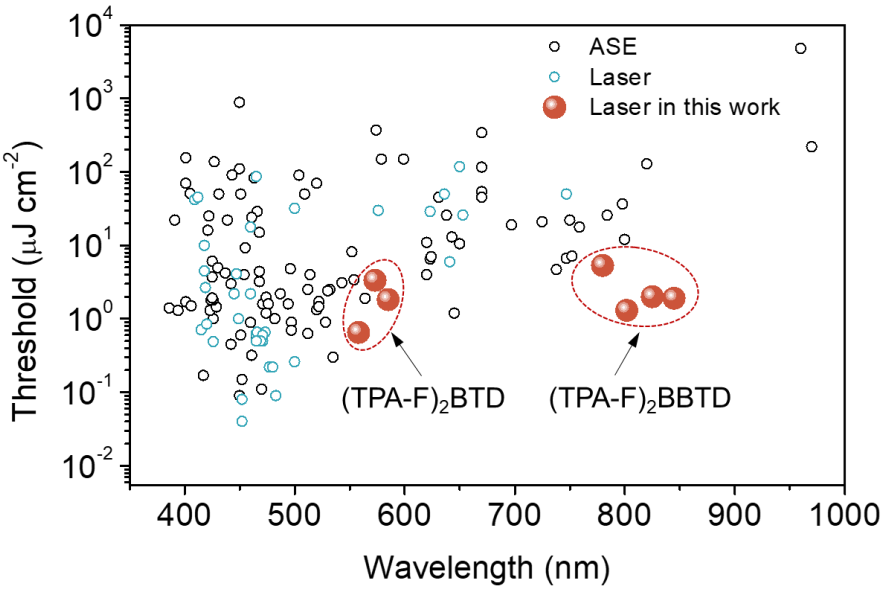

Figure 3-12. Summary of the ASE and laser performance measured from (TPA-F)$_2$BTD and (TPA-F)$_2$BBTD in this study and reported in literature.

3.2.7 EL performance

Both the laser dyes were next used to fabricate OLEDs. The specific device configuration was as follows: glass substrate/ITO (100 nm)/poly(3,4-ethylenedioxythiophene)-poly(styrenesulfonate) (PEDOT: PSS, 50 nm)/CBP: emitter (*X* wt%, *Y* nm)/2,2',2''-(1,3,5-benzinetriyl)-tris(1-phenyl-1H-benzimidazole) (TPBi, 65 nm)/LiF (0.8 nm)/Al (100 nm), where the PEDOT:PSS layer (HIL/HTL) and EML were solution-processed, *X* represented the quantity of dye compared to the quantity of CBP, and *Y* was the thickness of the EML. In parallel, the TPBi (ETL), LiF (EIL) and Al cathode were thermally evaporated. For the yellow emitter (TPA-F)$_2$BTD, the EML

based on a CBP host matrix was doped with different concentrations from 3 to 40 wt%, whose PLQYs of the corresponding solid-state films were close to the unity (>95%). With respect to the PL spectra, the EL spectra underwent a slight red-shift from 555 to 566 nm when increasing the doping concentrations, which may be because of the optical interference effect. For the 3 wt% blend films, the thickness of the EML was optimized from 60 to 150 nm by tuning the substrate rotation rate during spin-coating. As displayed in **Figure 3-13 (a)**, it was evident that the turn-on voltage of OLEDs decreased from 7.5 to 5.0 V by reducing the EML thickness from Y1 (~150 nm) to Y2 (~110 nm), Y3 (~80 nm), and Y4 (~60 nm). As presented in the EQE-*J* curve in Figure 3-13 (c), the highest EQE values of yellow emission increased from 1.65% to 2.67% when decreasing the thickness. It was worth noting that all the devices could tolerate high current density injection, and there was a slight efficiency rolloff within the variation of current density injection in several orders. For instance, the EQE of Y4 at 100 mA cm^{-2} maintained 1.70%.

For the NIR emitter $(TPA\text{-}F)_2BBTD$, the device configuration, similar to the one of $(TPA\text{-}F)_2BTD$, was also applied in the solution-processed device, which was also blended in CBP host with different concentration ratios from 1 to 6 wt%. More specifically, the turn-on voltage of NIR devices is around 8.0 V. In parallel, as displayed in Figure 3-13 (b), the corresponding EL spectra were located in the NIR regime, the spectral maximum showed red-shifting from 775 to 790 nm, with increasing the doping ratios. Owing to the limit of the energy-gap law effect, the highest EQE is 0.56%, and all the devices exhibited stable efficiency output with slight rolloff at high current density (over 100 mA cm^{-2}).

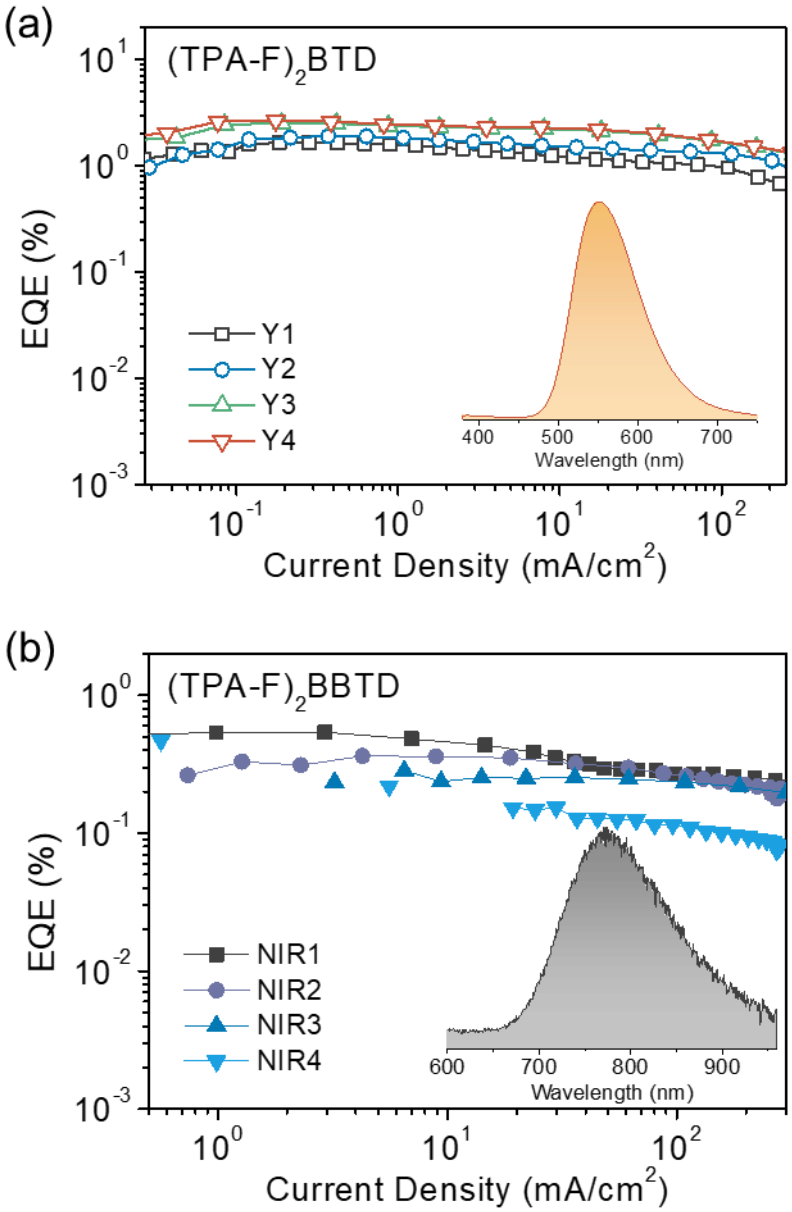

Figure 3-13. EQE vs. current density characteristics of (a) $(TPA\text{-}F)_2BTD$-based OLEDs with different EML thicknesses and (b) $(TPA\text{-}F)_2BBTD$-based OLEDs with different doping ratios (1 wt% in NIR1, 2 wt% in NIR2, 3 wt% in NIR3, and 6 wt% in NIR4).

3.3 Conclusion

In summary, D-spacer-A-spacer-D molecules have been successfully synthesized and characterized as promising laser candidates. The HOMO/LUMO wavefunction distribution was adjusted by inserting the fluorene spacer. A large *f* was obtained by tuning the relative D/A interplay strength to realize color-tunable organic lasing properties. Herein, TPA was selected as the donor moiety located at the end-sites of molecules, and BTD and BBTD with stronger electron-affinity capability, were chosen as acceptors for yellow ((TPA-F)$_2$BTD) and NIR ((TPA-F)$_2$BBTD) lasing dyes, respectively. In particular, the spacer-bridge connection between donor and acceptor moieties was composed of fluorene core, and the long alkyl chains were involved to guarantee the good solubility and suppressing of intermolecular ACQ in the case of (TPA-F)$_2$BTD. Therefore, the large k_r promoted the ASE/laser properties in a large range of doping concentrations. Among them, the yellow laser (λ_{peak} ~555 nm) from (TPA-F)$_2$BTD neat films, and NIR laser (λ_{peak} ~845 nm) from 3 wt% (TPA-F)$_2$BBTD:CBP blend films were respectively achieved.

3.4. Experimental sections

Molecule synthesis

Generally, these two dyes were synthesized in a similar manner using divergent synthesis in **Figure 3-14**. A Suzuki cross-coupling reaction was realized on the 4,7-dibromo-2,1,3-benzothiadiazole (or 4,8-dibromobenzo[1,2-c:4,5-c']bis-[1,2,5]thiadiazole) with the corresponding fluorene boronic ester (acid) counterpart in the presence of Pd(PPh$_3$)$_4$ yielding 1a and 1b with reasonable yields (ca. 75% and 48%, respectively). 1a (1b) was further brominated using bromine in chloroform to give 2a (2b). Subsequently, the dibromo-derivatives 2a (2b) were capped by using a Suzuki cross-coupling reaction with 4-(diphenylamino)phenylboronic acid yielding (TPA-F)$_2$BTD, 3a ((TPA-F)$_2$BBTD, 3b).

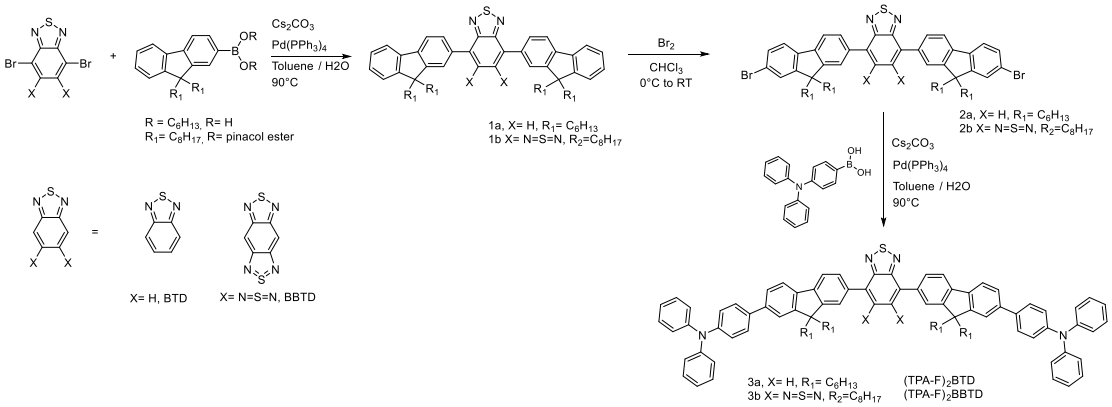

Figure 3-14. Synthesis pathway of $(TPA\text{-}F)_2BTD$ and $(TPA\text{-}F)_2BBTD$.

Synthesis of F_2-BTD (1a)

In a 50 mL round bottom flask, 4,7-dibromobenzo[c][1,2,5]thiadiazole (500 mg, 1.70 mmol, 1.0 eq.), 2-(9,9-dioctyl-9H-fluoren-2-yl)-4,4,5,5-tetramethyl-1,3,2-dioxaborolane (2.20 g, 4.25 mmol, 2.5 eq.) were suspended in DMF (30 mL) and the suspension was degassed with nitrogen for 20 min. Subsequently a degassed solution of K_2CO_3 (1.41 g, 10.2 mmol, 6.0 eq.) in water (5.1 mL) was added followed by the addition of a catalytic amount of $Pd(PPh_3)_4$. The reaction mixture was stirred at 95 °C for 16 h. At the end of the reaction, the solution was poured into 150 mL of water, and the aqueous layer was extracted with dichloromethane (DCM) for three times. The organic phases were combined, dried over $MgSO_4$ and evaporated to dryness. The crude was purified by column chromatography on silica gel using a gradient of solvent from 100% hexane to 90% hexane-10% DCM giving a yellow solid (1.16 g, yield: 75%). ^1H NMR ($CDCl_3$, 300 MHz, ppm) δ: 8.06 (dd, J=7.8 Hz, J=1.5 Hz, 2H), 7.98 (d, J=1.2 Hz, 2H), 7.92−7.87 (m, 3H), 7.83−7.77 (m, 2H), 7.44−7.33 (m, 6H), 2.17−1.97 (m, 8H), 1.27−1.07 (m, 40H), 0.87−0.73 (m, 20H); ^{13}C NMR ($CDCl_3$, 75 MHz, ppm) δ: 154.08, 153.47, 151.41, 151.33, 141.88, 140.58, 135.31, 134.73, 132.40, 128.23, 128.08, 127.58, 127.02, 123.95, 123.10, 120.16, 119.91, 112.79, 55.37, 40.38, 31.92, 30.16, 29.34, 23.98, 22.72, 14.19.

Synthesis of $(Br\text{-}F)_2$-BTD (2a)

In a 100 mL round bottom flask, 1a (500 mg, 0.547 mmol, 1.0 eq.) was dissolved in 40 mL of chloroform and the solution was stirred in an ice bath at 0 °C. Bromine (525 mg, 3.28 mmol, 6.0 eq.) in 10 mL of chloroform was added dropwise over 30 min. The solution was allowed to come back to room temperature and stirred for 4 additional hours. The solution was washed with a saturated solution of sodium thiosulfate then with brine. The DCM solution was dried over Na_2SO_4, then evaporated to dryness. The crude was purified by column chromatography on silica gel using a 90% hexane-10% DCM as eluent giving a yellow solid (574 mg, yield: 98%). ^{1}H NMR ($CDCl_3$, 300 MHz, ppm) δ: 8.03 (dd, J=7.9 Hz, J=1.5 Hz, 2H); 7.93 (s, 2H), 7.88 (s, 2H), 7.84 (d, J=7.92 Hz, 2H), 2.12−1.97 (m, 8H), 1.19−1.10 (m, 40H), 0.83−0.76 (m, 20H). ^{13}C NMR ($CDCl_3$, 75 MHz, ppm) δ: 154.43, 153.69, 150.91, 140.40, 139.81, 136.75, 133.67, 130.23, 128.49, 128.07, 126.42, 124.08, 121.48, 121.46, 119.98, 55.72, 40.33, 31.94, 30.12, 29.37, 29.34, 23.97, 22.75, 14.21.

Synthesis of $(TPA\text{-}F)_2$-BTD (3a)

In a 10 mL round bottom flask, 2a (250 mg, 0.233 mmol, 1.0 eq.) and (4-(diphenylamino)phenyl)boronic acid (169 mg, 0.583 mmol, 2.5 eq.) were solubilized in 4 mL of toluene and a solution of Cs_2CO_3 (759 mg, 2.33 mmol, 10.0 eq.) in 1.5 mL of water was added. The biphasing reaction mixture was degassed by bubbling nitrogen gas for 20 min. Then, a catalytic amount of $Pd(PPh_3)_4$ was added and the reaction was stirred at 90 °C for 16 h. After cooling down the mixture, water and DCM were added and the organic layer was washed with water. The organic phases were combined, dried over Na_2SO_4 and evaporated to dryness. The crude was purified by column chromatography on silica gel using a gradient of solvent from 90% hexane-10% DCM to 70% hexane-30% DCM giving an orange solid (m= 202 mg, yield: 62%). ^{1}H NMR ($CDCl_3$, 300 MHz, ppm) δ: 8.10 (dd, J=7.9 Hz, 2H), 8.02 (s, 2H), 7.93-7.90 (m, 4H), 7.84 (d, J=8.3 Hz, 2H), 7.64−7.61 (m, 8H), 7.34−7.29 (m, 8H), 7,24−7,18 (m, 12H), 7.10−7.05 (m, 4H), 2.16−2.09 (m, 8H), 1.23−1.14 (m, 40H), 0.90−0.80 (m, 20H); ^{13}C NMR ($CDCl_3$, 75 MHz, ppm) δ: 154.51, 152.16, 151.48, 147.82, 147.24, 141.22, 139.88, 139.68, 136.22, 135.71, 133.69, 129.42, 128.37, 128.01, 127.96, 125.76,

124.51, 124.15, 124.04, 123.06, 121.15, 120.37, 119.96, 55.45, 40.50, 31.94, 30.22, 29.39, 29.36, 24.07, 22.74, 14.21.

Synthesis of F_2-BBTD (1b)

In a 50 mL round bottom flask, 4,7-dibromobenzo[1,2-c:4,5-c']bis([1,2,5]thiadiazole) (350 mg, 0.994 mmol, 1.0 eq.) and (9,9-dihexyl-9H-fluoren-2-yl)boronic acid (940 mg, 2.49 mmol, 2.5 eq.) were dissolved in 20 mL of toluene and a solution of Cs_2CO_3 (3.24 g, 9.94 mmol, 10.0 eq.) in 10 mL of water was added. The biphasing reaction was degassed by bubbling nitrogen gas for 20 min. Then, a catalytic amount of $Pd(PPh_3)_4$ was added and the reaction mixture was stirred at 90 °C for 16 h. After cooling down the mixture, water and DCM were added and the organic layer was washed with water. The organic phases were combined, dried over Na_2SO_4 and evaporated to dryness. The crude was purified by column chromatography on silica gel using a gradient of solvent from 90% hexane-10% DCM to 66% hexane-34% DCM giving an orange solid (410 mg, yield: 48%). ^{1}H NMR ($CDCl_3$, 300 MHz, ppm) δ: 8.42 (d, 2H, J=1.1 Hz), 8.37 (dd, 2H, J=7.92 Hz, J=1.47 Hz), 8.04 (d, 2H, J=7.94 Hz), 7.90-7.87 (m, 2H), 7.52−7.43 (m, 6H), 2.24−2.11 (m, 8H), 1.26−1.23 (m, 26H), 1.04−0.84 (m, 22H). ^{13}C NMR ($CDCl_3$, 75 MHz, ppm) δ: 153.08, 151.85, 150.62, 141.91, 140.67, 133.87, 130.88, 127.59, 127.31, 127.01, 123.07, 121.84, 120.28, 119.58, 55.34, 40.33, 31.65, 29.91, 24.07, 22.71, 14.20.

Synthesis of (Br-F)$_2$-BBTD (2b)

In a 50 mL round bottom flask, 1b (200 mg, 0.233 mmol, 1.0 eq.) was dissolved in 20 mL of chloroform and the solution was stirred in an ice bath at 0 °C. Bromine (223 mg, 1.40 mmol, 6.0 eq) in 10 mL of chloroform was added dropwise over 30 min. The solution was allowed to come back to room temperature and stirred for 4 additional hours. The resulting solution was washed with a saturated solution of sodium thiosulfate then with brine. The DCM solution was dried over Na_2SO_4 then evaporated to dryness. The crude was purified by column chromatography on silica gel using an 80% hexane-20% DCM as eluent giving a yellow solid (182 mg, yield: 77%). ^{1}H NMR ($CDCl_3$, 300

MHz, ppm) δ: 8.31-8.28 (m, 4H), 7.94 (d, J=Hz, 2H), 7.68 (d, J=Hz, 2H), 7.56−7.51 (m, 4H), 2.18−1.94 (m, 8H), 1.22−1.15 (m, 24 H), 0.91−0.78 (m, 20H). ^{13}C NMR ($CDCl_3$, 75 MHz, ppm) δ: 154.12, 153.09, 150.37, 140.86, 139.71, 134.31, 131.04, 130.29, 127.35, 126.48, 121.82, 121.73, 121.64, 119.72, 55.74, 40.24, 31.66, 29.86, 24.06, 22.75, 14.21.

Synthesis of $(TPA\text{-}F)_2$-BBTD (3b)

In a 10 mL round bottom flask, 2b (150 mg, 0.147 mmol, 1.0 eq.) and (4-(diphenylamino)phenyl)boronic acid (107 mg, 0.369 mmol, 2.5 eq.) were dissolved in 4 mL of toluene and a solution of Cs_2CO_3 (481 mg, 1.47 mmol, 10.0 eq.) in 1.5 mL of water was added. The biphasing reaction was degassed by bubbling nitrogen gas for 20 min. Then, a catalytic amount of $Pd(PPh_3)_4$ was added and the reaction mixture was stirred at 90 °C for 16 h. After cooling down the mixture, water and DCM were added and the organic layer was washed with water. The organic phases were combined, dried over Na_2SO_4 and evaporated to dryness. The crude was purified by column chromatography on silica gel using a gradient of solvent from 80% hexane-20% DCM 60% hexane-40% DCM giving an orange solid (115 mg, yield: 58%). ^{1}H NMR (CD_2Cl_2, 300 MHz, ppm) δ: 8.38 (d, ^{4}J=0.9 Hz, 2H), 8.32 (dd, ^{3}J=8.0 Hz, ^{4}J=1.3 Hz, 2H), 7.98 (d, ^{3}J=7.8 Hz, 2H), 7.89 (d, ^{3}J=7.8 Hz, 2H), 7.70−7.61 (m, 8H), 7.35−7.27 (m, 8H), 7.23−7.13 (m, 12H), 7.11−7.02 (m, 4H), 2.22−2.09 (m, 8H), 1.24−1.16 (m, 24H), 0.97−0.92 (m, 8H), 0.81 (t, 3J=6.7 Hz, 12H); ^{13}C NMR (CD_2Cl_2, 75 MHz, ppm) δ: 153.58, 153.13, 151.33, 148.27, 147.80, 142.00, 140.57, 140.03, 136.01, 134.50, 131.67, 129.87, 128.37, 127.84, 126.17, 124.96, 124.50, 123.56, 122.13, 121.71, 121.06, 119.85, 55.96, 40.79, 32.15, 30.36, 24.65, 23.20, 14.44.

Sample preparation

The blended films (hosted by CBP) and neat films for photophysical and ASE measurements, were spin-coated on cleaned fused-silica substrates and non-fluorescent glass substrates from the prepared chloroform solution with different doping

concentrations. The film thickness was controlled by tuning the spin-coating rotation speed, and determined by a Dektak profilometer.

Photophysical characterization of absorption, PL spectra, PLQY and time-dependent transient PL

Absorption spectra for all the samples were measured by a Lambda 950 KPA spectrophotometer (PerkinElmer, USA). Steady-state PL spectra were recorded using an FP-8600 PL spectrometer (JASCO, Japan). PLQYs were estimated using an integrating sphere system coupled with a photonic multichannel analyzer (Hamamatsu Photonics C11347-11, PMA-11, Japan). All the samples were excited at 340 nm. The time-dependent transient PL was measured using a Quantaurus-Tau fluorescence lifetime measurement system (C11367-03, Hamamatsu Photonics, Japan) under the excitation of 340 nm.

Quantum chemical calculation

The DFT calculation of $(TPA\text{-}F)_2BTD$ and $(TPA\text{-}F)_2BBTD$ was subsequently carried out using the program Gaussian 16, and the corresponding geometries were optimized at B3LYP/6-31G(d) level. The alkyl chains were substituted with ethyl groups. The TD-DFT calculations were operated at B3LYP/6-31G(d) level.

Characterization of ASE properties

The as-prepared solid-state blending or neat films were photoexcited by a nitrogen laser (the excitation wavelength is 337 nm, with a pulse width of 800 ps and repetition rate of 8 Hz, KEN2020, Usho Optical Systems Co., Ltd.) in the ambient condition. The substrates were cut from the center for better waveguide emission. Neutral density filters were set up to vary the output energy of excitation pulses. The cylindrical lens was used to transform the excitation beam into a uniform stripe for stable excitation. The edge-emission from the waveguide edge was detected by an optical fiber, which was connected to a spectrometer (PMA-12, Hamamatsu Photonics, Japan).

DFB structure fabrication

Glass substrates covered with a 1000 nm silicon dioxide (SiO_2) layer were used for DFB fabrication. The substrates were subsequently cleaned up by detergent, pure water, acetone, and isopropanol (IPA) and then treated by UV-ozone. Next, hexamethyldisilazane was spin-coated onto the substrates at 4000 rpm for 15 s, followed by annealing at 120 ℃ for 120 s. Later, a reasist film composed of ZEP520A-7 solution was then spin-coated at 4000 rpm for 30 s, and then baked at 180 ℃ for 240 s. The electron-beam lithography was conducted to obtain the grating patterns on the resist layer by the JBX-5500SC system. Then, the development of the grating pattern was taken place in a developer solution ZED-N50. In the process of etching, the resist layer was employed as the protecting layer while the substrates undertook the plasma-etching with CHF_3 using an EIS-200ERT etching system (Elionix). For completely removing the resist layer from the substrates, they were plasma-etched with O_2 using an FA-1EA etching system (SAMCO).

Device fabrication and measurement.

The hole-transporting material PEDOT:PSS was purchased from Heraeus Clevios, whereas CBP and TPBi were supplied by TCI chemicals. The PEDOT:PSS layer was spin-coated on the cleaned pre-patterned ITO substrates, and then thermally annealed at 180 ℃ for 15 minutes. Neat and blend films with different doping concentrations hosted by CBP were subsequently spin-coated upon the PEDOT:PSS layer. The TPBi ETL, LiF EIL and Al cathode were thermally evaporated through shadow masks to complete the devices. Finally, the devices were encapsulated in the glovebox under the nitrogen-gas circumstance to prevent the detrimental influence of oxygen and moisture. For OLED performance measurement, $J-V$ characteristics were measured under DC driving using a constant source meter, Keithley 2400, Keithley Instruments Inc., and the EL spectra were recorded by an optical fiber connected to a spectrometer (PMA-12, Hamamatsu Photonics, Japan).

References

[1] I. D. W. Samuel, G. A. Turnbull, *Chem. Rev.* **2007**, *107*, 1272.

[2] V. G. Kozlov, V. Bulovic, P. E. Burrows, S. R. Forrest, *Nature* **1997**, *389*, 362.

[3] B. K. Yap, R. D. Xia, M. Campoy-Quiles, P. N. Stavrinou, D. D. C. Bradley, *Nat. Mater.* **2008**, *7*, 376.

[4] Y. Jiang, Y. Y. Liu, X. Liu, H. Lin, K. Gao, W. Y. Lai, W. Huang, *Chem. Soc. Rev.* **2020**, *49*, 5885.

[5] A. J. Kuehne, M. C. Gather, *Chem. Rev.* **2016**, *116*, 12823.

[6] R. Xia, W.-Y. Lai, P. A. Levermore, W. Huang, D. D. C. Bradley, *Adv. Funct. Mater.* **2009**, *19*, 2844.

[7] T. Aimono, Y. Kawamura, K. Goushi, H. Yamamoto, H. Sasabe, C. Adachi, *Appl. Phys. Lett.* **2005**, *86*, 071110.

[8] R. Xia, G. Heliotis, Y. Hou, D. D. C. Bradley, *Org. Electron.* **2003**, *4*, 165.

[9] A. D'Aleo, M. H. Sazzad, D. H. Kim, E. Y. Choi, J. W. Wu, G. Canard, F. Fages, J. C. Ribierre, C. Adachi, *Chem. Commun.* **2017**, *53*, 7003.

[10] H. R. Haghighi, S. Forget, S. Chenais, A. Siove, M. C. Castex, E. Ishow, *Appl. Phys. Lett.* **2009**, *95*, 033305.

[11] X. Wang, Z.-Z. Li, M.-P. Zhuo, Y. Wu, S. Chen, J. Yao, H. Fu, *Adv. Funct. Mater.* **2017**, *27*, 1703470.

[12] M. Mamada, T. Fukunaga, F. Bencheikh, A. S. D. Sandanayaka, C. Adachi, *Adv. Funct. Mater.* **2018**, *28*, 1802130.

[13] Z. Xu, Q. Liao, Q. Shi, H. Zhang, J. Yao, H. Fu, *Adv. Mater.* **2012**, *24*, OP216.

[14] W.-Y. Lai, R. Xia, Q.-Y. He, P. A. Levermore, W. Huang, D. D. C. Bradley, *Adv. Mater.* **2009**, *21*, 355.

[15] Y. Qian, Q. Wei, G. Del Pozo, M. M. Mróz, L. Lüer, S. Casado, J. Cabanillas-Gonzalez, Q. Zhang, L. Xie, R. Xia, W. Huang, *Adv. Mater.* **2014**, *26*, 2937.

[16] T. Matsushima, S. Yoshida, K. Inada, Y. Esaki, T. Fukunaga, H. Mieno, N. Nakamura, F. Bencheikh, M. R. Leyden, R. Komatsu, C. Qin, A. S. D. Sandanayaka, C. Adachi, *Adv. Funct. Mater.* **2019**, *29*, 1807148.

[17] T. Matsushima, S. Yoshida, K. Inada, Y. Esaki, T. Fukunaga, H. Mieno, N. Nakamura, F. Bencheikh, M. R. Leyden, R. Komatsu, C. Qin, A. S. D. Sandanayaka, C. Adachi, *Adv. Funct. Mater.* **2019**, *29*, 1807148.

[18] Y. Hu, F. Bencheikh, S. Chénais, S. Forget, X. Liu, C. Adachi, *Appl. Phys. Lett.* **2020**, *117*, 153301.

[19] C. A. M. Senevirathne, A. S. D. Sandanayaka, B. S. B. Karunathilaka, T. Fujihara, F. Bencheikh, C. Qin, K. Goushi, T. Matsushima, C. Adachi, *ACS Photon.* **2021**, *8*, 1324.

[20] A. S. D. Sandanayaka, K. Yoshida, M. Inoue, C. Qin, K. Goushi, J.-C. Ribierre, T. Matsushima, C. Adachi, *Adv. Opt. Mater.* **2016**, *4*, 834.

[21] A. S. D. Sandanayaka, T. Matsushima, F. Bencheikh, K. Yoshida, M. Inoue, T. Fujihara, K. Goushi, J. C. Ribierre, C. Adachi, *Sci. Adv.* **2017**, *3*, e1602570.

[22] A. S. D. Sandanayaka, T. Matsushima, F. Bencheikh, S. Terakawa, W. J. Potscavage, C. Qin, T. Fujihara, K. Goushi, J.-C. Ribierre, C. Adachi, *Appl. Phys. Express* **2019**, *12*, 061010.

[23] S.-J. Chang, X. Liu, T.-T. Lu, Y.-Y. Liu, J.-Q. Pan, Y. Jiang, S.-Q. Chu, W.-Y. Lai, W. Huang, *J. Mater. Chem. C* **2017**, *5*, 6629.

[24] D.-H. Kim, A. D'Aléo, X.-K. Chen, A. D. S. Sandanayaka, D. Yao, L. Zhao, T. Komino, E. Zaborova, G. Canard, Y. Tsuchiya, E. Choi, J. W. Wu, F. Fages, J.-L. Brédas, J.-C. Ribierre, C. Adachi, *Nat. Photon.* **2018**, *12*, 98.

[25] G. Qian, Z. Zhong, M. Luo, D. Yu, Z. Zhang, Z. Y. Wang, D. Ma, *Adv. Mater.* **2009**, *21*, 111.

[26] C. Wang, X.-L. Li, Y. Gao, L. Wang, S. Zhang, L. Zhao, P. Lu, B. Yang, S.-J. Su, Y. Ma, *Adv. Opt. Mater.* **2017**, *5*, 1700441.

[27] Y. Yang, R. T. Farley, T. T. Steckler, S. H. Eom, J. R. Reynold, K. S. Schanze, J. Xue, *Appl. Phys. Lett.* **2008**, *93*, 163305.

[28] Z. R. Grabowsk, K. Rotkiewicz, W. Rettig, *Chem. Rev.* **2003**, *103*, 3899.

[29] S. Yamada, J. Bessho, H. Nakasato, O. Tsutsumi, *Dyes Pigments* **2018**, *150*, 89.

[30] S. Tarkuc, Y. A. Udum, L. Toppare, *Polymer* **2009**, *50*, 3458.

[31] K. R. Justin Thomas, J. T. Lin, M. Velusamy, Y. T. Tao, C. H. Chuen, *Adv. Funct.*

Mater. **2004**, *14*, 83.

[32] W. Li, Y. Pan, L. Yao, H. Liu, S. Zhang, C. Wang, F. Shen, P. Lu, B. Yang, Y. Ma, *Adv. Opt. Mater.* **2014**, *2*, 892.

[33] H. Usta, D. Alimli, R. Ozdemir, E. Tekin, F. Alkan, R. Kacar, A. G. Altas, S. Dabak, A. G. Gürek, E. Mutlugun, A. F. Yazici, A. Can, *J. Mater. Chem. C* **2020**, *8*, 8047.

[34] Y. Gao, S. Zhang, Y. Pan, L. Yao, H. Liu, Y. Guo, Q. Gu, B. Yang, Y. Ma, *Phys. Chem. Chem. Phys.* **2016**, *18*, 24176.

[35] W. Li, Y. Pan, R. Xiao, Q. Peng, S. Zhang, D. Ma, F. Li, F. Shen, Y. Wang, B. Yang, Y. Ma, *Adv. Funct. Mater.* **2014**, *24*, 1609.

Chapter 4. Quasi-planar donor-acceptor structure from intramolecular lock toward narrowband EL and TADF lasers

4.1 Introduction

Pursuing a high EL efficiency and ultrapure luminescence for wider-color gamuts are two crucial prerequisites of optoelectronic devices, such as OLEDs[1-5] and cutting-edged OSLDs for realizing the terminal display technology.[6-16] To improve the EQE of OLEDs and trigger the OSLDs under a much reduced threshold, the fundamental purpose is to fully harvest generated excitons for radiation.[7] In particular, the utilization of spin-forbidden triplets, which account for 75% among electrically-generated excitons, plays a critical role.[17] Recently, TADF materials with an IQE of ≈100% have been extensively developed.[18-25] To effectively minimize ΔE_{ST}, so far, the most efficient TADF emitters were constructed by twisted D-A structures to separate frontier molecular orbitals.[26-33] However, such structures are often accompanied by a large Stokes-shift and a broadened spectrum (with FWHM >70 nm) because of the structural relaxation at the S_1 state and vibronic coupling between the S_1 and the S_0, which brought about detrimental effects on the luminescence purity.[10, 22, 26, 34-36] Moreover, the HOMO/LUMO separation inducing an ICT state would retard the radiation rate, and therefore inhibits the ASE/laser actions. There were very rare TADF candidates that could exhibit ASE actions. Very recently, the standard of Recommendation ITU-R BT.2020 (Rec. 2020) for ultrahigh definition displays further stimulated the demand of organic emitters with high efficiency and purity.[37, 38] However, even the most cutting-edged TADF emitters were still hard to approach the Commission Internationale de l'Eclairage (CIE) coordinates (0.131, 0.046) required by Rec.2020, which required the emission in the violet-blue region with high color purity.[34, 39]

In this contribution, I used a single intramolecular-lock strategy to planarize *para*-linked donor (phenoxazine or acridine) and acceptor (mesitylboron). Two locked TADF emitters, PXZN-B (phenoxazine) and DMACN-B (acridine) exhibited very small torsion angles of 20.8 ° and 28.0 °, respectively, leading to that the classic *twisted* D-A structure was largely eliminated. Thanks to the enhanced molecular rigidity and suppressed rotation or vibration, PXZN-B and DMACN-B exhibited deep-blue and

violet-blue structureless PL with smaller FWHMs of 44 and 29 nm, respectively. Subsequently, the corresponding OLEDs performed the excellent CIE coordinates for PXZN-B (0.133, 0.147) and DMACN-B (0.151, 0.045). Also, high EQEs of over 10% were achieved for both TADF emitters. It was worth noting the CIE coordinates (0.151, 0.045) of DMACN-B-based emission closely satisfy Rec.2020 standard (0.131, 0.046). Encouragingly, they also had a very fast $S_1 \rightarrow S_0$ transition with $k_r > 10^8\ s^{-1}$ owing to the appreciable HOMO/LUMO overlap, which induced a large f and transition dipole moment ($\vec{\mu}$) in the locked D-A structures. Therefore, both the locked D-A type TADF emitters, PXZN-B and DMACN-B, exhibited ASE and laser characteristics with low thresholds, torching the potential for revealing the TADF-based lasing and eventually approaching monochromatic emission on the CIE spectral locus, without the integration of complicated color filters.

4.2 Results and discussion

4.2.1 Molecular structures

The molecular structures of DMACN-B and PXZN-B are shown in **Figure 4-1 (a)**. The twisted conformation of conventional D-A TADF emitters was locked from diarylamine donor moieties. For the acceptor segment, bulky mesityl groups were introduced to prevent the hydrolysis of boron atoms by moisture. Besides, the steric hindrance in acceptor moieties could effectively reinforce the rigidity to restrict the bond free-rotation, thus minimizing the non-radiative relaxation. In particular, by tuning the torsion angle via “intramolecular lock”, a series of remarkable changes for optoelectronic characteristics, including photophysical and EL properties, would subsequently arise and will be discussed below.

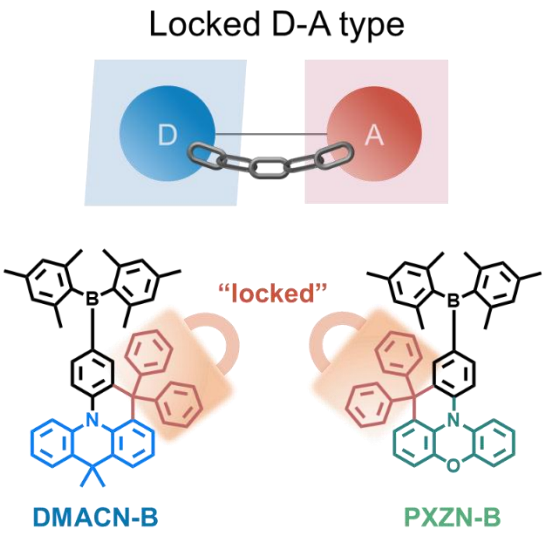

Figure 4-1. (a) Molecular design of the locked D-A type structures of DMACN-B and PXZN-B.

4.2.2 Theoretical calculation

To evaluate the possible structural change for these two D-A type molecules, a DFT simulation was performed to investigate the effects of the intramolecular locking strategy. Besides locked DMACN-B and PXZN-B, their lock-free analogs were also calculated for comparison. As shown in **Figure 4-2**, compared with the lock-free analogs, the locked structures had a smaller torsion angle (~90° vs. ~30°) between the donor and the acceptor planes.

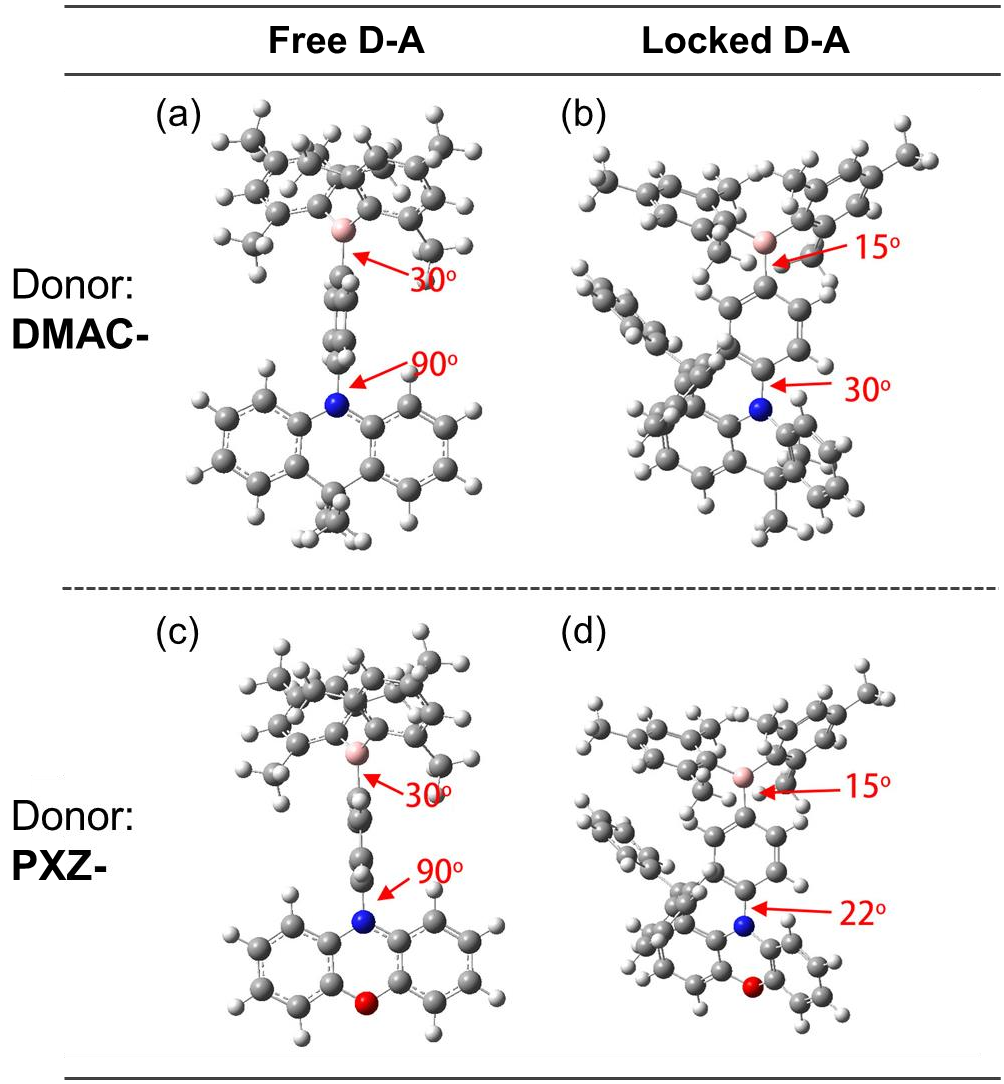

Figure 4-2. Theoretical calculation on two torsion angles of free and locked molecules at the ground state.

As shown in **Figure 4-3**, the π orbital interaction between D and A consequently led to: (i) a deeper HOMO level and shallower LUMO level because of the larger energy level of the locked fragments, and thus a larger HOMO-LUMO gap; (ii) HOMO of donor delocalized to benzene of acceptor moiety, which resulted in the smaller hole-electron distance and a larger hole-electron overlap. Therefore, the S_1 energy level of locked structures tended to exhibit a more LE character, a shorter transition wavelength, and a larger *f*, which should lead to higher PLQY and larger k_r. The S_1 and T_1 of the locked structure had a larger LE character compared with those of the lock-free structure. As expected in Figure 4-3 (c), because of the closer distance hole/electron

distance, the HOMO/LUMO wavefunction overlap (Sr) became larger in the locked D-A molecules. Thus, the S_1 and T_1 of the locked D-A structure have a larger LE character (Sr ~0.5) compared with those of the lock-free structure (Sr ~0.1).

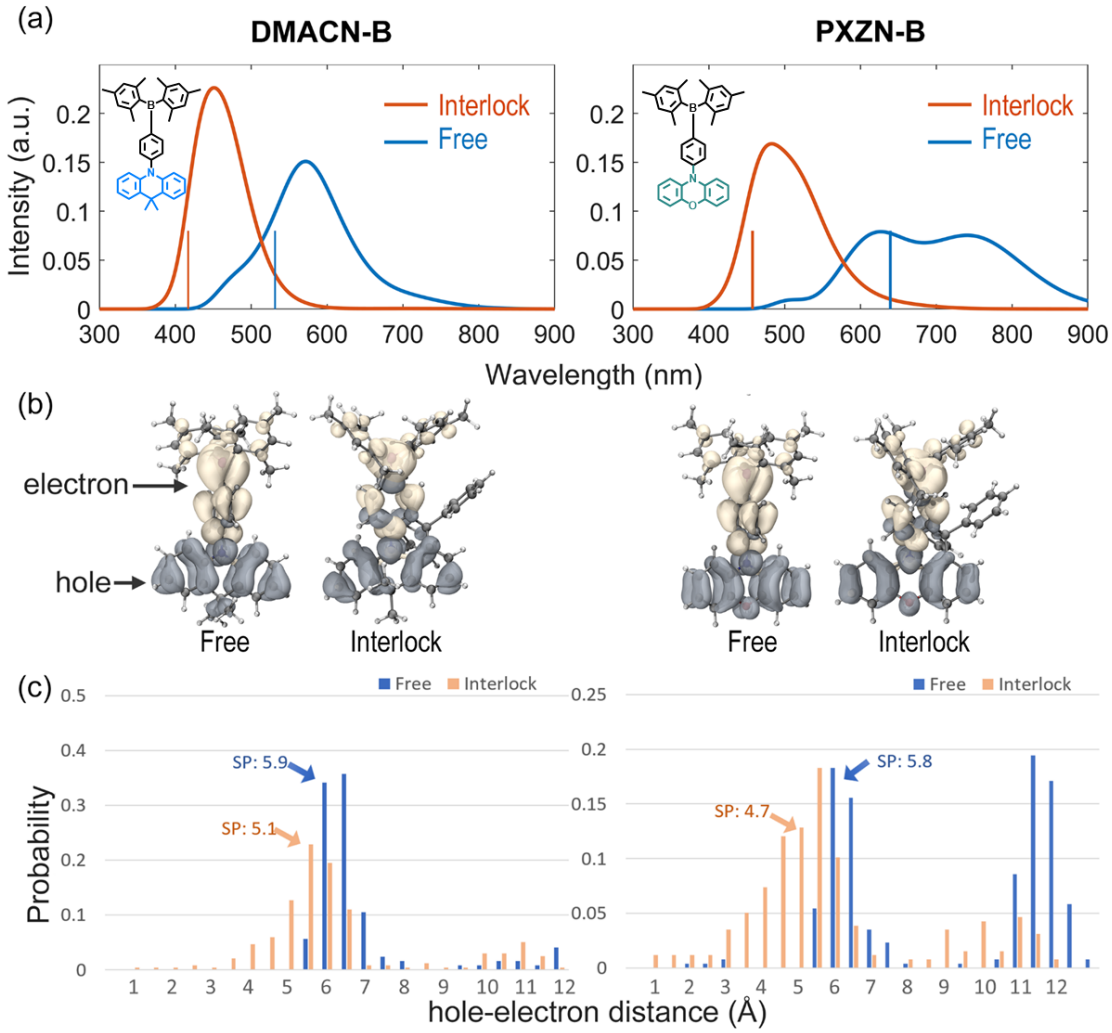

Figure 4-3. (a) Simulated fluorescence spectra of free and locked DMACN-B and PXZN-B from the ensemble. The insets are the molecular structures of free-type DMACN-B and PXZN-B. The vertical lines corresponded to the location of the stationary point (SP) transition. (b) Hole and electron distributions. (c) Hole-electron centroid distance distribution of the ensemble. The stationary points (SP) are annotated by the arrow.

Besides the blueshift of the luminescence spectra, as shown in **Figure 4-4**, the locked D-A molecules DMACN-B and PXZN-B exhibited narrowband emission with smaller FWHMs, because of the rigid quasi-planar D-A structures. Therefore, the radiative transition channels of the locked DMACN-B and PXZN-B were remarkably condensed within the emissive zone, which also led to the much larger *f* compared to the free-lock D-A type analogs.

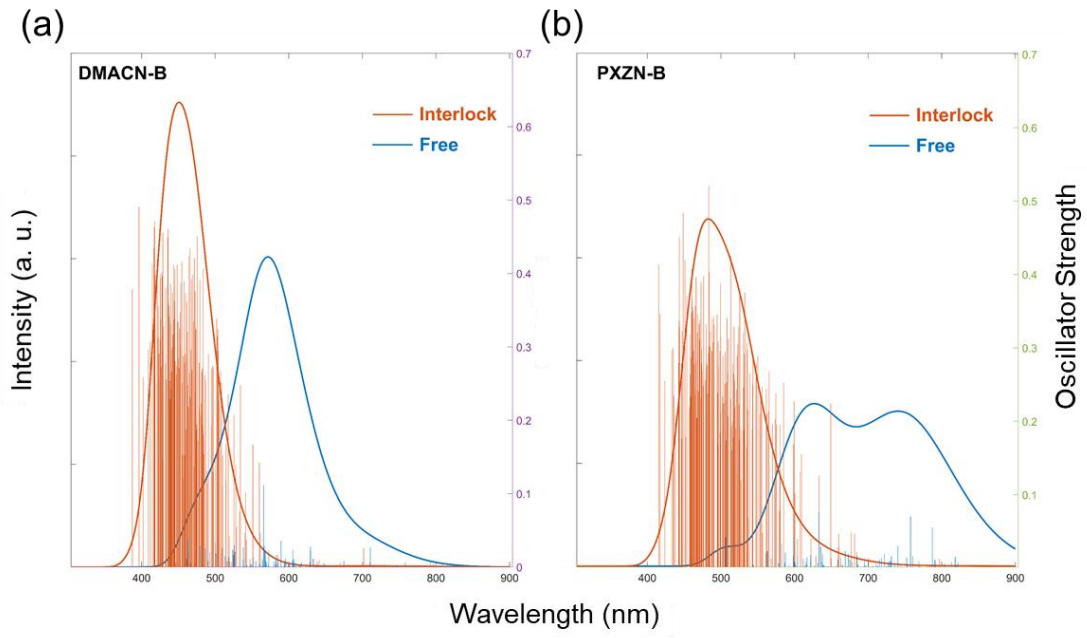

Figure 4-4. Simulated fluorescence spectra of free D-A and locked D-A type DMACN-B and PXZN-B from the ensemble. The vertical lines corresponded to the *f* for all the transitions in the ensemble.

4.2.3 Single-crystal analysis

To experimentally confirm the actual spatial arrangements of the locked D-A molecules, single-crystal structures of locked PXZN-B and DMACN-B were further studied. From the reported work, the torsion angles for typical D-A type emitters with the same D/A moieties were 87.3 ° (phenoxazine as donor) and 88.4 ° (9,9-dimethyl-9,10-dihydroacridine as donor), respectively. By comparison, as illustrated in **Figure 4-5**, after inserting the diphenyl methylene lock, the torsion angles between B-C benzene skeleton and donor planes dramatically decreased to 20.8 °for PXZN-B and

28.0 ° for DMACN-B, demonstrating that the orthogonal D-A structure was largely eliminated, which was also consistent with the trend of the calculated results.

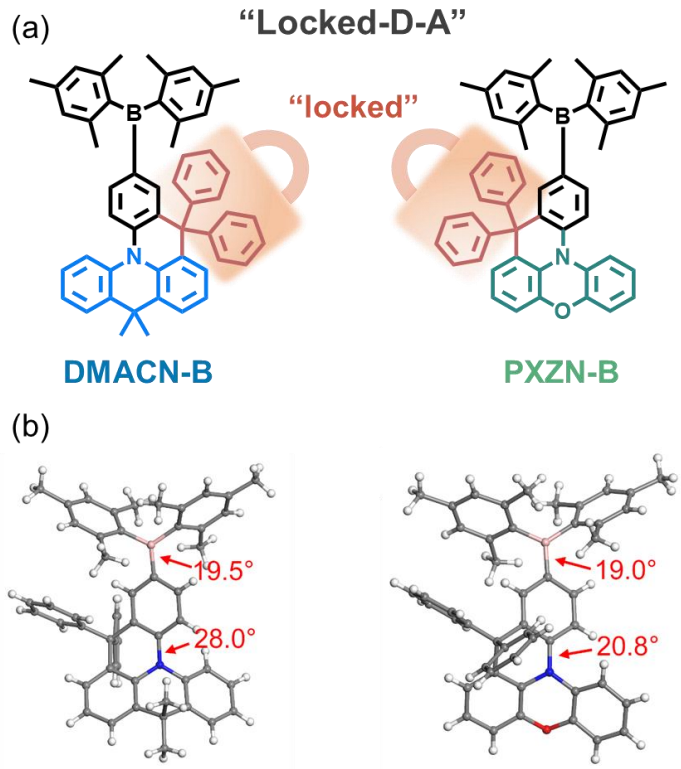

Figure 4-5. (a) Molecular and (b) single-crystal structures of locked D-A type DMACN-B and PXZN-B.

4.2.4 Photophysical properties

To confirm the conjecture mentioned above, the photophysical properties for locked D-A type compounds PXZN-B and DMACN-B were measured. The investigation of absorption, fluorescence, and phosphorescence in toluene was conducted. As shown in **Figure 4-6** (a) and (b), both two locked D-A emitters DMACN-B and PXZN-B exhibited small FWHMs of 29 and 44 nm, respectively. In addition, the corresponding emission peaks were located in the deep blue (430 nm) and pure blue (454 nm) regions. In addition, both locked DMAC-B and PXZN-B molecules exhibited high PLQYs over 90%, and the corresponding decay lifetime were 3.8 and 4.3 ns for locked DMACN-B and PXZN-B, respectively. Therefore, a large radiative

rate over 10^8 s^{-1} was achieved in these two molecules. Moreover, the experimental ΔE_{ST} of the locked D-A molecules DMACN-B and PXZN-B was estimated to be 0.27 and 0.28 eV, respectively, which is promising to trigger the TADF actions.

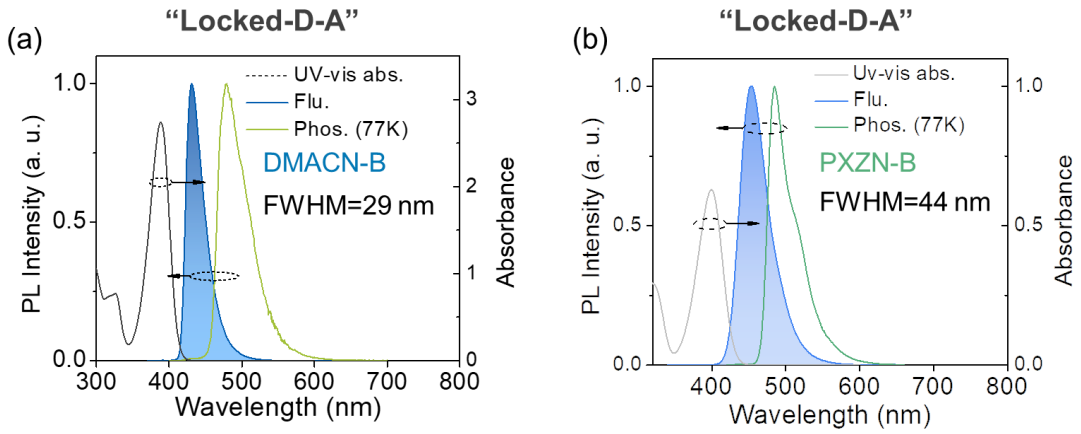

Figure 4-6. UV-vis absorption and PL spectra at room temperature and phosphorescence spectra at 77 K in toluene for (a) the locked DMACN-B and (b) the locked PXZN-B.

For further clarifying TADF properties, the transient PL properties of the compounds were measured in the thin films doped into a host matrix at 20 wt%. As shown in **Figure 4-7**, the delayed components in both blend films could be clearly observed from the transient PL curves, confirming the TADF properties of the locked DMACN-B and PXZN-B. Also, a large k_r of 2.5×10^8 and 1.9×10^8 s^{-1} could be maintained because of their high PLQYs and small radiative decay lifetime. The data of photophysical properties in blend film was summarized in **Table 4-1**.

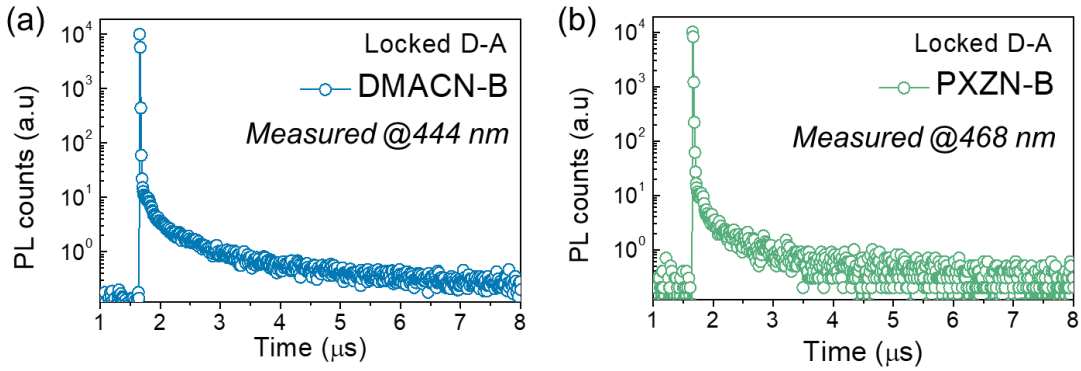

Figure 4-7. Transient emission profiles of (a) 20 wt% locked DMACN-B-doped DPEPO films and (b) 20 wt% locked PXZN-B -doped DPEPO films at room temperature.

Table 4-1. Photophysical properties of lock PXZN-B and DMACN-B.

Material	λ_{PL} (nm)	FWHM (nm)	PLQY (%)	τ_p (ns)	k_r (10^8 s^{-1})	ΔE_{ST} (eV)
Lock PXZN-B	430	44	92.0	5.4	1.9	0.28
Lock DMACN-B	454	29	93.0	4.0	2.5	0.27

4.2.5 ASE properties

As we have estimated earlier, because of the restriction of the D/A torsion angle by inserting the diphenyl methylene lock group, the corresponding D/A planes tended to be quasi-planar, which directly led to a larger spatial overlap between the LUMO and HOMO wavefunctions. Although the ΔE_{ST} became relatively larger, the TADF activity was still successfully triggered, which was discussed above. Moreover, another merit for the use of the intramolecular-lock method was to fasten the k_r (exceeding 10^8 s^{-1}) of the S_1 to S_0 transition [$k_r(S_1 \rightarrow S_0)$] of the locked DMACN-B and PXZN-B estimated. Therefore, we aimed at evaluating the ASE properties of the locked D-A type TADF emitters. **Figures 4-8 (a) and (b)** exhibited the spectral change of DMACN-B- and PXZN-B-based blend films with the optimal doping ratios in DPEPO and mCP

under different excitation intensities. Here, because of the better solubility for solution-processing, mCP with a high T_1 state was also used as the host. Noticeably, with a gradual increase in excitation intensity above the threshold, the sharp narrowing of the spectral band and a rapid increase of output intensity were observed from Figure 4-8 (a) and (b). In detail, for the optimized PXZN-B-based sample at 10 wt%, when increasing the excitation power from 1.09 to 20.96 μJ cm^{-2}, the corresponding FWHM largely decreased from 34.0 to 8.1 nm as shown in Figure 4-8 (a) and (c). Then, after plotting the output PL intensity against excitation intensity, a clear change of slope was observed, indicating that the low threshold was around 3.0 μJ cm^{-2}. A similar ASE performance occurred in deep-blue (around 448 nm) DMACN-B-based samples with the calculated threshold of around 12.0 μJ cm^{-2}. Moreover, to assess the optical gain of the TADF laser dyes, the σ_{em} has been estimated. According to the Eq. 2.1, the corresponding σ_{em} at the ASE peak for locked DMACN-B and PXZN-B is around 8.0×10^{-17} cm^2. The aforementioned performance of the locked D-A type TADF emitters implied the possibility and potential for realizing low threshold ASE or laser performance based on D-A type TADF molecules, by precisely manipulating the HOMO/LUMO overlap and torsion angles.

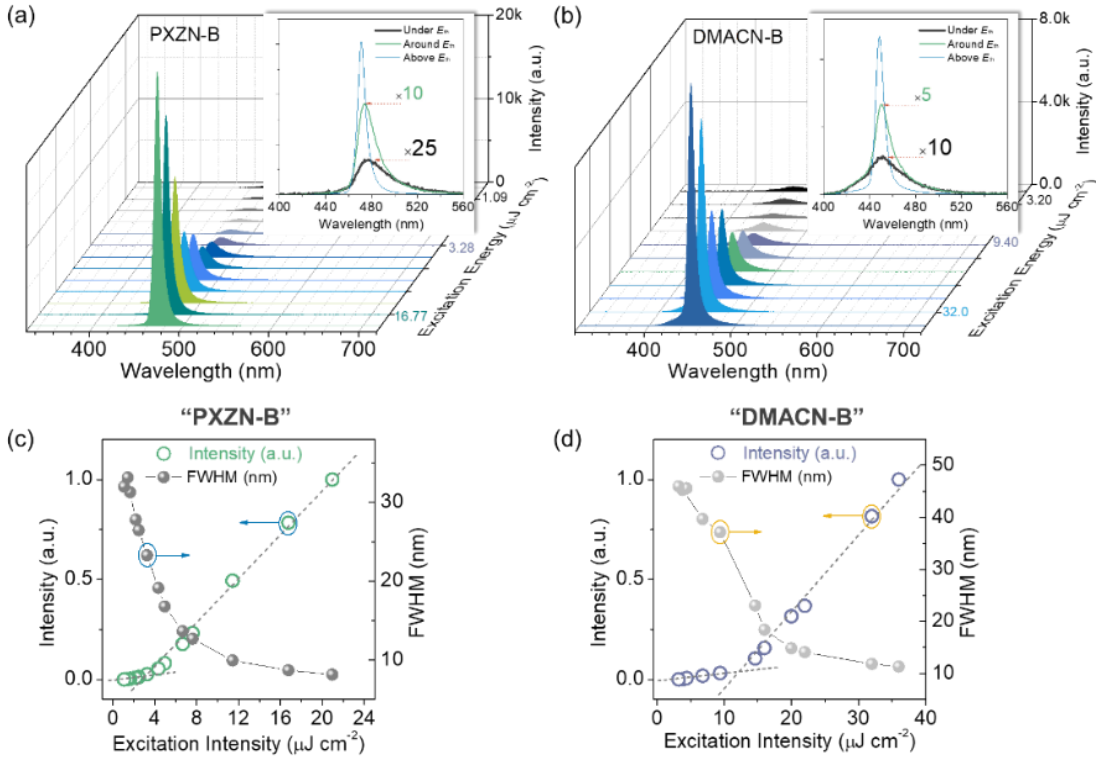

Figure 4-8. Optimal ASE performance of PXZN-B- and DMACN-B-based solid-state films in a mCP host matrix. Spectral shapes changed with increasing the excitation power for (a) PXZN-B and (b) DMACN-B doped films. The insets are the corresponding spectra before, around, and above the ASE threshold. Output waveguide emission intensity of FWHMs versus excitation power relationship of (c) PXZN-B and (d) DMACN-B doped films.

4.2.6 DFB lasers based on TADF molecules

The promising ASE properties of the intramolecular-locked TADF molecules prompted us to further investigate the corresponding lasing characteristics. I incorporated the 2nd-order DFB resonator structures to give a vertical output of the laser with lower thresholds. The thickness of PXZN-B-based films used for the DFB devices was around 200 nm. The laser devices were thereby optically pumped by a nitrogen laser source. As shown in **Figure 4-9 (a)**, the laser threshold was estimated to be 1.1 μJ cm^{-2} according to the abrupt change of slope intensity and FWHM, which was lower than the ASE threshold (3.3 μJ cm^{-2}). Moreover, the FWHM of laser devices was

detected to be as small as 0.2 nm [Figure 4-9 (b)]. Remarkably, the laser threshold from the PXZN-B TADF molecules was comparable to the state-of-the-art solution-processed fluorescence rivals.

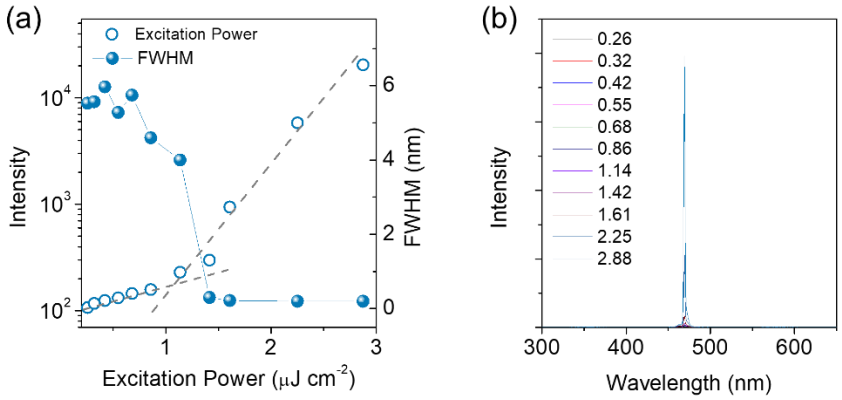

Figure 4-9. 2nd order DFB lasers based on a locked PXZN-B: mCP blend film were demonstrated. (a) Output waveguide emission intensity or FWHM versus excitation power relationship of PXZN-B based laser devices. (b) Spectral shape change with increasing the excitation power for DMACN-B based laser devices. The inset is the corresponding spectra of the laser with high resolution.

Then, the polarization properties of a pure blue laser based on the locked PXZNB: mCP blend film were investigated. As shown in **Figure 4-10**, the 2nd-order DFB laser exhibited a strong, linear transverse electric polarization. Consequently, the approaching unity degree value implied that the remarkable polarization characteristics of the pure blue laser system.

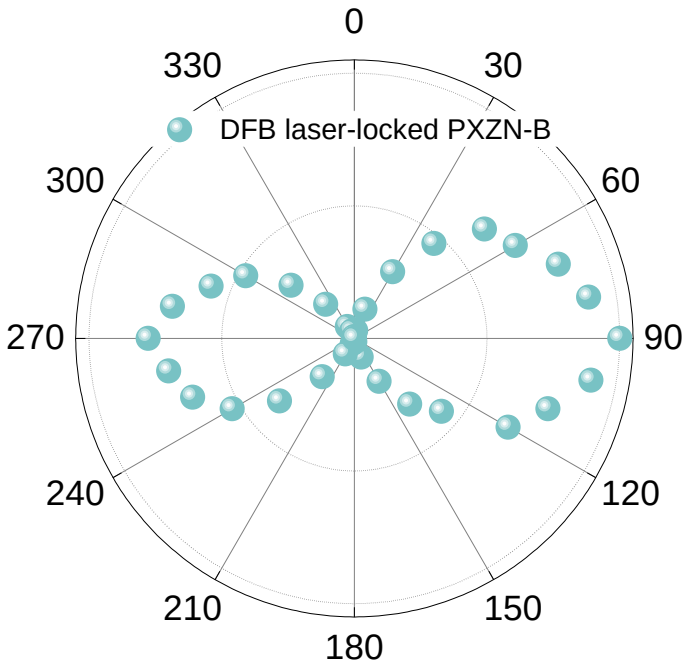

Figure 4-10. Polarization of the laser based on the locked PXZN-B in mCP blend film.

4.2.7 EL properties

To further verify the TADF properties and EL performance of PXZN-B and DMACN-B, pure-blue and deep-blue OLEDs were fabricated accordingly. The device structure was glass substrate/ITO/1,4,5,8,9,11-hexaazatriphenylenehexacarbonitrile (HAT-CN, HIL) (10 nm)/1,1-bis[(di-4-tolylamino)phenyl]cyclohexane (TAPC, HTL) (30 nm)/4,4',4''-tris-(carbazol-9-yl)-triphenylamine (TCTA, EBL) (10 nm)/1,3-di(9H-carbazol-9-yl)benzene (mCP, EBL) (10 nm)/DPEPO: dopant (EML, *x* wt%, 20 nm)/DPEPO (HBL, 10 nm)/1,3,5-tri[(3-pyridyl)-phen-3-yl]benzene (TmPyPB, ETL) (30 nm)/8-hydroxyquinolinolato-lithium (Liq, EIL) (2 nm)/Al (120 nm). The energy-level diagram of the devices is shown in **Figure 4-11 (a)**. Consequently, the OLED with 20 wt% PXZN-B (Device 1) exhibited a maximum EQE (EQE_{max}) of 12.7% and a maximum PE (PE_{max}) of 15.3 lm W^{-1}, with CIE coordinates of (0.133, 0.147) at 5 mA cm^{-2}. For optimized DMACN-B based OLEDs, the EQE_{max} and PE_{max} were 10.0% and 4.5 lm W^{-1}, respectively. In particular, the corresponding CIE coordinates were (0.151,

0.045) with a small FWHM of 44 nm, which could closely satisfy the Rec.2020 (0.131, 0.046) standard. The corresponding data was summarized in **Table 4-2**.

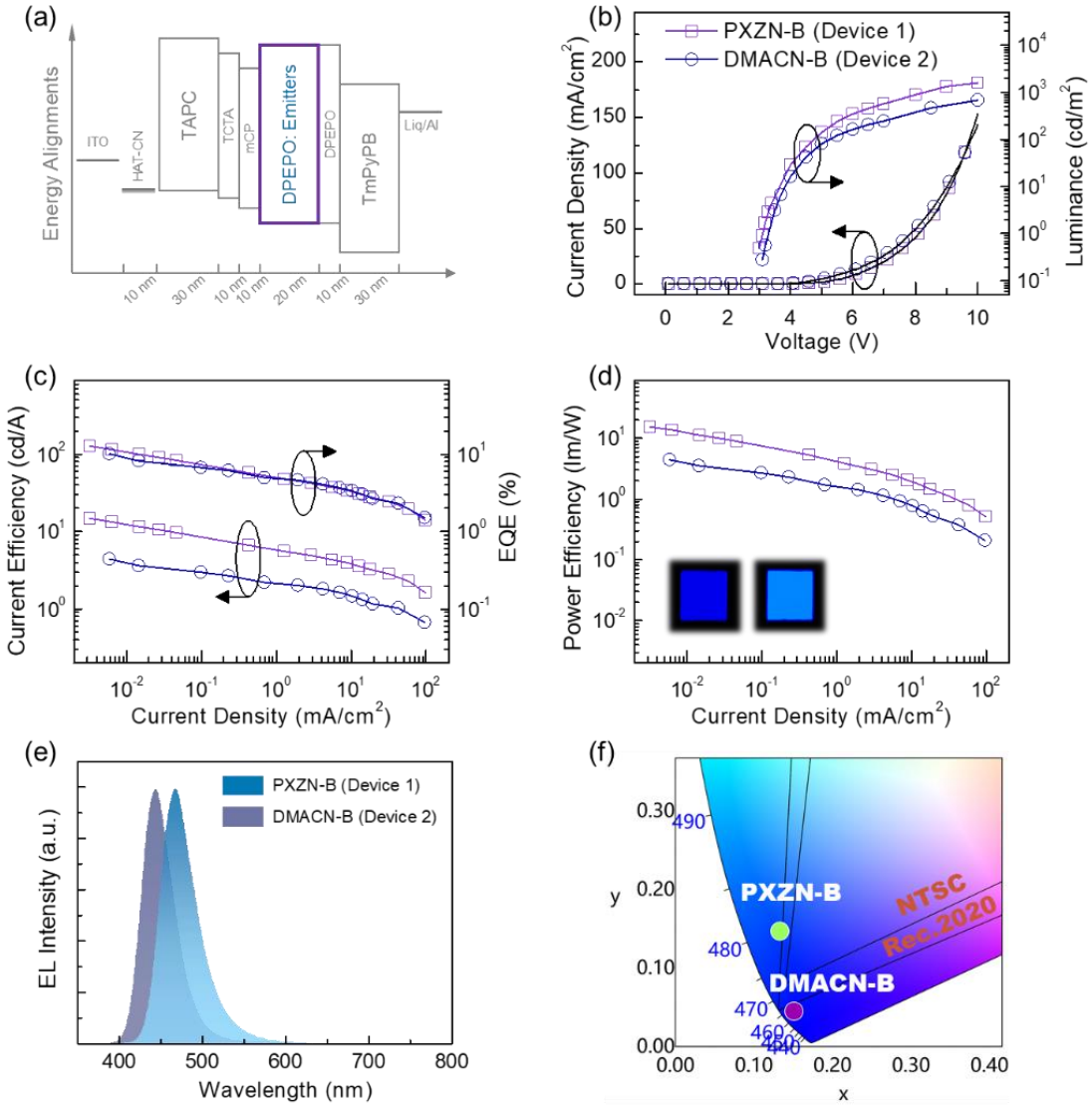

Figure 4-11. (a) Schematic energy-level diagram, (b) current density–voltage–luminance (*J*–*V*–*L*), (c) current efficiency–current density–external quantum efficiency (CE–*J*–EQE), (d) power efficiency–current density (PE–*J*) characteristics; (e) EL spectra (at a current density of 5 mA cm^{-2}), and (f) CIE plots of OLEDs.

Table 4-2. The performance of OLED devices and ASE based on PXZN-B and DMACN-B.

Devices		Vona)	$\eta_{max/50/500}$ b)	λmax	@ 5 mA cm^{-2}		ASE Threshold
Dopant	Host	[V]	EQE [%]		FWHM [nm]	CIE (x, y)	[μJ cm^{-2}]
PXZN-B	DPEPO	3.1	12.7/5.3/3.0	468	48	(0.133, 0.147)	3.3
DMACN-B	DPEPO	3.3	10.0/4.6/2.2	444	44	(0.151, 0.045)	12.0

a) The driving voltages at 1 cd m^{-2}. b) The maximum efficiencies and efficiencies at 50 and 500 cd m^{-2}.

Moreover, to evaluate the EL performance and the color purity in this work, the representative devices in the deep-blue region were systematically summarized in **Figure 4-12**. It was evident from Figure 4-12 (a) that the device performance based on DMACN-B in this work reached the record high EQE of over 10% among the ultra-blue OLEDs with CIE-y<0.046. Meanwhile, benefitting from the narrowband EL spectra induced by the rigid molecular skeleton, the color purity was much reinforced with a smaller emission blueshift in Figure 4-12 (b).

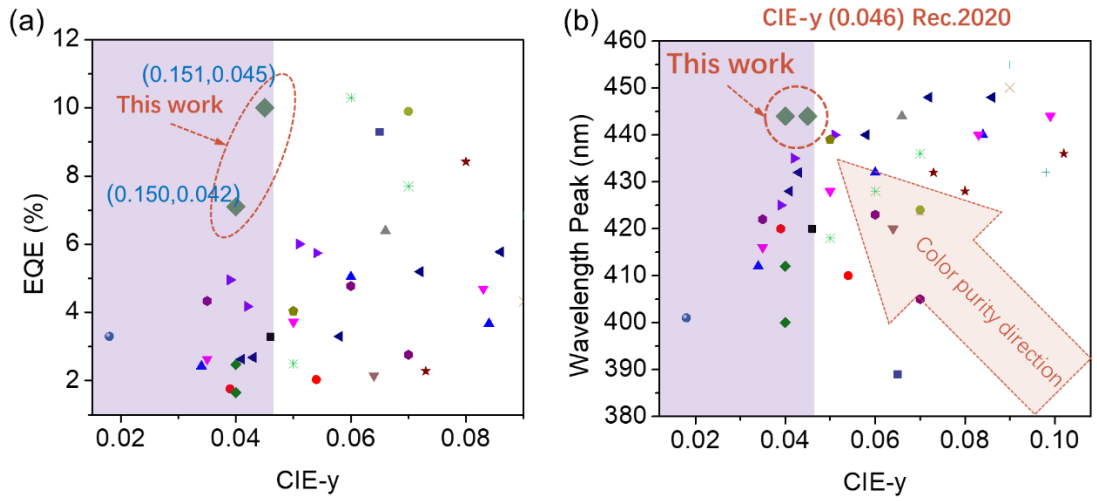

Figure 4-12. (a) The comparison of the representative deep EL performance having small CIE-y coordinate with the device performance presented in this work. (b)

Wavelength peak versus CIE-y coordinate plots that evaluated the color purity of the EL in the reported works and this work.

4.3 Conclusion

In summary, we proposed that the unconventional quasi-planar D-A structure would be very suitable for achieving deep-blue or even violet-blue emission, which was quite challenging in traditional *twisted* D-A TADF design. In this regard, I designed two TADF emitters, locked PXZN-B and DMACN-B, into which diphenyl methylene intramolecular-lock was incorporated to manipulate the HOMO/LUMO distribution by shrinking the torsion angles, restricting the intramolecular rotation and vibration. As a consequence, the rigid and quasi-planar TADF molecules, PXZN-B and DMACN-B, exhibited remarkably blue-shifted structureless emission with small FWHM values of 44 and 29 nm, respectively. Furthermore, for the EL performance, better CIE-y coordinates for PXZN-B (0.133, 0.147) and DMACN-B (0.151, 0.045) were obtained, owing to the small FWHMs, as well as the structureless spectral shape. To the best of our knowledge, this was the first time for TADF emitters that could closely approach Rec.2020 blue standard (0.131, 0.046). Moreover, OLEDs exhibited TADF characteristics, with EQEs exceeding 10% for PXZN-B (12.7%) and DMACN-B (10.0%). Furthermore, because of the enhanced f, the S_1-to-S_0 k_r could exceed 10^8 s^{-1}; thus, such (locked D-A) type TADF emitters could also exhibit good laser performance, with a low threshold of 1.1 μJ cm^{-2}. Therefore, the intramolecular-lock strategy provided not only innovation for realizing high-efficiency deep-blue TADF emission with small FWHMs and high color purity but also an avenue for torching TADF-based ASE and lasers by rationally controlling the HOMO/LUMO distribution and torsion angles.

4.4 Experimental sections

Materials and characterization

All chemicals and starting materials were received from commercial sources and used without further purification. ^{1}H NMR and ^{13}C NMR spectra were recorded on a Bruker 400 spectrometer at room temperature. Mass spectra were recorded on a Thermo ISQ mass spectrometer using a direct exposure probe. UV–vis absorption spectra were recorded on a Perkin Elmer Lambda 750 spectrophotometer. PL spectra and phosphorescent spectra were recorded on a Hitachi F-4600 fluorescence spectrophotometer. PLQYs were estimated using an integrating sphere system coupled with a photonic multichannel analyzer (Hamamatsu Photonics C11347-11, PMA-11, Japan), and all the samples were excited at 340 nm. Transient PL decays were measured by using a Quantaurus-Tau fluorescence lifetime measurement system (C11367-03, Hamamatsu Photonics, Japan) and a single photon counting spectrometer from HORIBA Jobin Yvon. Electrochemical measurements were made by using a CHI600 voltammetric analyzer. A conventional three-electrode configuration consisting of a platinum working electrode, a Pt-wire counter electrode, and an Ag/AgCl reference electrode was used. The solvent in all measurements was CH_2Cl_2, and the supporting electrolyte was 0.1 m $[Bu_4N]PF_6$. Ferrocene was added as a calibrant after each set of measurements, and all potentials reported were quoted with reference to the ferrocene-ferrocenium (Fc/Fc^+) couple at a scan rate of 100 mV s^{-1}.

Synthesis route

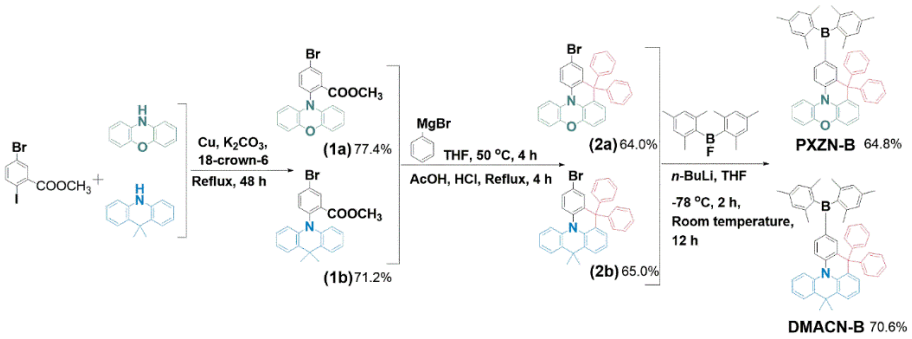

Figure 4-13. Synthetic routes for locked PXZN-B and DMACN-B.

Synthesis of methyl 5-bromo-2-(10H-phenoxazin-10-yl)benzoate (1a)

Methyl 5-bromo-2-iodobenzoate (5.0 g, 15 mmol), 10H-phenoxazine (3.22 g, 17.6 mmol), copper powder (0.13 g, 2.20 mmol), 18-crown-6 (0.38 g, 1.47 mmol), and potassium carbonate (2.43 g, 17.60 mmol) was dissolved in 100 mL 1,2-dichlorobenzene in a 500 mL 2-neck round bottom flask under argon atmosphere. The reaction mixture was refluxed for 48 hours under stirring, the reaction was cooled to room temperature and then the solvent was removed through rotary evaporator. The solid products dissolved in DCM and washed with water (200 mL×3). Then the extracts were combined, dried with sodium sulfate (Na_2SO_4), filtered and evaporated under reduced pressure. The crude product was purified by column chromatography using petroleum ether (PE)/DCM (7/3, v/v) as eluent to attain product. The obtained product was a yellow powder (4.50 g, 77.40%). ^{1}H NMR (400 MHz, $CDCl_3$): δ (ppm): 8.31 (d, J=2.4 Hz, 1H), 7.89 (dd, J=8.4, 2.4 Hz, 1H), 7.31 (t, J=6.7 Hz, 1H), 6.80−6.51 (m, 6H), 5.82 (dt, J=7.9, 1.8 Hz, 2H), 3.74 (d, J=2.9 Hz, 3H). ^{13}C NMR (100 MHz, $CDCl_3$) δ (ppm): 164.42, 143.78, 142.06, 138.15, 137.79, 135.13, 133.66, 133.45, 123.23, 122.57, 121.58, 115.58, 112.85, 77.35, 77.03, 76.72, 52.81. MS (EI) m/z: 395.00 [M^+]. Elemental analysis: found (%): C, 60.74; H, 3.51; N, 3.69. Calcd. for $C_{20}H_{14}BrNO_3$: C, 60.62; H, 3.56; N, 3.53.

Synthesis of methyl 5-bromo-2-(9,9-dimethylacridin-10(9H)-yl)benzoate (1b)

The compound methyl 5-bromo-2-iodobenzoate (5.10 g, 15 mmol), 9,9-dimethyl-9,10-dihydroacridine (3.76 g, 18 mmol), copper powder (0.14 g, 2.24 mmol), 18-crown-6 (0.39 g, 1.55 mmol) and potassium carbonate (2.53 g, 18 mmol) were dissolved in 150 mL 1,2-dichlorobenzene in a 500 mL 2-neck round bottom flask under argon atmosphere. The reaction mixture was refluxed for 48 hours with continuously stirring, then cooled to room temperature and solvent was removed under reduced pressure. The obtained products dissolved in DCM and washed with water (200 mL×3). The separated organic layer was combined, dried with Na_2SO_4 and evaporated through rotary evaporator. The crude mixture was subjected to column chromatography using

PE/DCM (7/3, v/v) as an eluent to obtain the product, which was a pale yellow powder (4.50 g, 71.20%). ^{1}H NMR (400 MHz, $CDCl_3$): δ (ppm): 8.34 (d, J=2.4 Hz, 1H), 7.92 (dd, J=8.4, 2.4 Hz, 1H), 7.53−7.44 (m, 2H), 7.26 (d, J=8.4 Hz, 1H), 6.95 (dd, J=7.2, 1.6 Hz, 4H), 6.12−6.04 (m, 2H), 3.58 (d, J=2.7 Hz, 3H), 1.73 (s, 6H). ^{13}C NMR (100 MHz, $CDCl_3$) δ (ppm): 164.53, 143.70, 141.72, 140.53, 140.16, 139.81, 137.74, 135.83, 135.40, 135.26, 134.29, 134.10, 129.71, 126.45, 125.77, 122.26, 120.65, 113.39, 77.35, 77.03, 76.71, 52.61, 35.86. MS (EI) m/z: 421.03 [M^+]. Elemental analysis: found (%): C, 66.60; H, 4.51; N, 3.59. Calcd. for $C_{23}H_{20}BrNO_2$: C, 65.41; H, 4.77; N, 3.32.

Synthesis of 11-bromo-9,9-diphenyl-9H-quinolino[3,2,1-kl]phenoxazine (2a)

The phenyl magnesium bromide (1 M solution in THF, 54 mL, 54.26 mmol) was taken and added to the flask under argon and stirred at room temperature. The THF solution of methyl 5-bromo-2-(10H-phenoxazin-10-yl)benzoate (4.30 g, 10.80 mmol) was added slowly to the reaction mixture. Further stirred at 50 ℃ for 4 hours, then the reaction mixture was quenched with a small amount of ammonium hydroxide (NH_4Cl) in water (8 mL) and THF was evaporated. The obtained solid was extracted with DCM and washed with water (3×50 mL). The organic layer was collected and dried over Na_2SO_4, resulting in 3.90 g yellowish viscous solid, which was used in the next reaction without column purification. The crude mixture was dissolved in 30 mL acetic acid while 8 mL hydrochloric acid (36%) was added drop-wise to the solution mixture. The reaction mixture was refluxed for 4 hours, then cooled to room temperature, extracted with DCM and water the organic layer was evaporated. which was further purified from column chromatography with eluents: PE/DCM as a white powder (7/2, v/v) (3.50 g, 64.0%). ^{1}H NMR (400 MHz, $CDCl_3$): δ (ppm): 7.54 (d, J=8.6 Hz, 1H), 7.36 (d, J=8.7 Hz, 4H), 7.17 (t, J=11.9 Hz, 3H), 6.97 (d, J=2.2 Hz, 3H), 6.94−6.84 (m, 7H), 6.81 (d, J=8.0 Hz, 1H), 6.48 (d, J=9.2 Hz, 1H). ^{13}C NMR (100 MHz, $CDCl_3$) δ (ppm): 147.88, 145.82, 144.40, 143.91, 137.61, 136.28, 133.03, 132.26, 131.34, 129.77, 128.92, 128.83, 127.93, 127.13, 126.62, 124.22, 124.07, 123.32, 122.86, 118.03, 117.28, 115.28, 114.35, 113.79, 77.34, 77.22, 77.02, 76.70, 56.92. MS (EI) m/z: 501.04. Elemental

analysis: found (%): C, 74.28; H, 3.90; N, 2.89. Calcd. for $C_{31}H_{20}BrNO$: C, 74.11; H, 4.01; N, 2.79.

Synthesis of 3-bromo-9,9-dimethyl-5,5-diphenyl-5,9-dihydroquinolino[3,2,1 de]acridine (2b)

The phenyl magnesium bromide (1 M solution in THF 51 mL, 50.91 mmol) was taken and added to the flask under argon and stirred at room temperature. The THF solution of methyl 5-bromo-2-(9,9-dimethylacridin-10(9H)-yl)benzoate (4.30 g, 10.22 mmol) was added slowly to the reaction mixture. Further stirred at 50℃ for 4 hours, then the reaction mixture was quenched with small amount of NH_4Cl in water (8 mL) and THF was evaporated. The obtained solid was extracted with DCM and washed with water (3×50 mL). The organic layer was collected and dried over Na_2SO_4, resulting in 3.90 g yellowish viscous solid, which was used in the next reaction without column purification. The crude mixture was dissolved in 30 mL acetic acid while 8 mL hydrochloric acid (36%) was added drop-wise to the solution mixture. The reaction mixture was refluxed for 4 hours, then cooled to room temperature, extracted with DCM and water. which was further purified from column chromatography with eluents: PE/DCM as a white powder (7/2, v/v) (3.50 g, 65.0%). ^{1}H NMR (400 MHz, $CDCl_3$): δ (ppm): 7.45 (d, J=6.4 Hz, 1H), 7.36 (dd, J=7.2, 5.1 Hz, 6H), 7.13−6.94 (m, 10H), 6.79 (t, J=7.6 Hz, 3H), 1.93 (s, 3H), 1.28 (s, 3H). ^{13}C NMR (100 MHz, $CDCl_3$) δ (ppm): 144.87, 144.80, 138.95, 137.80, 137.63, 136.68, 136.13, 133.48, 132.63, 132.54, 131.51, 129.85, 128.92, 127.83, 127.75, 127.26, 126.99, 126.38, 126.21, 124.09, 123.34, 122.31, 121.97, 118.35, 117.72, 114.59, 77.35, 77.23, 77.03, 76.71, 57.29, 36.73, 33.08, 22.88. MS (EI) m/z: 527.10 [M^+]. Elemental analysis: found (%): C, 77.39; H, 4.77; N, 2.69. Calcd. for $C_{34}H_{26}BrN$: C, 77.27; H, 4.96; N, 2.65.

Synthesis of 11-(dimesitylboranyl)-9,9-diphenyl-9H-quinolino[3,2,1kl]phenoxazine (PXZN-B)

Compound 2a (1.50 g, 2.99 mmol) was dissolved in 30 mL distilled THF and cooled to −78 ℃. After 10 minutes, *n*-butyl lithium (1.6 M solution in hexane, 2.21 mL,

3.61 mmol) was added drop-wise. The mixture was stirred for 1 hour at −78 °C, and then dimesitylboron fluoride (2.0 g, 7.51 mmol) in 30 mL THF was dissolved and added slowly to the reaction mixture. After 2 hours, the reaction mixture was slowly allowed to warm up to room temperature and stirred for 12 hours. On completion, the reaction mixture was quenched with water (5 mL). The solvent was evaporated and the residue was dissolved in DCM and washed well with water (3×50 mL). The organic layer was dried over Na_2SO_4, filtered and evaporated, which was purified from column chromatography using PE/DCM (6/4, v/v) as eluent and final product was obtained as yellowish powder (1.30 g, 64.80%).^{1}H NMR (600 MHz, $CDCl_3$): δ (ppm): 7.55 (d, J = 8.3 Hz, 1H), 7.39 (d, J=8.3 Hz, 1H), 7.15–7.06 (m, 7H), 6.92–6.80 (m, 8H), 6.78 (d, J=7.9 Hz, 1H), 6.70 (d, J= 3.1 Hz, 5H), 6.61 (d, J=7.9 Hz, 1H), 2.25 (s, 6H), 1.98 (s, 12H).^{13}C NMR (151 MHz, $CDCl_3$) δ (ppm): 147.95, 145.79, 144.81, 144.54, 141.56, 141.30, 140.40, 140.31, 139.39, 137.83, 136.02, 132.74, 130.95, 128.87, 128.63, 127.90, 127.77, 127.38, 126.28, 124.42, 124.06, 123.18, 122.97, 118.63, 117.21, 113.67, 112.73, 77.20, 76.99, 76.78, 56.65, 23.38, 21.13. MALDI-TOF (m/z) calculated for $C_{49}H_{42}BNO$ [M^+]: 697.691, found: 671.640. Elemental analysis: found (%): C, 87.78; H, 6.32; N, 2.30. Calcd. for $C_{49}H_{42}BNO$: C, 87.62; H, 6.30; N, 2.09.

Synthesis of N,N-dimesityl-9,9-dimethyl-5,5-diphenyl-5,9-dihydroquinolino[3,2,1-de]acridin-3-amine (DMACN-B)

Compound 2b (1.51 g, 2.84 mmol) was dissolved in 30 mL distilled THF and cooled to −78 °C. After 10 minutes, *n*-butyl lithium (1.6 M solution in hexane 2.11 mL, 3.41 mmol) was added drop-wise. The mixture was stirred for 1 hour at −78 °C, and then dimesitylboron fluoride (1.51 g, 5.61 mmol) in 30 mL THF was dissolved and added slowly to the reaction mixture. After 2 hours, the reaction mixture was slowly allowed to warm up to room temperature and stirred for 12 hours. On completion, the reaction mixture was quenched with water (5 mL). The solvent was evaporated and the residue was dissolved in DCM and washed well with water (3×50 mL). The organic layer was dried over Na_2SO_4 filtered and evaporated, which was purified from column chromatography using PE/DCM (6/4, v/v) as eluent and final product was obtained as

white powder (1.40 g, 70.60%). ^{1}H NMR (600 MHz, $CDCl_3$): δ (ppm): 7.42 (d, J = 6.3 Hz, 1H), 7.39 (s, 2H), 7.35 (d, J=7.7 Hz, 1H), 7.13 (s, 3H), 7.10–6.98 (m, 8H), 6.90 (d, J=7.7 Hz, 2H), 6.82 (s, 1H), 6.76 (d, J=8.2 Hz, 2H), 6.71 (s, 4H), 2.26 (s, 6H), 2.01 (s, 12H), 1.89 (s, 3H), 1.28 (s, 3H). ^{13}C NMR (150 MHz, CDCl3) δ (ppm) 145.67, 145.65, 145.46, 145.23, 142.67, 141.68, 140.36, 139.98, 139.35, 137.80, 136.85, 136.09, 136.01, 134.11, 133.49, 133.09, 131.14, 128.85, 127.90, 127.56, 127.29, 127.22, 126.12, 126.10, 126.05, 123.99, 123.50, 122.37, 121.79, 118.29, 115.80, 77.21, 76.99, 76.78, 57.00, 36.70, 33.12, 23.43, 22.96, 21.14. MALDI-TOF (m/z) calculated for $C_{52}H_{48}BN$ [M^+]: 697.773, found: 697.519. Elemental analysis: found (%): C, 89.77; H, 6.81; N, 1.94. Calcd. for $C_{52}H_{48}BN$: C, 89.51; H, 6.93; N, 2.01.

Device fabrication

OLEDs were fabricated on ITO-coated glass substrates layer (110 nm, 15 Ω square^{-1}) under a base pressure of 3 × 10^{-6} Torr. Deposition rates and thicknesses of all materials were monitored with oscillating quartz crystals. The doping layer was deposited by utilizing two different sensors to monitor the deposition rates of both host material and dopant material. The deposition rate of the host was controlled at 0.2 nm s^{-1}. The EL and *J-V* characteristics of the devices were measured by a constant current source (Keithley 2400 Source Meter) combined with a photometer (Photo Research Spectra Scan PR 655) under an ambient environment.

Single crystal information

Data collections were performed on a Bruker D8-Venture diffractometer with a Turbo X-ray Source (Mo–Kα radiation, λ = 0.71073 Å). The crystal was kept at 100.0 K during data collection. Using Olex2, the structure was solved with the XT structure solution program using Intrinsic Phasing and refined with the ShelXL refinement package using Least Squares minimization.

ASE/laser sample preparation and measurement

Film samples were fabricated through the solution process. For this, dye emitters and host materials (mCP, mCBP or DPEPO) were dissolved in chloroform with corresponding weight doping ratios. Non-fluorescent glass substrates for optical measurement were selected, which were subsequently cleaned with acetone, isopropyl alcohol, and UV-ozone treatment before spin-coating. The film thickness was controlled around 200 nm by tuning the spin-coating rotation speed. The prepared substrates were cut from the center for better waveguide emission output, then photoexcited by a commercial nitrogen (N_2) laser (the excitation wavelength is 337 nm, the pulse width is 0.8 ns, and the repetition rate is 8 Hz, KEN2020, Usho Optical Systems Co. Ltd) in the ambient condition. The neutral density (ND) filter was set up between the N_2 laser source and the sample to adjust the input power intensity. Output waveguide emission from the cutting edge of samples was detected by an optical fiber connected to spectrometers (Hamamatsu Photonics PMA-12 and PMA-50).

References

[1] M. A. Baldo, D. F. O'Brien, Y. You, A. Shoustikov, S. Sibley, M. E. Thompson, S. R. Forrest, *Nature* **1998**, *395*, 151.

[2] J. Kido, M. Kimura, K. Nagai, *Science* **1995**, *267*, 1332.

[3] X. Ai, E. W. Evans, S. Dong, A. J. Gillett, H. Guo, Y. Chen, T. J. H. Hele, R. H. Friend, F. Li, *Nature* **2018**, *563*, 536.

[4] S. Reineke, F. Lindner, G. Schwartz, N. Seidler, K. Walzer, B. Lüssem, K. Leo, *Nature* **2009**, *459*, 234.

[5] D. Di, S. Romanov Alexander, L. Yang, M. Richter Johannes, P. H. Rivett Jasmine, S. Jones, H. Thomas Tudor, M. Abdi Jalebi, H. Friend Richard, M. Linnolahti, M. Bochmann, D. Credgington, *Science* **2017**, *356*, 159.

[6] I. D. W. Samuel, G. A. Turnbull, *Chem. Rev.* **2007**, *107*, 1272.

[7] H. Nakanotani, T. Furukawa, C. Adachi, *Adv. Opt. Mater.* **2015**, *3*, 1381.

[8] A. J. Kuehne, M. C. Gather, *Chem. Rev.* **2016**, *116*, 12823.

[9] X.-K. Chen, D. Kim, J.-L. Brédas, *Acc. Chem. Res.* **2018**, *51*, 2215.

[10] Y. Liu, C. Li, Z. Ren, S. Yan, M. R. Bryce, *Nat. Rev. Mater.* **2018**, *3*, 18020.

[11] S. Li, Z. Yu, X. Xiao, H. Geng, K. Wang, X. Jin, Q. Liao, Y. Liao, Y. Wu, J. Yao, H. Fu, *Laser Photon. Rev.* **2019**, *13*, 1900036.

[12] A. S. D. Sandanayaka, T. Matsushima, F. Bencheikh, S. Terakawa, W. J. Potscavage, C. Qin, T. Fujihara, K. Goushi, J.-C. Ribierre, C. Adachi, *Appl. Phys. Express* **2019**, *12*, 061010.

[13] D.-H. Kim, A. D'Aléo, X.-K. Chen, A. D. S. Sandanayaka, D. Yao, L. Zhao, T. Komino, E. Zaborova, G. Canard, Y. Tsuchiya, E. Choi, J. W. Wu, F. Fages, J.-L. Brédas, J.-C. Ribierre, C. Adachi, *Nat. Photon.* **2018**, *12*, 98.

[14] H. Ye, D. H. Kim, X. Chen, A. S. D. Sandanayaka, J. U. Kim, E. Zaborova, G. Canard, Y. Tsuchiya, E. Y. Choi, J. W. Wu, F. Fages, J.-L. Bredas, A. D'Aléo, J.-C. Ribierre, C. Adachi, *Chem. Mater.* **2018**, *30*, 6702.

[15] Y. Jiang, Y.-Y. Liu, X. Liu, H. Lin, K. Gao, W.-Y. Lai, W. Huang, *Chem. Soc. Rev.* **2020**, *49*, 5885.

[16] Z. Zhou, C. Qiao, K. Wang, L. Wang, J. Liang, Q. Peng, Z. Wei, H. Dong, C. Zhang, Z. Shuai, Y. Yan, Y. S. Zhao, *Angew. Chem. Int. Ed.* **2020**, *59*, 21677.

[17] M. A. El-Sayed, *Accounts Chem. Res.* **1968**, *1*, 8.

[18] H. Uoyama, K. Goushi, K. Shizu, H. Nomura, C. Adachi, *Nature* **2012**, *492*, 234.

[19] Q. Zhang, B. Li, S. Huang, H. Nomura, H. Tanaka, C. Adachi, *Nat. Photon.* **2014**, *8*, 326.

[20] S. Hirata, Y. Sakai, K. Masui, H. Tanaka, S. Y. Lee, H. Nomura, N. Nakamura, M. Yasumatsu, H. Nakanotani, Q. Zhang, K. Shizu, H. Miyazaki, C. Adachi, *Nat. Mater.* **2015**, *14*, 330.

[21] H. Kaji, H. Suzuki, T. Fukushima, K. Shizu, K. Suzuki, S. Kubo, T. Komino, H. Oiwa, F. Suzuki, A. Wakamiya, Y. Murata, C. Adachi, *Nat. Commun.* **2015**, *6*, 8476.

[22] M. Y. Wong, E. Zysman-Colman, *Adv. Mater.* **2017**, *29*, 1605444.

[23] L.-S. Cui, A. J. Gillett, S.-F. Zhang, H. Ye, Y. Liu, X.-K. Chen, Z.-S. Lin, E. W. Evans, W. K. Myers, T. K. Ronson, H. Nakanotani, S. Reineke, J.-L. Bredas, C. Adachi, R. H. Friend, *Nat. Photon.* **2020**, *14*, 636.

[24] X. Tang, L.-S. Cui, H.-C. Li, A. J. Gillett, F. Auras, Y.-K. Qu, C. Zhong, S. T. E. Jones, Z.-Q. Jiang, R. H. Friend, L.-S. Liao, *Nat. Mater.* **2020**, *19*, 1332.

[25] Y. Wada, H. Nakagawa, S. Matsumoto, Y. Wakisaka, H. Kaji, *Nat. Photon.* **2020**, *14*, 643.

[26] Z. Yang, Z. Mao, Z. Xie, Y. Zhang, S. Liu, J. Zhao, J. Xu, Z. Chi, M. P. Aldred, *Chem. Soc. Rev.* **2017**, *46*, 915.

[27] H. Tanaka, K. Shizu, H. Miyazaki, C. Adachi, *Chem. Commun.* **2012**, *48*, 11392.

[28] X. Cai, S.-J. Su, *Adv. Funct. Mater.* **2018**, *28*, 1802558.

[29] W. Yuan, H. Yang, C. Duan, X. Cao, J. Zhang, H. Xu, N. Sun, Y. Tao, W. Huang, *Chem* **2020**, *6*, 1998.

[30] P. Rajamalli, N. Senthilkumar, P. Y. Huang, C. C. Ren-Wu, H. W. Lin, C. H. Cheng, *J. Am. Chem. Soc.* **2017**, *139*, 10948.

[31] H. Tsujimoto, D.-G. Ha, G. Markopoulos, H. S. Chae, M. A. Baldo, T. M.

Swager, *J. Am. Chem. Soc.* **2017**, *139*, 4894.

[32] D. G. Congrave, B. H. Drummond, P. J. Conaghan, H. Francis, S. T. E. Jones, C. P. Grey, N. C. Greenham, D. Credgington, H. Bronstein, *J. Am. Chem. Soc.* **2019**, *141*, 18390.

[33] Y. Im, M. Kim, Y. J. Cho, J.-A. Seo, K. S. Yook, J. Y. Lee, *Chem. Mater.* **2017**, *29*, 1946.

[34] T. Hatakeyama, K. Shiren, K. Nakajima, S. Nomura, S. Nakatsuka, K. Kinoshita, J. Ni, Y. Ono, T. Ikuta, *Adv. Mater.* **2016**, *28*, 2777.

[35] W. Zeng, H.-Y. Lai, W.-K. Lee, M. Jiao, Y.-J. Shiu, C. Zhong, S. Gong, T. Zhou, G. Xie, M. Sarma, K.-T. Wong, C.-C. Wu, C. Yang, *Adv. Mater.* **2018**, *30*, 1704961.

[36] J. Xue, Q. Liang, R. Wang, J. Hou, W. Li, Q. Peng, Z. Shuai, J. Qiao, *Adv. Mater.* **2019**, *31*, 1808242.

[37] M. Sugawara, S. Choi, D. Wood, *IEEE Signal Processing Magazine* **2014**, *31*, 170.

[38] J. E. O. Neal, H. Arnold, *SMPTE Motion Imaging Journal* **2016**, *125*, 116.

[39] Y. Yuan, X. Tang, X.-Y. Du, Y. Hu, Y.-J. Yu, Z.-Q. Jiang, L.-S. Liao, S.-T. Lee, *Adv. Opt. Mater.* **2019**, *7*, 1801536.

Chapter 5. Planar fused-structure with multiple-resonance (MR) effect toward narrowband emission and TADF lasers

5.1 Introduction

As I discussed in Chapter 4, the intramolecular lock used in the conventional twisted donor/acceptor structure could minimize the torsion angles between the donor and acceptor motifs, which resulted in a closer distance of the HOMO/LUMO wavefunctions located at electron-donating/accepting fragments, respectively.[1-10] Therefore, the quasi-planar molecular skeleton with much enhanced rigidity not only triggered laser activities but also maintained the TADF properties with a narrower emission.[11] Herein, to further suppress the vibronic coupling and structural relaxation for sharper emission and improve the laser performance, an entirely planar TADF molecule was proposed to reinforce the structural rigidity.[12-16] According to the equation 1.10:[17, 18]

$$\Delta E_{S1T1} = \frac{e^2}{2\pi\varepsilon_0} \iint \varphi_H(\overrightarrow{r_1})\varphi_L(\overrightarrow{r_2}) \frac{1}{|\overrightarrow{r_1}-\overrightarrow{r_2}|} \varphi_H(\overrightarrow{r_2})\, \varphi_L(\overrightarrow{r_1}) d^3\overrightarrow{r_1} d^3\overrightarrow{r_2}, \text{ (Eq. 1.10)}$$

where ΔE_{S1-T1} is the ΔE_{ST}, φ_H and φ_L represent the wavefunctions of the HOMO and LUMO, respectively, and r_{12} denotes the distance between the electrons 1 and 2. Therefore, it is evident that the ΔE_{ST} can be reduced by eliminating the overlap between HOMO and LUMO wavefunctions.[19] In this polycyclic aromatic framework, separated D/A motifs are replaced by nitrogen/boron atoms, respectively, where the HOMO wavefunctions would localize at the nitrogen atoms, while LUMO wavefunctions would locate at the boron atoms at the *para*-position.[20-22] Resultantly, the opposite MR effect would significantly separate the HOMO/LUMO wavefunctions to trigger the TADF character.

5.2 Results and discussion

5.2.1 Molecular structure and synthesis

The B/N atom fused narrowband emitters, namely PhCzBN1 and PhCzBN2 were designed on the basis of the entirely planar CzBN-core, where the fused carbazole

fragment was used to replace the diphenylamine unit for larger rigidity. Then, the two compounds were synthesized by nucleophilic aromatic substitution reaction and tandem electrophilic arene borylation (**Figure 5-1**). The final products were purified by a temperature-gradient sublimation method under vacuum after recrystallization to obtain the highly pure materials, which were then used for the fabrication of organic lasers and OLEDs by vacuum deposition.

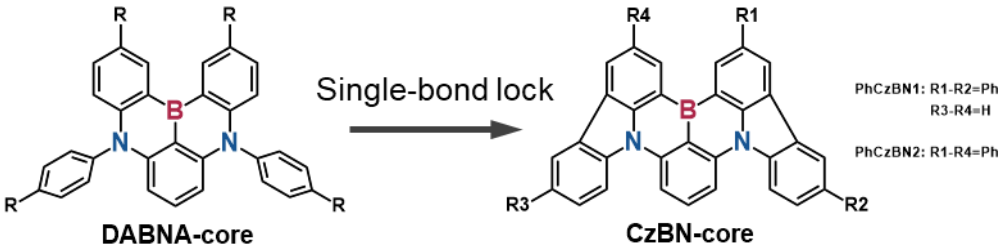

Figure 5-1. Molecular design toward entirely planar MR-TADF skeleton.

Benefitting from the planar and rigid frameworks, as can be seen in **Figure 5-2**, two derivatives based on the CzBN-core, PhCzBN1 and PhCzBN2, exhibited a very high temperature of decomposition (T_d) of 528 and 583 ℃, respectively, which was crucial to the operational stability in the light-emitting process. By comparison, T_d of DABNA2 was 486 ℃, which was lower than PhCzBN1 and PhCzBN2.

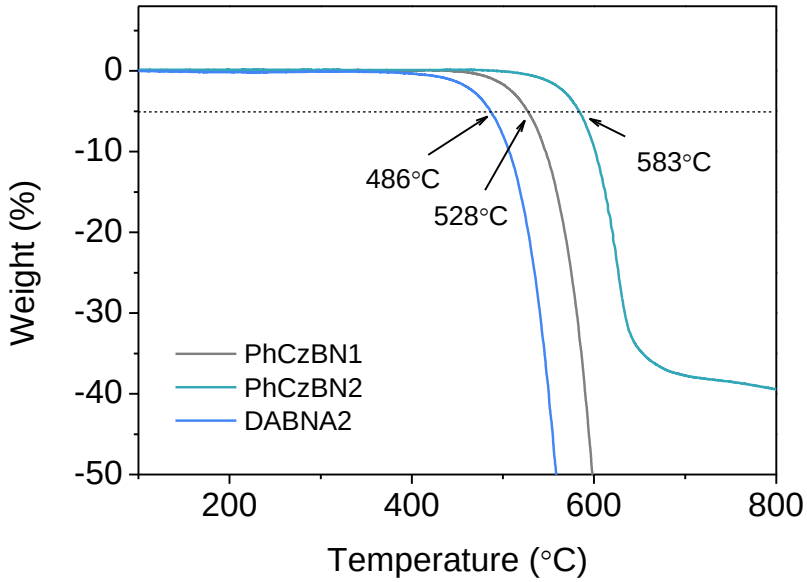

Figure 5-2. Thermogravimetry (TG) curve at one atmosphere. The 5 wt% loss point indicated the sublimation temperature of 528, 583, and 486 ℃ for PhCzBN1, PhCzBN2, and DABNA2, respectively.

5.2.2 Theoretical calculation

To investigate the differences between the geometric and optical properties of PhCzBN1/2, the ground-state geometries were initially optimized by DFT at the B3LYP/6-31+G(d, p) level in the gas phase. As shown in **Figure 5-3**, the HOMO wavefunctions were localized at the nitrogen atoms, which were located at the *meta*-position of a boron atom. Whereas the LUMO wavefunctions were localized at the electron-deficient boron atom at its *ortho*- and *para*-positions. It was worth noting that the fused B/N-based molecular skeleton was planar with the extreme rigidity. The phenyl substituents at the *para*-position of nitrogen atoms in PhCzBN1 and PhCzBN2 led to the longer conjugation length, however, with only slight HOMO wavefunction delocalization. Consequently, because the phenyl-units did not incorporate the distinct electron-donating or affinity capability, it made the emission redshift without reorganizing the wavefunction distributions, thereby maintaining the strong MR effect on the heterocyclic skeleton. Thus, the corresponding *f* of the ground state to the excited state (S_0-S_1) was as large as 0.4, guaranteeing a large k_r.

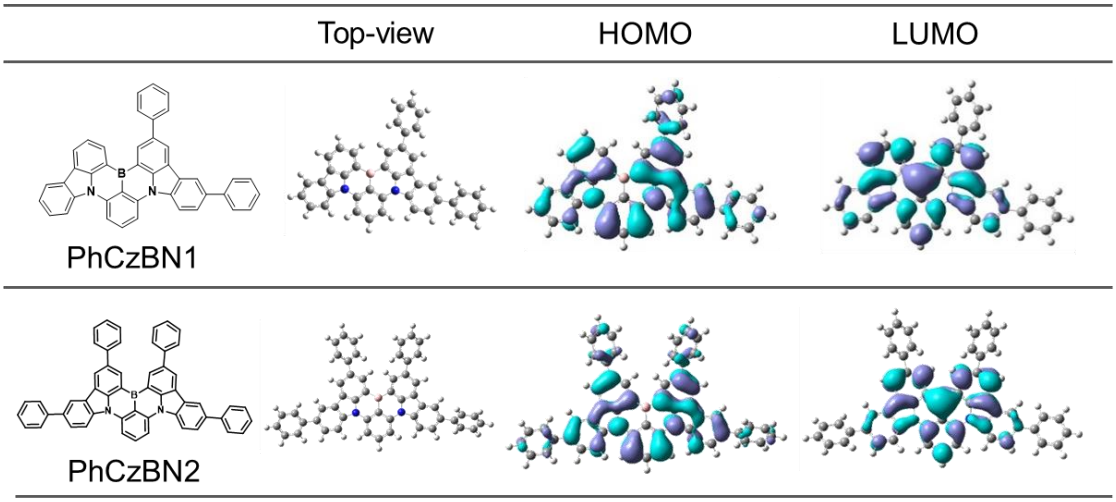

Figure 5-3. Molecular structures, HOMO and LUMO wavefunction distributions of PhCzBN1 and PhCzBN2, the latter of which was calculated using B3LYP/6-31+G (d, p).

5.2.3 Photophysical properties

UV-vis absorption and PL spectra of PhCzBN1 in toluene and solid-state films were measured [**Figure 5-4 (a)**]. The strong absorption band appeared below 300 nm, which arose from the π-π* transition. Meanwhile, the narrow ICT absorption band was located in the 400−500 nm regime. Owing to the planar and rigid molecular structure, either structural relaxation or vibration at the excited state was largely suppressed, therefore, a smaller Stokes shift occurred between the absorption band and PL spectra. In that case, the FWHM of the PL spectrum of PhCzBN1 in toluene was only 25 nm (0.13 eV). The narrow PL spectrum of PhCzBN1: mCBP blend films with a low doping ratio of 1 wt% also had a FWHM value of ~29 nm (~0.14 eV). However, the excimer induced by molecule aggregation with much broader FWHM would take place under the higher doping concentration of 5 wt% (~63 nm, ~0.29 eV) and in neat films (~113 nm, ~0.44 eV). Furthermore, because of the suppressed concentration quenching effect under the lower concentration, the PLQY of 1 wt% PhCzBN1 or PhCzBN2: mCBP blend films was as high as 99% and 94%, respectively. By comparison, the 1 wt% DABNA2: mCBP blend film exhibited a lower PLQY of 88%.

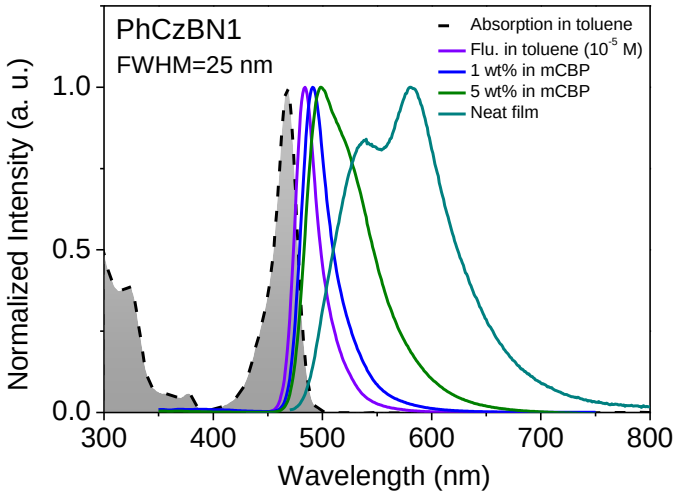

Figure 5-4. (a) Absorption and fluorescence of PhCzBN1 in toluene (10^{-5} M in toluene) and blend films with CBP at different doping ratios (1 wt%, 5 wt% and neat film).

The time-dependent transient PL lifetime was subsequently estimated. As shown in **Figure 5-5 (a)**, both PhCzBN1 and PhCzBN2 exhibited a very small prompt decay lifetime (~6.5 ns) in mCBP blend films, which was close to the DABNA-core based molecule (DABNA2). The k_r of PhCzBN1, PhCzBN2, and DABNA2 was over 1.0×10^8 s^{-1}. Encouragingly, PhCzBN1 and PhCzBN2 showed the faster triplet up-conversion process, with the delayed lifetime of around 50 μs, which was slightly smaller than the one of DABNA2. The longer triplet upconversion lifetime might cause the detrimental effects in the OLED and lasers.

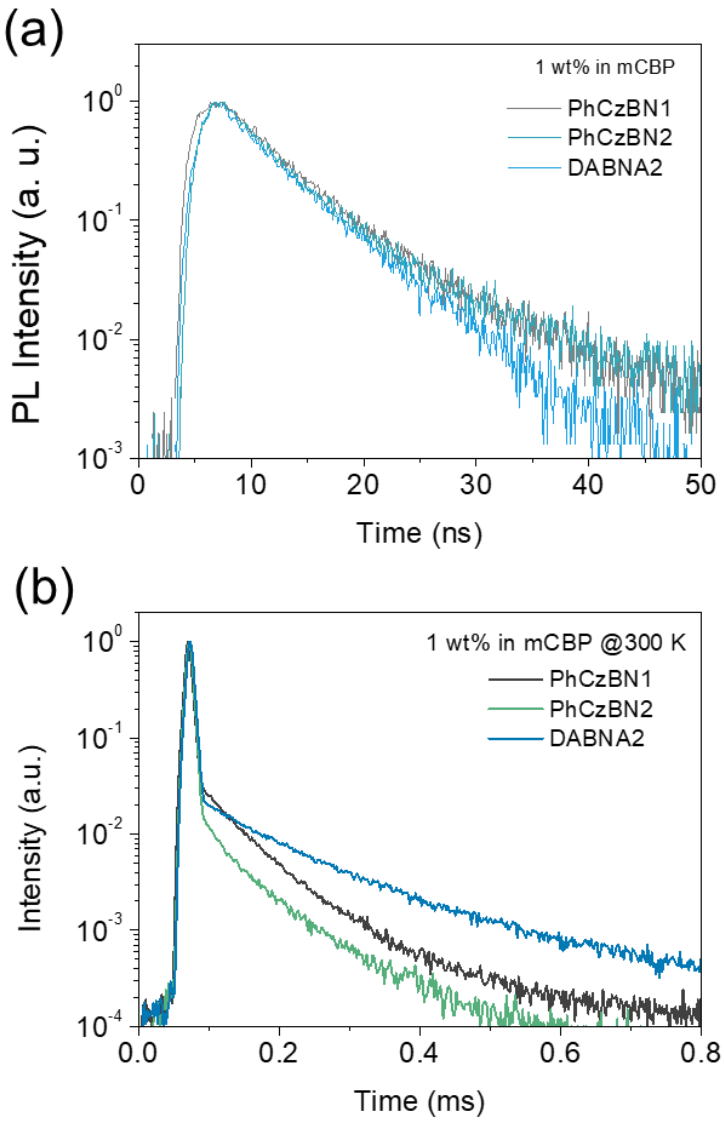

Figure 5-5. Transient PL spectra. (a) The prompt component and (b) the delayed component of 1 wt% PhCzBN1, PhCzBN2, and DABNA2 doped in mCBP films, respectively.

5.2.4 ASE properties

Owing to the large f and k_r of PhCzBN1 and PhCzBN2, it was promising to evaluate the corresponding ASE/laser properties. 1 wt% PhCzBN1 or PhCzBN2: mCBP blend films were thermally deposited on a quartz substrate, which was then photo-excited by a nitrogen laser source subsequently. Consequently, it showed not only a nonlinear increase of emission output, but also an abrupt narrowing of FWHM when gradually increasing the excitation intensity, which indicated the ASE activity. After plotting

Figure 5-6 (a) (b), the ASE thresholds of around 9.0 μJ cm^{-2} for PhCzBN1- and PhCzBN2-based films could be respectively determined. Meanwhile. the corresponding ASE spectral peaks were around 508 and 516 nm, respectively. Furthermore, the σ_{em} has been estimated from the Eq. 2-1, the corresponding σ_{em} at the ASE peak of PhCzBN1 and PhCzBN2-based blend films is around 8.0 ×10^{-17} cm^2.

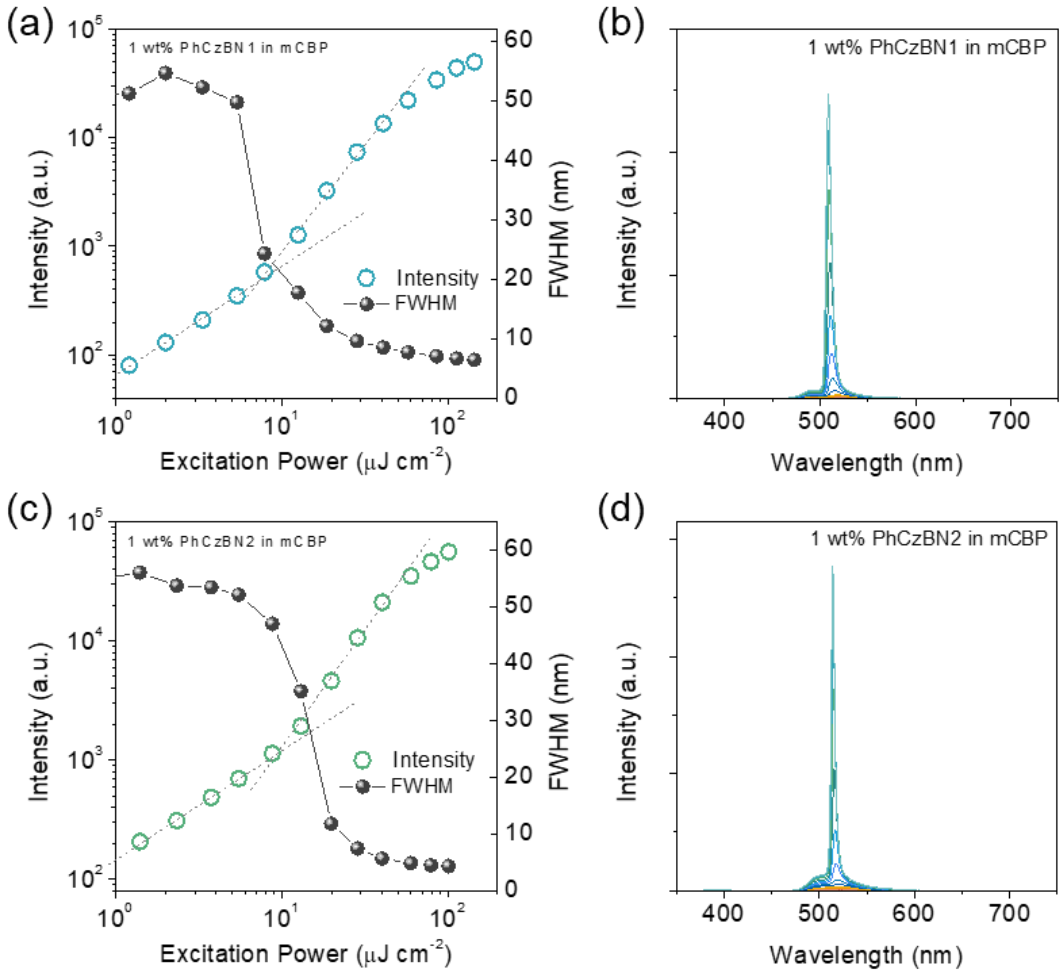

Figure 5-6. ASE performance of PhCzBN1/2-based solid-state films in a mCBP host matrix. Output waveguide emission intensity versus excitation power relationship of (a) PhCzBN1-based and (c) PhCzBN2-based solid-state films. Spectral shape changes with increasing the excitation power for (b) PhCzBN1-based and (d) PhCzBN2-based solid-state films.

In addition, the ASE stability was also evaluated under the nitrogen gas atmosphere. As shown in **Figure 5-7 (c)**, compared to DABNA2 without a fully locked molecular skeleton, the samples based on PhCzBN1 and PhCzBN2 exhibited better ASE stability with a suppressed intensity rolloff, which could still maintain closely 80% of the initial ASE intensity under the continuous excitation (excitation power ~40 μJ cm^{-2}) for two hours, implying that the reinforced rigid molecular structure with high T_d could inhabit the molecule degradation under the high excitation intensity. Meanwhile, the accelerated triplet up-conversion process would relieve the severe triplet-related quenching or annihilation to some degree.

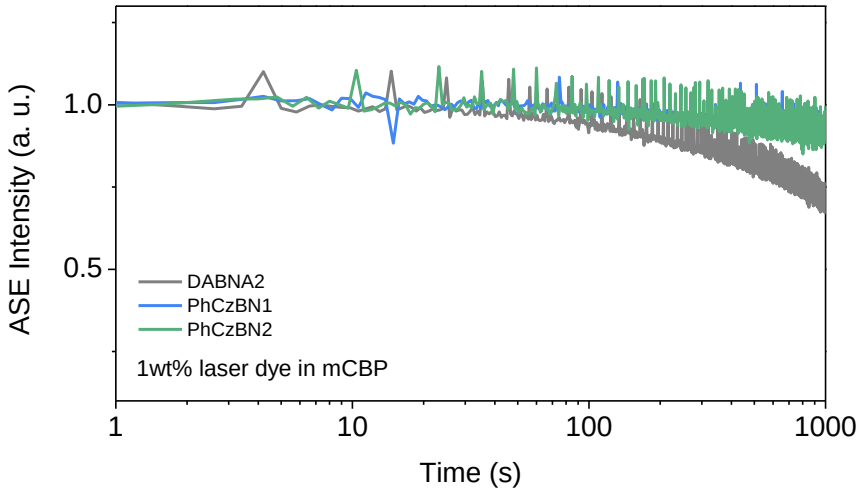

Figure 5-7. ASE stability of PhCzBN1-, PhCzBN2-, and DABNA2-based solid-state films.

5.2.5 Second-order DFB lasers based on PhCzBN1 TADF molecule

The laser properties of the 2nd-order DFB devices based on a 1 wt% PhCzBN1: mCBP blend film were examined under pulsed optical pumping by a nitrogen gas laser. Here, the 2nd-order DFB structures with diverse Λ_2 of 300, 310, and 315 nm were designed. As shown in **Figure 5-8**, the Λ_2-dependent DFB laser thresholds of 1 wt% PhCzBN1: mCBP blend films were estimated around 1 μJ cm^{-2}, which were much lower than the ASE threshold. Meanwhile, the laser spectral peak could be flexibly

tuned from 505 nm (Λ_2=305 nm) to 526 nm (Λ_2=315 nm) by rationally manipulating the vibronic bands spanning the entire emission spectrum.

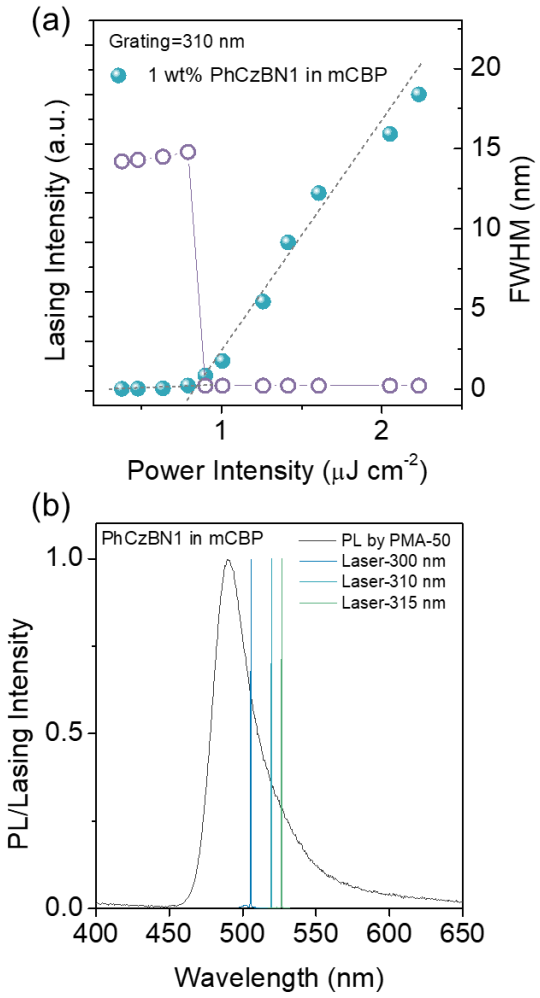

Figure 5-8. 2nd order DFB lasers properties. Change of laser intensity and FWHM as a function of excitation power for laser devices with DFB grating periods of (a) 310 nm, and (b) PL and laser spectra were detected by a photonic multichannel analyzer (PMA-50). The inset is the laser beam from the devices.

To further confirm the laser activity, the investigation of polarization, far-field, and near-field interference patterns of the beam divergence from one laser device has been systematically carried out. As shown in **Figure 5-9 (a)**, the laser output beam from the 1 wt% PhCzBN1: mCBP blend film could be clearly detected when a luminescent card

was placed at a distance of 10 cm. In addition, the interference patterns could be feasibly observed by a luminescent card in front of the samples in Figure 5-9 (b).

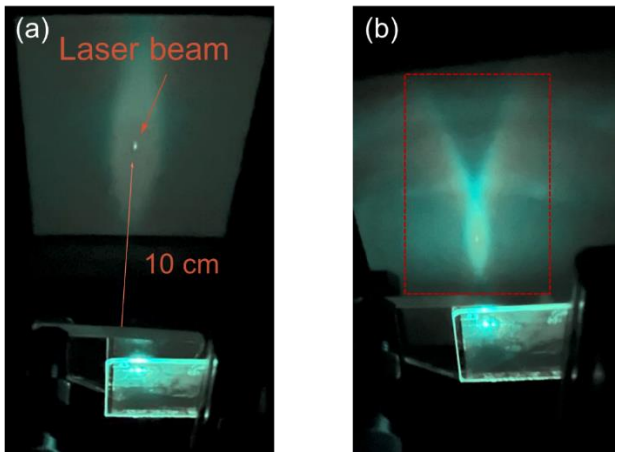

Figure 5-9. 2nd order DFB lasers properties based on the PhCzBN1: mCBP blend film. (a) Far-field laser beams and (b) interference patterns of the DFB lasers.

As shown in **Figure 5-10**, the 2nd-order DFB laser exhibited a strong, linear transverse electric polarization, with a degree of polarization of 99.5%, which was accordingly calculated from the equation: $(I_{max} - I_{min})/(I_{max} + I_{min})$, where I_{max} and I_{min} denoted the maximum intensity at 0° and the minimum intensity at 90°, respectively. Consequently, the high degree value indicated the remarkable polarization characteristics of the TADF laser system.

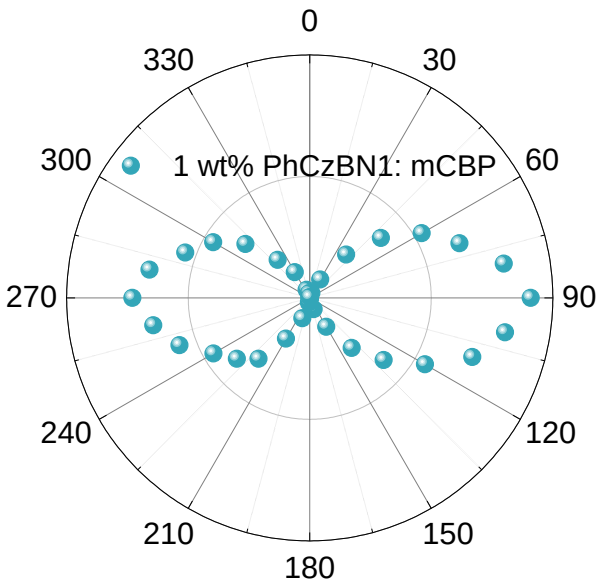

Figure 5-10. The polarization property of the 2nd order DFB lasers properties based on the PhCzBN1: mCBP blend film.

5.2.6 EL properties

The EL properties based on PhCzBN1 were further investigated, DABNA2 was also selected to evaluate the EL performance for a better comparison. The multilayered OLEDs were designed as the following configuration: glass substrate/ITO (anode)/HAT-CN (HIL, 10 nm)/Tris-PCz (HTL, 30 nm)/mCBP (EBL, 5 nm)/ mCBP: PhCzBN1 or DABNA2 (EML, 30 nm, 1 wt%)/SF3-TRZ (HBL, 10 nm)/SF3-TRZ: Liq (ETL, 20 nm, 30 wt%)/ Liq (EIL, 2 nm)/ Al (cathode, 100 nm). Here, HAT-CN was used as the HIL, Tris-PCz was the HTL, a thin mCBP film of 5 nm was inserted to block the electrons. Then, a 1 wt% PhCzBN1 or DABNA2: mCBP blend film was the EML, 10 nm SF3-TRZ film was then followed not only to block the holes, but also to prevent the migration of Liq to quench the excitons, Liq: SF3-TRZ blend film was employed as the ETL, 2 nm Liq film was the EIL. As shown in **Figure 5-6**, the maximum EQE of OLEDs based on the PhCzBN1-based single-host system is around 10%, which exceeded the theoretical limitation (EQE~5%) of a conventional fluorescence emitter, indicating the contribution from the up-converted triplets. By comparison, DABNA2-based OLED exhibited a lower EQE of 6.2%. More importantly, PhCzBN1-based

OLED possessed a much better operational stability than the one based on DABNA2. In detail, T_{50} of PhCzBN1-based device exceeded 80 hours, while the one of DABNA2 was only 3 hours, indicating the remarkable stability for the CzBN-core as anticipated. Furthermore, in order to further improve the EQEs and operational stability, the TADF-assisted fluorescence (TAF) strategy was employed to accelerate the triplet up-conversion process. Therefore, TPh2Cz2DPhCzBN (HDT-1) with a faster k_{RISC} (~10^6 s^{-1}) was employed as the TADF assistant dopant to upconvert the generated triplets to singlets, then the singlet excitons transferred to the singlet energy level of PhCzBN1, which was followed by radiative transition. As expected, the maximum EQE of TAF-OLED was boosted to ~20%, as well as the greatly improved device stability with T_{80} over 100 hours.

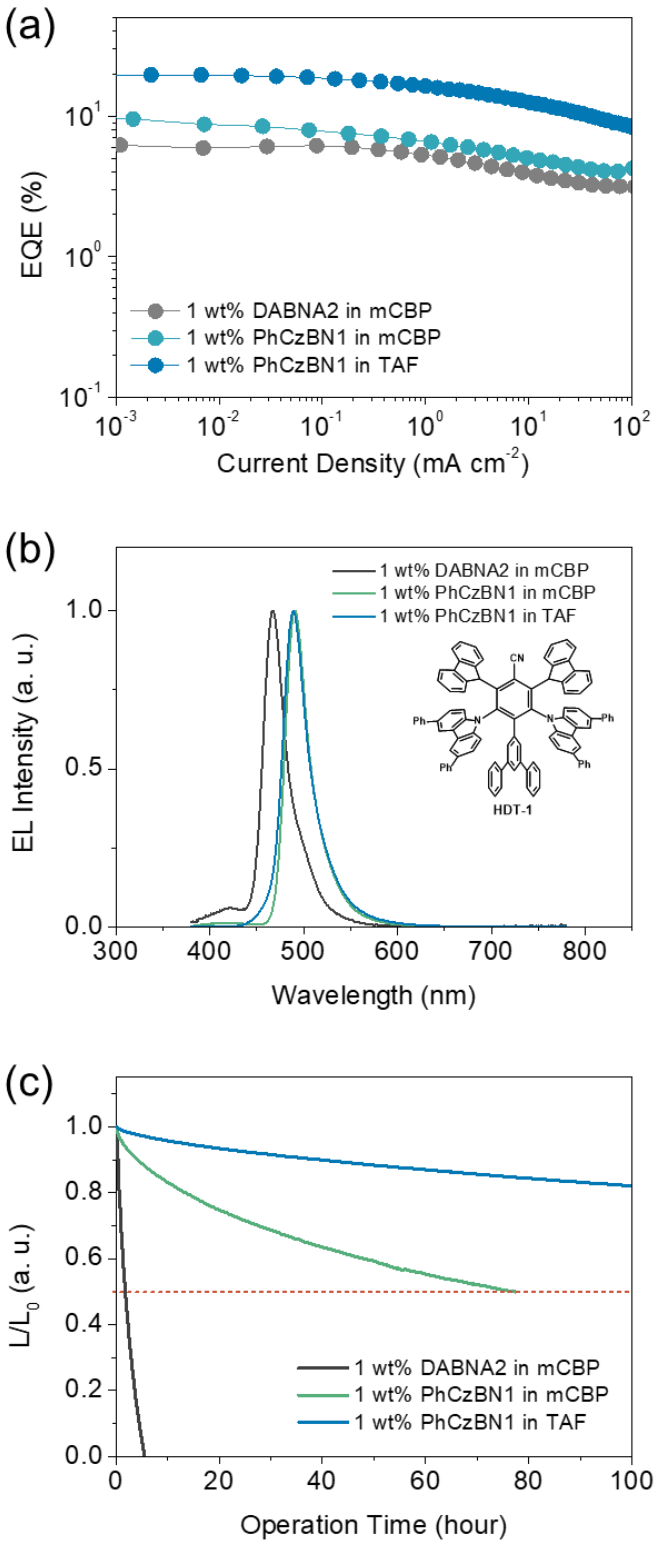

Figure 5-11. OLED performance based on PhCzBN1 and DABNA2. (a) EQE to current density curve; (b) EL spectra and (c) the operational lifetime of the single-host and TADF-assistant fluorescence (TAF) devices.

5.3 Conclusion

In summary, we designed a B/N-atom-based sky-blue TADF emitter PhCzBN1 with very narrowband emission (FWHM~25 nm). Compared to the conventional TADF molecules with the twisted D-A configuration, this polycyclic framework exhibited the remarkable features of an extreme planarity and rigidity, which largely suppressed the nuclear vibrational relaxation and structural twisting. Thus, the inducing large f (~0.4) led to the outstanding laser property with a low threshold of around 1 μJ cm^{-2}. Moreover, the significant localization of the HOMO/LUMO wavefunctions on B/N atoms guaranteed the reduced ΔE_{ST}, thereby triggering the TADF characteristic. Due to the triplet contribution, the EQE of the corresponding OLEDs could exceed the theoretical limitation (~5%) of fluorescence emitters with optimized operational stability. To further improve the EQE values and stability, TADF assistant HDT-1 was employed to fasten the triplet up-conversion process in TAF-OLED. Consequently, ~20% EQE could be achieved with the much-improved device stability.

5.4 Experimental section

Materials

All reagents were used from the commercial sources and were used as purchased without further purification. Column chromatographic separations were conducted by 200-300 nm silica gel. NMR spectra were obtained in $CDCl_3$ or DMSO-d_6 with a Bruker Biospin Avance-III 500 NMR spectrometer at the ambient temperature. Chemical shifts (δ) were denoted in parts per million (ppm) relative to tetramethylsilane (TMS) as an internal reference. Elemental analyses (C, H and N) were carried out with a Yanaco MT-5 elemental analyzer.

Synthesis route

9*H*-carbazole (5.00 g, 29.9 mmol) was fully dissolved in dry *N*,*N*-dimethylformamide (180 mL) in a round-bottom flask equipped under nitrogen atmosphere. The sodium hydride (1.32 g, 32.8 mmol, 60% dispersion in mineral oil) was slowly added and the obtained mixture was stirred for an hour at room temperature. Then, 2-bromo-1,3-difluorobenzene (6.35 g, 32.8 mmol) was added and the reaction solution was heated to 80 °C for 5 hours. The reaction was quenched with water and the precipitate was filtered off. The isolated product was purified by flash column chromatography (silica gel, chloroform/hexane: 1/9). Yield: 51% (5.18 g). ^{1}H NMR (500 MHz, $CDCl_3$, 298 K, relative to Me_4Si): δ=8.16 (d, 2H, J=8.0 Hz), 7.52−7.50 (m, 1H), 7.42 (t, 2H, J=7.5 Hz), 7.36−7.30 (m, 4H), 7.08 (d, 2H, J=8.0 Hz). ^{13}C NMR (125 MHz, $CDCl_3$): δ=161.62, 159.64, 140.72, 138.87, 129.27, 129.20, 126.50, 126.47, 126.11, 123.46, 120.46, 120.30, 116.73, 116.56, 111.70, 111.54, 110.03. MS (APCI) calcd. for $C_{18}H_{11}BrFN$: *m/z* = 339.01; found: 338.93 $[M]^+$.

3,6-Diphenyl-9*H*-carbazole (3.38 g, 10.5 mmol) was fully dissolved in dry *N*,*N*-dimethylformamide (150 mL) in a round-bottom flask equipped with a condenser under nitrogen atmosphere. The sodium hydride (0.46 g, 11.4 mmol, 60% dispersion in mineral oil) was slowly added and the obtained mixture was stirred for an hour at room temperature. Then, 9-(2-bromo-3-fluorophenyl)-9*H*-carbazole (3.00 g, 8.8 mmol) was added and the reaction solution was heated to 130 °C for 16 hours. The reaction was

quenched with water and the precipitate was filtered off. The isolated product was purified by flash column chromatography (silica gel, chloroform/hexane: 3/7). Yield: 74% (4.17 g). ^{1}H NMR (500 MHz, $CDCl_3$, 298 K, relative to Me_4Si): δ=8.42 (s, 2H), 8.18 (d, 2H, J=7.5 Hz), 7.82−7.77 (m, 1H), 7.75−7.72 (m, 8H), 7.51−7.47 (m, 6H), 7.38−7.33 (m, 4H), 7.29 (d, 2H, J=8.0 Hz), 7.23 (d, 2H, J=8.5 Hz). ^{13}C NMR (125 MHz, $CDCl_3$): δ=141.91, 140.78, 140.72, 139.47, 139.26, 134.18, 131.48, 131.22, 12.64, 128.86, 127.44, 126.75, 126.24, 125.99, 124.18, 123.56, 120.58, 120.41, 119.18, 110.37, 109.97. MS (APCI) calcd. for $C_{42}H_{27}BrN_2$: *m/z*=638.14; found: 638.14 $[M]^+$.

A toluene solution (100 mL) containing 9-(2-bromo-3-(9*H*-carbazol-9-yl)phenyl)-3,6-diphenyl-9*H*-carbazole (2.00 g, 3.1 mmol) was added *n*-butyllithium (2.30 mL, 3.7 mmol, 1.6 M in hexane) slowly at −30 °C under a nitrogen atmosphere. The reaction mixture was slowly warmed to room temperature and stirred at 60 °C for 2 hours. After addition of boron tribromide (0.36 mL, 3.7 mmol) at −15 °C, the reaction mixture was stirred at room temperature for 1 hour. N,N-diisopropylethylamine (1.19 mL, 6.8 mmol) was added at 0 °C and then the reaction mixture was allowed to warm to room temperature. After stirring at 110 °C for 10 hours, the reaction mixture was cooled to room temperature. An aqueous solution of sodium acetate and ethyl acetate was added to the reaction mixture. the precipitate was filtered off. The crude product was dissolved in hot toluene to recrystallize, then sublimation. Yield: 31% (0.55 g). ^{1}H NMR (500 MHz, $CDCl_3$, 298 K, relative to Me_4Si): δ=9.15 (s, 1H), 8.98 (d, 1H, J=7.0 Hz), 8.60 (s, 1H), 8.50 (t, 2H, J=8.5 Hz) 8.46 (s, 1H), 8.39−8.35 (m, 3H), 8.24 (d, 1H, J=7.5 Hz), 8.03 (t, 1H, J=8.0 Hz). 7.91 (d, 2H, J=7.0 Hz), 7.85 (d, 1H, J=7.0 Hz), 7.80 (d, 2H, J=7.5 Hz), 7.69 (t, 1H, J=7.5 Hz) 7.64−7.59 (m, 3H), 7.55 (t, 2H, J=7.5 Hz), 7.47 (t, 2H, J=8.0 Hz), 7.42 (t, 1H, J=7.5 Hz). MS (APCI) calcd. for $C_{42}H_{25}BN_2$: *m/z* = 568.21; found: 568.43 $[M]^+$. Elemental analysis calcd. (%) for $C_{42}H_{25}BN_2$: C 88.74, H 4.43, N 4.93; found: C 88.83, H 4.37, N 4.95.

9,9'-(2-Bromo-1,3-phenylene)bis(3,6-diphenyl-9*H*-carbazole). 3,6-Diphenyl-9*H*-carbazole (1.00 g, 3.13 mmol) was fully dissolved in dry *N*,*N*-dimethylformamide (20 mL) in a round-bottom flask equipped with a condenser under nitrogen atmosphere. The sodium hydride (0.13 g, 3.13 mmol, 60% dispersion in mineral oil) was slowly

added and the obtained mixture was stirred for an hour at room temperature. Then, 2-bromo-1,3-difluorobenzene (0.26 g, 1.35 mmol) was added and the reaction solution was heated to 130 °C for 18 hours. The reaction was quenched with water and the precipitate was filtered off. The isolated product was purified by flash column chromatography (silica gel, chloroform/hexane: 4/6). Yield: 76% (0.81 g). ^{1}H NMR (500 MHz, $CDCl_3$, 298K, relative to Me_4Si): δ=8.44 (s, 4H), 7.83−7.74 (m, 15H), 7.50 (t, 8H, J=7.5 Hz), 7.37 (m, 4H), 7.32 (d, 4H, J=8.5 Hz).

To a dry toluene solution (90 mL) containing 9,9'-(2-bromo-1,3-phenylene)bis(3,6-diphenyl-9*H*-carbazole) (3.00 g, 3.79 mmol) was added *n*-butyllithium (2.84 mL, 4.55 mmol, 1.6 M in hexane) slowly at −30 °C under a nitrogen atmosphere. The reaction mixture was slowly warmed to room temperature and stirred at 60 °C for 2 hours. After addition of boron tribromide (0.44 mL, 4.55 mmol) at −15 °C, the reaction mixture was stirred at room temperature for 1 hour. *N*,*N*-diisopropylethylamine (1.45 mL, 8.34 mmol) was added at 0 °C and then the reaction mixture was allowed to warm to room temperature. After stirring at 110 °C for 8 hours, the reaction mixture was cooled to room temperature. An aqueous solution of sodium acetate and ethyl acetate was added to the reaction mixture. The precipitate was filtered off. The crude product was dissolved in hot toluene to recrystallize, then sublimation. Yield: 24% (0.66 g). MS (APCI) calcd. For $C_{54}H_{33}BN_2$: *m/z* = 720.27; found: 720.2 $[M]^+$. Elemental analysis calcd. (%) for $C_{54}H_{33}BN_2$: C 90.00, H 4.62, N 3.89; found: C 90.10, H 4.54, N 3.91.

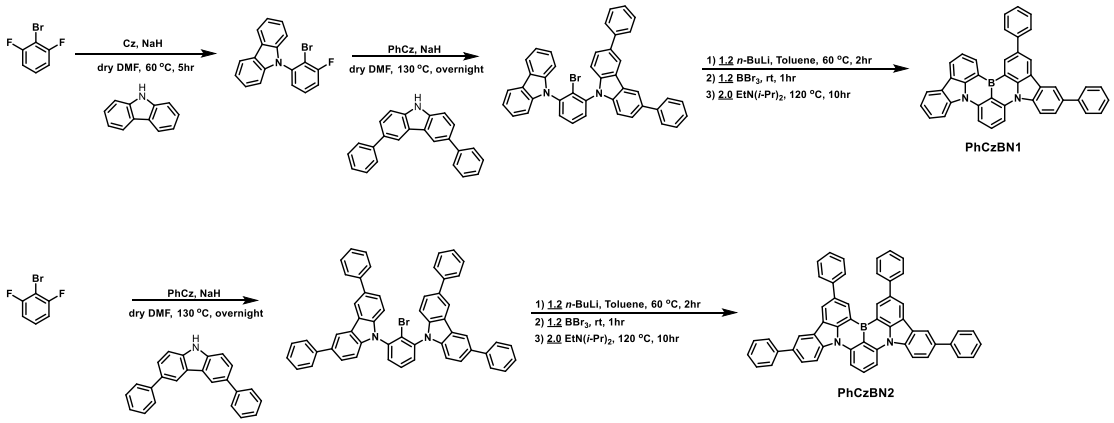

Figure 5-12. Molecule synthesis route of PhCzBN1 and PhCzBN2.

Theoretical calculation

DFT calculation was employed to simulate the electron density distributions of HOMO and LUMO wavefunctions of the TADF laser dyes. The molecular structure optimization was obtained by the hybrid B3LYP functional and 6-31+G(d, p) basis set using the Gaussian 16 program package.

Thermal properties

Thermal gravimetry-differential analysis was conducted by a Bruker TG-DTA2400SA under the nitrogen atmosphere, the corresponding heating rate was 10 ℃ min^{-1}. A Netzsch DSC204 Phoenix calorimeter was used for differential scanning calorimetry analysis at a scanning rate of 5 ℃ under the nitrogen atmosphere.

Optical characterization

The ground-state UV-vis absorption spectra were measured by a spectrophotometer (LAMBDA 950-PKA, PerkinElmer). The steady-state fluorescence at room-temperature and phosphorescence at 77 K was recorded by a multichannel spectrofluorometer (FP-8600, JASCO). The PLQYs were measured by an absolute photoluminescence quantum yield measurement system (C11347-01 Quantaurus-QY, Hamamatsu Photonics, Japan). The PLQY measurement of the dye in toluene was conducted after nitrogen-gas bubbling for 15 minutes. The PLQY measurement of the blend films was carried out under Ar flow. The time-dependent transient PL decay of the solution or blend films was conducted by a Quantaurus-Tau fluorescence lifetime system (C11367-03, Hamamatsu Photonics, Japan) and an integrated streak camera (C4334, Hamamatsu Photonics, Japan).

Organic solid-state film fabrication and ASE measurement

PhCzBN1- and PhCzBN2-based blend films were thermally co-deposited onto the substrates in the vacuum chamber. For ASE measurement, the prepared solid-state films were optically-excited at the edge region by a nitrogen-gas lasing source (NL100, Stanford Research System, excitation lasing wavelength is 337 nm), The output lasing beam was shaped to a stripe. The ASE emission was detected from the edge of the quartz substrate by a spectrometer (Hamamatsu Photonics PMA-12). ASE measurements are conducted under the nitrogen atmosphere to prevent the degradation

caused by oxygen and moisture.

DFB structure fabrication

A silicon dioxide layer with a thickness of 1000 nm was sputtered onto the glass substrates to avoid the exciton quenching by the glass. Then, the substrates were subsequently washed as the aforementioned steps. After the UV-ozone treatment, hexamethyldisilazane was spin-coated on the silicon dioxide surface at 4000 rpm for 15 s and then annealed at 120 ℃ for 120 s. Afterward, to form a resist layer, ZEP520A-7 solution (ZEON Co.) was dropped onto the surface by spin-coating at 4000 rpm for 30 s, and followed by annealing at 180 ℃ for 4 min. Next, the electron-beam lithography (JEOL, JBX-5500SC) was used to obtain the grating patterns on the resist layer. For the development of the resist layers, the grating patterns were developed in ZED-N50 (ZEON Co.) solution at room temperature. During the process of etching, the resist layer was employed as the protecting layer while the substrates have undertaken the plasma-etching with CHF_3 using an EIS-200ERT etching system (Elionix). For completely removing the resist layer from the substrates, they were plasma-etched with O_2 using a FA-1EA etching system (SAMCO).

Fabrication and characterization of optical-pumping organic laser

After finishing the 2^{nd}-order DFB fabrication, PhCzBN1-based mCBP blend films were thermally evaporated on the DFB substrates, and the thickness was controlled at 200 nm. Then, several droplets of CYTOP (Asahi Glass Co. Ltd.) were spin-coated on the surface of the organic films. The samples were encapsulated by a sapphire lid, which were then dried under vacuum overnight. A nitrogen-gas laser source (NL100, Stanford Research System, excitation lasing wavelength is 337 nm) was employed to optically excite the DFB samples, and the output beam was concentrated to a small-size light spot through a lens and a slit. The laser intensity and spectral shapes were recorded by a multichannel spectrometer (PMA-50, Hamamatsu Photonics) with an optical fiber. The N_2 laser intensity was manipulated by adjusting the neutral density filter with multiple channels.

OLED device fabrication and characterization

The functional organic layers and conductive metallic layer (Al) were subsequently deposited onto the pre-patterned ITO substrates with different shadow masks for the sandwich-like structure. Then, the encapsulation was carried out by a glass cap and UV curing epoxy resin in the glove box with nitrogen atmosphere immediately, to prevent the degradation caused by moisture and oxygen. The device performance was thereby evaluated after the encapsulation. The $J-V$, L, and EQEs were measured under the DC mode by a calibrated luminance meter (CS-2000, Konica Minolta, Japan), and integrated with a constant source meter (Keithley 2400, Keithley Instruments Inc.).

References

[1] Z. Yang, Z. Mao, Z. Xie, Y. Zhang, S. Liu, J. Zhao, J. Xu, Z. Chi, M. P. Aldred, *Chem. Soc. Rev.* **2017**, *46*, 915.

[2] M. Y. Wong, E. Zysman-Colman, *Adv. Mater.* **2017**, *29*, 1605444.

[3] H. Kaji, H. Suzuki, T. Fukushima, K. Shizu, K. Suzuki, S. Kubo, T. Komino, H. Oiwa, F. Suzuki, A. Wakamiya, Y. Murata, C. Adachi, *Nat. Commun.* **2015**, *6*, 8476.

[4] Q. Zhang, J. Li, K. Shizu, S. Huang, S. Hirata, H. Miyazaki, C. Adachi, *J. Am. Chem. Soc.* **2012**, *134*, 14706.

[5] H. Uoyama, K. Goushi, K. Shizu, H. Nomura, C. Adachi, *Nature* **2012**, *492*, 234.

[6] H. Tanaka, K. Shizu, H. Miyazaki, C. Adachi, *Chem. Commun.* **2012**, *48*, 11392.

[7] Y. Liu, C. Li, Z. Ren, S. Yan, M. R. Bryce, *Nat. Rev. Mater.* **2018**, *3*, 18020.

[8] X.-K. Chen, D. Kim, J.-L. Brédas, *Acc. Chem. Res.* **2018**, *51*, 2215.

[9] V. Jankus, P. Data, D. Graves, C. McGuinness, J. Santos, M. R. Bryce, F. B. Dias, A. P. Monkman, *Adv. Funct. Mater.* **2014**, *24*, 6178.

[10] X.-K. Chen, B. W. Bakr, M. Auffray, Y. Tsuchiya, C. D. Sherrill, C. Adachi, J.-L. Bredas, *J. Phys. Chem. Lett.* **2019**, *10*, 3260.

[11] A. Khan, X. Tang, C. Zhong, Q. Wang, S.-Y. Yang, F.-C. Kong, S. Yuan, A. S. D. Sandanayaka, C. Adachi, Z.-Q. Jiang, L.-S. Liao, *Adv. Funct. Mater.* **2021**, *31*, 2009488.

[12] Y. Kondo, K. Yoshiura, S. Kitera, H. Nishi, S. Oda, H. Gotoh, Y. Sasada, M. Yanai, T. Hatakeyama, *Nat. Photon.* **2019**, *13*, 678.

[13] H. Nakanotani, T. Furukawa, C. Adachi, *Adv. Opt. Mater.* **2015**, *3*, 1381.

[14] H. Tanaka, S. Oda, G. Ricci, H. Gotoh, K. Tabata, R. Kawasumi, D. Beljonne, Y. Olivier, T. Hatakeyama, *Angew. Chem. Int. Ed.* **2021**, *60*, 17910.

[15] Y. Zhang, D. Zhang, J. Wei, Z. Liu, Y. Lu, L. Duan, *Angew. Chem. Int. Ed.* **2019**, *58*, 16912.

[16] Y. Zhang, D. Zhang, T. Huang, A. J. Gillett, Y. Liu, D. Hu, L. Cui, Z. Bin, G. Li,

J. Wei, L. Duan, *Angew. Chem. Int. Ed.* **2021**, *60*, 20498.

[17] T. J. Penfold, E. Gindensperger, C. Daniel, C. M. Marian, *Chem. Rev.* **2018**, *118*, 6975.

[18] T. J. Penfold, F. B. Dias, A. P. Monkman, *Chem. Commun.* **2018**, *54*, 3926.

[19] X. Cai, X. Li, G. Xie, Z. He, K. Gao, K. Liu, D. Chen, Y. Cao, S.-J. Su, *Chem. Sci.* **2016**, *7*, 4264.

[20] F. Chen, L. Zhao, X. Wang, Q. Yang, W. Li, H. Tian, S. Shao, L. Wang, X. Jing, F. Wang, *Sci. China Chem.* **2021**, *64*, 547.

[21] X. Wu, B.-K. Su, D.-G. Chen, D. Liu, C.-C. Wu, Z.-X. Huang, T.-C. Lin, C.-H. Wu, M. Zhu, E. Y. Li, W.-Y. Hung, W. Zhu, P.-T. Chou, *Nat. Photon.* **2021**, *15*, 780.

[22] M. Yang, I. S. Park, T. Yasuda, *J. Am. Chem. Soc.* **2020**, *142*, 19468.

Chapter 6. Conclusion and perspective

6.1 Conclusion

In summary, the works presented in this thesis mainly focused on the investigation of the intramolecular interactions in D-A type configurations from fluorescence toward the TADF-based OLEDs and organic solid-state lasers. In this regard, I obtained the following findings:

In **Chapter 2**, an electron-affinity substituent was conjugated with a DCNP-core, the introduction of weak D/A interplay inducing a CT state effectively maintained the moderate ΔE_{ST} (0.45 eV) of DCNP-pCN but did not affect the priority of the LE state, thereby retaining a large *f*. By comparison, the electron-donating substituent resulted in a distinct D-A separation, which enhanced the CT state and, thereby, suppressed the ASE/laser actions. Consequently, an excellent laser performance from 2^{nd}-order and mixed-order DFB devices could be obtained, with high stability and a low laser threshold around 2.0 μJ cm^{-2}. Moreover, exceeding 2% without efficiency rolloff was obtained over 17000 mA cm^{-2}.

In **Chapter 3**, a functional spacer was inserted in D-A-D molecules as a promising laser candidate. Importantly, the HOMO/LUMO wavefunction distributions could be manipulated by a rigid fluorene-core spacer, where the long alkyl chains were involved to guarantee good solubility and prevent intermolecular aggregation caused quenching. Meanwhile, the organic lasers showing emissions ranging from yellow to NIR could be adjusted by tuning the relative D/A interplay strength to realize color-tunable organic lasing properties from yellow to NIR emission. Resultantly, yellow lasers with low thresholds based on a $(TPA\text{-}F)_2BTD$ neat film were obtained (λ_{peak}~555 nm). Additionally, NIR lasers based on a 3 wt% $(TPA\text{-}F)_2BBTD$: CBP blend film, with a low threshold of around 1 μJ cm^{-2} (λ_{peak} ~845 nm) were achieved as well.

In **Chapter 4**, I proposed that the unconventional quasi-planar D-A structure, where a diphenyl methylene intramolecular-lock was incorporated to manipulate the HOMO/LUMO distributions by shrinking and fixing the torsion angles. This rigid configuration could largely restrict the intramolecular rotation and vibration. As a consequence, the rigid and quasi-planar TADF molecules, locked PXZN-B and

DMACN-B, exhibited remarkably blue-shifted structureless emission with small FWHMs of 44 and 29 nm, respectively. Moreover, both the emitters exhibited TADF characteristics, with high EQEs exceeding 10%. Furthermore, the locked D-A type TADF emitters could also exhibit promising laser performance with a low threshold of around 1 μJ cm^{-2}. Therefore, the intramolecular-lock strategy provided not only innovation for realizing high-efficiency deep-blue TADF emission with small FWHMs and high color purity but also an avenue for torching TADF-based ASE and lasers.

In **Chapter 5**, I designed a B/N atom based sky-blue TADF emitter PhCzBN1 with an entirely planar structure. Compared to the conventional TADF molecules with the twisted D-A configuration, the largely suppressed vibrational relaxation and bonding rotation led to a strong *f* and a small FWHM of 25 nm. Benefitting from the significant localization of the HOMO/LUMO wavefunctions on B/N atoms, TADF properties were successfully triggered and the EQE value could reach 10%. Moreover, tunable DFB lasers based on this TADF molecule could be realized by rationally manipulating the vibronic bands spanning the entire emission spectrum, and the lowest laser threshold was as low as around 1 μJ cm^{-2}.

Overall, to comprehend the molecular design principle of TADF laser dyes in this research, I prepared **Figure 6-1** to summarize the strategies of molecular design for D-A type laser dyes. Herein, the manipulation of LE and CT states by tuning diverse D/A interplays plays a crucial role. Firstly, it can be concluded that the LE state should dominate to guarantee the large radiative rates by investigating (i) electron-donating/accepting substituent effect in Chapter 2. Then, on the basis of the reasonable wavefunction overlap (LE state), good laser performance could be achieved by (ii) rationally inserting functional spacers to decrease the nonradiative process in Chapter 3. Then, a relatively large k_r and a small ΔE_{ST} could be satisfied together by (iii) using a rigid intramolecular lock to minimize the D/A torsion angle, which leads to the realization of laser performance in TADF molecules in Chapter 4. Finally, the TADF laser action could also be triggered based on (iv) an entirely rigid and planar D/A fused skeleton with MR effect from the opposite boron/nitrogen atoms in Chapter 5. Among

these D-A type molecules, from the aspect of σ_{em}, (TPA-F)$_2$BTD and (TPA-F)$_2$BBTD exhibit the best value exceeding 1.0 ×10^{-16} cm^2.

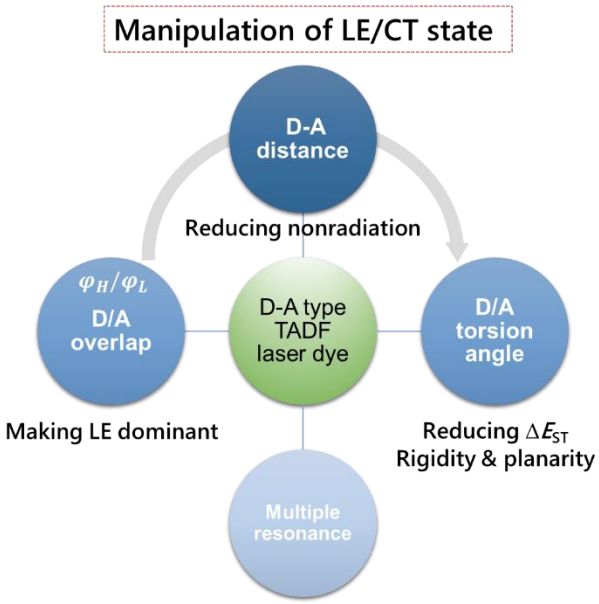

Figure 6-1. The general picture of D-A type molecular design toward TADF laser dyes.

It is worth noting that the trend of the TADF laser dyes is from a flexible D-A plane to a quasi-planar structure and an entirely planar configuration. In other words, it is important to reinforce the molecular planarity and rigidity. Benefitting from the shrinking torsion angle and the enhanced rigidity, molecular structural relaxation, as well as the vibrational relaxation at the excited state would be largely suppressed, and the closer HOMO/LUMO wavefunction distance leads to a stronger *f* and a higher quantum yield. Resultantly, DFB lasers were firstly realized based on TADF molecules to our best knowledge. In addition, the suppressed rotation and vibrational relaxation strategy could also lead to a small FWHM, which improved the color purity of TADF emitters. All the lasers obtained in this thesis have been summarized in **Figure 6-2**.

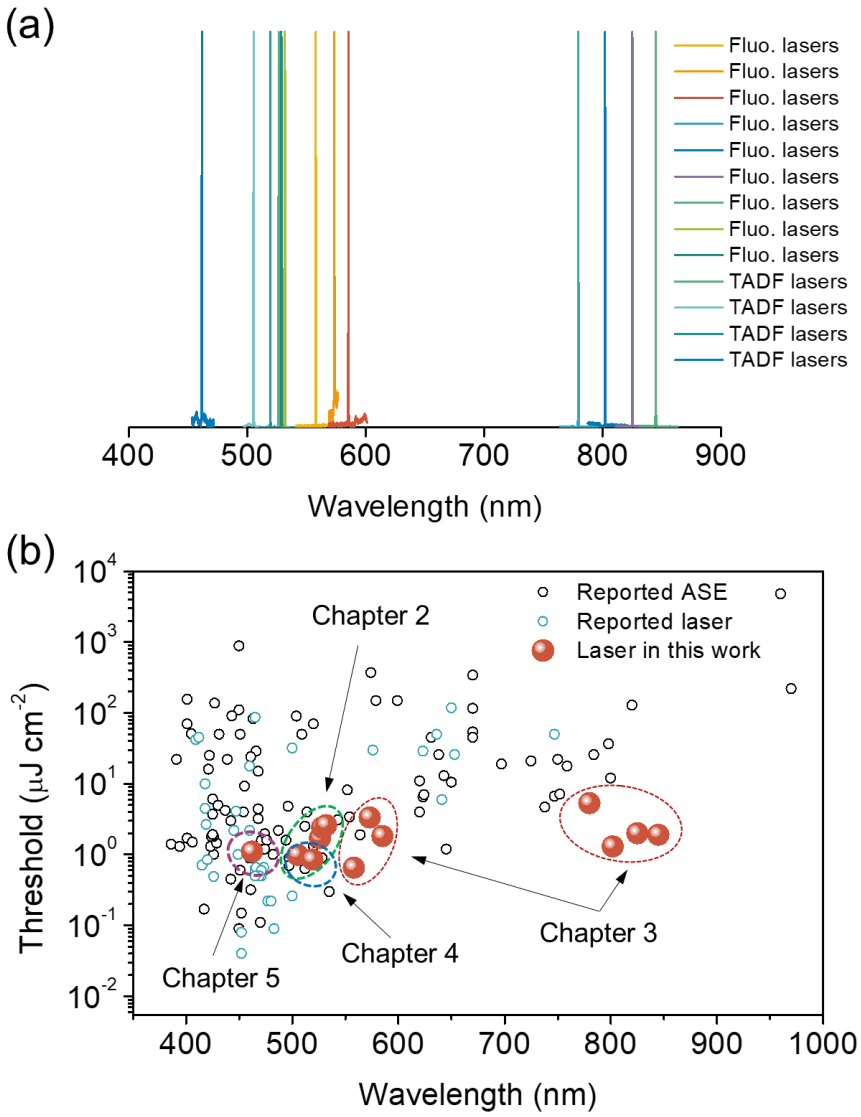

Figure 6-2. (a) Lasers obtained in this work. The laser wavelengths range from blue to NIR. (b) Summary of the representative ASE/lasers in the reported literature and this work.

6.2 Future plans

For the long term, electrical-pumping OSLDs have been always considered as a breakthrough worth to be targeted. Harvesting the spin-forbidden triplets for the radiation process is always the most ideal strategy to reduce the thresholds and strength the operational stability. Although an indication of electrical-pumping OSLDs based on

a fluorescent laser dye has been put forward recently, the very poor laser operational stability is an issue that should be addressed, and one of the main reasons is the extremely high laser threshold without the contribution from triplets, which occupies 75% of the generated excitons under electrical excitation. The TADF laser dyes reported in this work might provide the possibility to harvest triplets for reducing the laser thresholds under the electrical-pumping.

In this regard, I expect to first attempt the TADF lasers under a long-pulsed or CW excitation by optimizing the doping and film morphology, incorporating the high-quality resonators, and the suitable pumping sources. Then, the OLED design based on these TADF molecules without efficiency rolloff under the extremely high current density injection will be investigated. In parallel, the advanced DFB resonators, such as $1^{st}/2^{nd}$ mixed-ordered, two dimensional (2D) resonators will be incorporated to further reduce the energy loss, as well as the lasers thresholds toward the electrical-pumping OSLDs as shown in **Figure 6-3**.

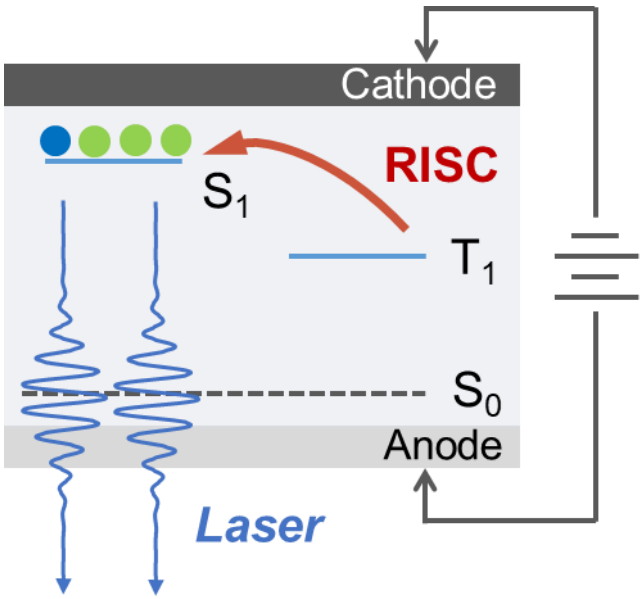

Figure 6-3. Schematic diagram of the terminal electrical-pumping TADF OSLDs.

A fast RISC process plays a crucial role in efficiently harvesting triplets. As we know, a slow RISC process would lead to exciton annihilations, which is responsible for the degradation and severe efficiency rolloff, especially under the high current

density injection. Though optical-pumping DFB lasers from TADF molecules have been realized in my work, the relatively small RISC rate (k_{RISC} ~10^4 s^{-1} for PXZN-B, DMACN-B, and PhCzBN1) leaves the space for the faster candidates. Therefore, novel TADF molecules incorporating the charge-resonance type hybrid triplet states, charge hopping, and other novel strategies will be designed with an even faster RISC process exceeding 10^8 s^{-1} for realizing OSLDs with even better performance.

Moreover, triplet utilization could also be realized by the TADF-assisted fluorescence (TAF) strategy, where TADF molecules with a very fast RISC process are used as the triplet harvester rather than the terminal laser dye. Therefore, new TADF molecules (no laser properties) with very fast spin-flip accelerate RISC rates (>10^8 s^{-1}), will be designed based on charge-resonance type hybrid triplet states, thermal equilibration, and other novel unraveled mechanisms,[1, 2] which would be promising to be employed for stabilizing OSLDs under electrical-pumping.

References

[1] L.-S. Cui, A. J. Gillett, S.-F. Zhang, H. Ye, Y. Liu, X.-K. Chen, Z.-S. Lin, E. W. Evans, W. K. Myers, T. K. Ronson, H. Nakanotani, S. Reineke, J.-L. Bredas, C. Adachi, R. H. Friend, *Nat. Photon.* **2020**, *14*, 636.

[2] N. Aizawa, A. Matsumoto, T. Yasuda, *Sci. Adv. 7*, eabe5769.

Publication list

Papers

1. **X. Tang**, Y. T Lee, Z. Feng, S. Y. Ko, J. W. Wu, V. Placide, J. C. Ribierre, A. D. Aléo and C. Adachi, ***ACS Materials Letters,* 2020**, *2*, 1567-1574.

2. **X. Tang**, U. Balijapalli, D. Okada, B. S. B. Karunathilaka, C, A. M. Sensvirathne, Y. T. Lee, Z. Feng, A. S. D. Sandanayaka, T. Matsushima and C. Adachi, ***Advanced Functional Materials,* 2021**, 2104529.

3. A. Khan[#], **X. Tang[#]**, C. Zhong, Q. Wang, S. Y. Yang, F. C. Kong, S. Yuan, A. S. D. Sandanayaka, C. Adachi, Z. Q. Jiang and L. S. Liao, ***Advanced Functional Materials,* 2021**, 2009488. (*A. Khan and **X. Tang** equally contributed*)

4. U. Balijapalli[#], **X. Tang[#],** D. Okada, Y. T. Lee, B. S. B. Karunathilaka, M. Auffray, G. Tumen-Ulzii, Y. Tsuchiya, A. S. D. Sandanayaka, T. Matsushima, H. Nakanotani and Chihaya Adachi, ***Advanced Optical Materials,* 2021**, 2101122. (*U. Balijapalli and **X. Tang** equally contributed*)

5. **X. Tang**, Y. T. Lee, C, A. M. Sensvirathne, A. S. D. Sandanayaka, T. Matsushima, C. Adachi. (*Under preparing*)

6. Y. T. Lee, C. Y. Chan, M. Tanaka, M. Mamada, K. Goushi, **X. Tang**, Y. Tsuchiya, H. Nakanotani, C. Adachi. (*Submitted*)

International conferences

1. **X. Tang**, A. Khan, Z. Q. Jiang, C, Adachi, *Quasi-Planar TADF Molecular Design Towards Pure Violet-Blue Electroluminescence and Organic Laser*, **The 13th Asian Conference on Organic Electronics (A-COE 2021)**, Nagoya, Japan. (Poster presentation, **"Best Poster Award"**)

List of abbreviations

Materials

1,4,5,8,9,11-hexaazatriphenylene-hexacarbonitrile (**HAT-CN**)

Tris(8-hydroxyquinoline) aluminum (**Alq$_3$**)

Tris(2-phenylpyridine)iridium(III) [**Ir(ppy)$_3$**]

1,2,3,5-tetrakis(carbazol-9-yl)-4,6-dicyanobenzene (**4CzIPN**)

1,1-bis[4-[*N,N*-di(p-tolyl)amino]phenyl]cyclohexane (**TAPC**)

4,4′,4″-tris(*N*-carbazolyl)triphenylamine (**TCTA**)

9,9′,9″-triphenyl-9*H*,9′*H*,9″*H*-3,3′:6′3″-tercarbazole (**Tris-PCz**)

N,N′-dicarbazolyl-3,5-benzene (**mCP**)

3,3-di(9*H*-carbazol-9-yl)biphenyl (**mCBP**)

Bis(2-(diphenylphosphino)phenyl)ether oxide (**DPEPO**)

1,3,5-tri(*m*-pyrid-3-yl-phenyl)benzene (**TmPyPB**)

1,3,5-tris(*N*-phenylbenzimidazol-2-yl)benzene (**TPBi**)

8-hydroxyquinolatolithium (**Liq**)

Lithium fluoridoe (**LiF**)

Aluminum (**Al**)

Indium tin oxide (**ITO**)

Triphenylamine (**TPA**)

Poly(methylmethacrylate) (**PMMA**)

Poly(3,4-ethylene dioxythiophene):poly(styrenesulfonate) (**PEDOT:PSS**)

4,4'-bis(*N*-carbazolyl)-1,1'-biphenyl (**CBP**)

4,4′-bis[(N-carbazole)styryl]biphenyl (**BSBCz**)

4,7-dibromo-2,1,3-benzothiadiazole (**BTD**)

4,8-dibromobenzo[1,2-c:4,5-c′]bis-[1,2,5]thiadiazole (**BBTD**)

2,6-dicyano-1,1-diphenyl-$\lambda^5\sigma^4$-phosphinine (**DCNP**)

Molybdenum trioxide (**MoO_3**)

Boron/nitrogen (**B/N**)

trans-1,4-distyrylbenzene (**DSB**)

Bis-styrylbenzene (**BSB**)

Keywords

Amplified spontaneous emission (**ASE**)

Aggregation caused quenching (**ACQ**)

Becke, three-parameter, Lee-Yang-Parr functional (**B3LYP**)

Commission international de l'Eclairage (**CIE**)

Charge transfer (**CT**)

Cyclic voltammetry (**CV**)

Continuous-wave (**CW**)

Donor-acceptor (**D-A**)

Direct current (**DC**)

Dexter energy transfer (**DET**)

Delayed fluorescence (**DF**)

Distributed feedback (**DFB**)

Density functional theory (**DFT**)

Differential scanning calorimetry (**DSC**)

Electron-blocking layer (**EBL**)

Electron-injection layer (**EIL**)

Electroluminescence (**EL**)

Emissive layer (**EML**)

External quantum efficiency (**EQE**)

Electron-transporting layer (**ETL**)

Förster resonance energy transfer (**FRET**)

Full width at half maximum (**FWHM**)

Hole-blocking layer (**HBL**)

Hole-injection layer (**HIL**)

Hybrid locally charge transfer (**HLCT**)

Highest occupied molecular orbital (**HOMO**)

Hole-transporting layer (**HTL**)

Internal conversion (**IC**)

Intramolecular charge transfer (**ICT**)

Internal quantum efficiency (**IQE**)

Intersystem crossing (**ISC**)

Locally excited (**LE**)

Lowest unoccupied molecular orbital (**LUMO**)

Multiple resonance (**MR**)

Mass spectrum (**MS**)

Near-infrared (**NIR**)

Nuclear magnetic resonance (**NMR**)

Organic light-emitting diode (**OLED**)

Organic semiconductor laser (**OSL**)

Organic semiconductor laser diode (**OSLD**)

Power efficiency (**PE**)

Phosphorescence organic light-emitting diode (**PhOLED**)

Photoluminescence (**PL**)

Photoluminescence quantum yield (**PLQY**)

Reverse intersystem crossing (**RISC**)

Spin-orbit coupling (**SOC**)

Spin-orbit perturbation (**SOP**)

Singlet-singlet annihilation (**SSA**)

Singlet-polaron annihilation (**SPA**)

Singlet-triplet annihilation (**STA**)

Thermally activated delayed fluorescence (**TADF**)

Thermally activated delayed fluorescence assisted fluorescence (**TAF**)

Time-dependent density functional theory (**TDDFT**)

Transition dipole moment (**TDM**)

Thermogravimetric analysis (**TGA**)

Triplet-polaron annihilation (**TPA**)

Triplet-triplet annihilation (**TTA**)

Ultraviolet visible (**UV-vis.**)

Physical symbols

ASE threshold ($\boldsymbol{E_{th}}$)

Arbitrary unit (**a. u.**)

Boltzmann constant ($\boldsymbol{k_B}$)

Spin angular momentum ($\boldsymbol{S}$)

Ground state ($\mathbf{S_0}$/ $\boldsymbol{E_1}$)

Excited state ($\boldsymbol{E_2}$)

The lowest singlet excited state ($\mathbf{S_1}$)

The lowest triplet excited state ($\mathbf{T_1}$)

Wavelength ($\boldsymbol{\lambda}$)

HOMO wavefunction ($\boldsymbol{\varphi_H}$)

LUMO wavefunction ($\boldsymbol{\varphi_L}$)

Oscillator strength ($\boldsymbol{f}$)

Einstein's B coefficient ($\boldsymbol{B}$)

Radiative decay rate ($\boldsymbol{k_r}$)

Nonradiative rate ($\boldsymbol{k_{nr}}$)

Intersystem crossing rate ($\boldsymbol{k_{ISC}}$)

Intersystem crossing rate ($\boldsymbol{k_{RISC}}$)

Radiative lifetime ($\boldsymbol{\tau_r}$)

Prompt decay lifetime ($\boldsymbol{\tau_p}$)

Delayed decay lifetime ($\boldsymbol{\tau_d}$)

Fluorescence quantum yield ($\boldsymbol{\phi_{PL}}$)

Transition dipole moment ($\boldsymbol{\vec{\mu}}$)

Current density-voltage (***J-V***)

Outcoupling factor ($\boldsymbol{\eta}$)

Stimulated emission cross-section ($\boldsymbol{\sigma_{em}}$)

Singlet-triplet splitting ($\boldsymbol{\Delta E_{ST}}$)

Frequency of light ($\boldsymbol{\nu}$)

Velocity of light (***c***)

Grating period ($\boldsymbol{\Lambda}$)

Planck's constant (***h***)

Spin statistic factor ($\boldsymbol{\chi}$)

Operational time at half luminance maximum ($\boldsymbol{T_{50}}$)

Thermal decomposition temperature ($\boldsymbol{T_d}$)

Luminance (***L***)

Kelvin (***K***)

Celsius degree (**°C**)

Nanosecond (**ns**)

Microsecond (**µs**)

Millisecond (**ms**)

Molar per liter (**M**)

Acknowledgement

First and foremost, I would like to take this opportunity to express my deepest gratitude and highest respect to my supervisor, Prof. Chihaya Adachi. It has been three years since my first meet and face-to-face communication with Prof. Adachi in EL2018, Tokyo, 9/2018. It is always my greatest honor that Prof. Adachi offered me an invaluable opportunity and scholarship support to Japan, to be a member of our OPERA family. Adachi-sensei initiated and guided me into a challenging and “stimulated” field of organic semiconductor lasers, which represents the ultimate luminescence with the highest color purity, highest intensity, and highest directionality. Actually, those are the most precious personalities of Adachi-sensei, where I am motivated: with the purest passion, endeavor, and persistence to strive for the facts and breakthroughs of research. Adachi-sensei always offered me unparalleled freedom to attempt and explore unknowns in the research. Moreover, Adachi-sensei always promoted me to attend the cutting-edge international conferences or lectures, and recommended me to apply the research project for practicing leadership. Whenever I encountered failure and felt confused, he was always here to encourage me and give me valuable suggestions. Under Adachi-sensei’s supervision, I realized the importance of revealing the underlying principles and mechanisms behind the performance. All of these unforgettable experiences with Adachi-sensei will definitely be of the most precious treasure for my future career and life.

I also deeply grateful to Prof. Hiroyuki Furuta and Prof. Yuji Oki for serving as the members of my thesis defense committee. Their valuable and constructive comments and suggestions helped me further improve the thesis and presentation.

I would like to sincerely appreciate Associate Prof. Toshinori Matsushima for his continuous encouragement, constructive guiding and discussion when encountering the difficulties and challenges in the research. It took an enormous of time and efforts for him to carefully revise my manuscripts and Ph.D. thesis word by word, and I learnt a lot from his passion, optimism and hard-working attitude on the research and daily life.

I would like to sincerely express my gratitude to Prof. Atula Sandanayaka for his great support and teaching on my organic laser works. At my initial stage of Ph.D. course, he taught and trained me to use optical instruments, accompanied with me to check the film deposition and device fabrication technology. Even after returning Sri Lanka, he always provided me the discussion and support to promote my research progress.

I would like to express my appreciation to Associate Prof. Hajime Nakanotani for the kind suggestions on my research work, and his support on my courses and lectures in the department; Assistant Prof. Kenichi Goushi and Assistant Prof. Masashi Mamada for their kind teaching, discussion and support on my experiment and daily life; and Associate Prof. Youichi Tsuchiya for his kind and valuable comments and suggestions on my research and presentations.

Then, I am deeply grateful to Prof. Anthony D'Alésio and Dr. Virginie Placide in France for their teaching of the photophysical measurements, the fruitful discussion of

laser materials design and our collaborated papers; Prof. Jean-Charles Ribierre for the help and advice in my research work. And I also sincerely thank Prof. Zuo-Quan Jiang and Prof. Liang-Sheng Liao in Soochow University for recommending me to study abroad and broaden my horizon, they always provided me with the great encouragement, support, and valuable discussion of my research. In addition, I would like to acknowledge Dr. Yi-Ting Lee for her kind support and teaching of the theoretical calculation and device fabrication.

Furthermore, I would like to express my appreciation to all the members in our OPERA family, Prof. Chuanjiang Qin, Associated Prof. Ryota Kabe, Associated Prof. Kai Wang, Associated Prof. Yongsheng Hu, Dr. Chin-Yiu Chan, Dr. Daichi Okada, Dr. Ryutaro Komatsu, Dr. Dr. Umamahesh Balijapalli, Dr. Buddhika Sanjeewa Bandara Karunathilaka, Dr. Zesen Lin, Dr. Tai Cheng, Dr. Morgan Auffray, Dr. Ganbaatar Tumen-Ulzii, Dr. Chathuranganie Senevirathne, Dr. Tomohiro Ishii, Dr. Hao Ye, Dr. Linsong Cui, Dr. Fatima Bencheikh, Dr. Ryo Nagata, Dr. Kazuya Jinnai, Dr. Minghan Cai, Dr. Aziz Khan, Mr. Zhao-Feng, Mr. Xuelong Liu, Mr. Jaehyun Bae, Ms. Alasvand Yazdani Sahar, Mr. Satoru Watanabe, Mr. Yuya Oyama, Ms. Reiko Aoki, Mr. Shinichi Tan, Mr. HyunSuk Park, Mr. Thanh Ba Nguyen, Mr. Kotaro Takekuma, Mr. Nishiki Yamada, Mr. Yusaku Kashiwagi, Ms. Ayano Abe, and other members. I also would like to thank all the secretaries and staffs for their warm and kind support and help in my daily life, experiment, and manuscript uploading and submission, especially for Ms. Sachiko Higashikawa, Ms. Yuko Kawahara, Ms. Hiroko Kuratomi, Ms. Rei Sasagawa; Then, Ms. Nozomi Nakamura, Ms. Keiko Kusuhara, and Ms. Shinobu Terakawa for

their kind assistant for technical support. Moreover, I would like express my deep gratitude to my dear friends for their warm and continuous encouragement throughout the three years.

Finally, I would like to sincerely express my deepest gratitude to my dear parents for their selfless and endless love, they are always here behind me and encouraging me to be brave to pursue my dream, to fly higher, to see, to experience this colorful world. Meanwhile, I would like to sincerely express my special gratitude and love to my girlfriend, she is always accompanying with me to go through the challenges, her patience and warm love encourages me to pursue the bright future together.

Fukuoka
January, 2022
Xun Tang